Astronomy Reports, Vol. 47, No. 6, 2003, pp. 443–457. Translated from Astronomicheskiĭ Zhurnal, Vol. 80, No. 6, 2003, pp. 483–498.

A Dynamical Model of the Galaxy

A. V. Khoperskov and N. V. Tyurina

Sternberg Astronomical Institute, Universitetskiĭ pr. 13, Moscow, 119992 Russia

Received January 28, 2002; in final form, January 10, 2003

Abstract—A series of dynamical models of the Galaxy is constructed assuming that the entire disk is near the gravitational-stability limit. This imposes constraints on the dynamical and kinematic parameters of the main subsystems (the disk, bulge, and halo). The disk surface density in the solar neighborhood should not exceed $58\,M_\odot/\,\mathrm{pc}^2$. Further, we find that the observed local decrease in the rotational velocity at $6\ \mathrm{kpc} \lesssim r \lesssim 10\ \mathrm{kpc}$ is not associated with details of the radial distribution of matter in the Galaxy and instead results from dynamical processes or some other factors responsible for noncircular motions. It follows from the presence of a long-lived bar and the observed distribution of the stellar-velocity dispersion that the central maximum in the rotation curve at radius $r \simeq 300$ pc cannot be associated with a very concentrated bulge core. The best agreement between the observational data and the parameters of the dynamical models is achieved for a radial disk scale length of $L \simeq 3$ kpc. The relative contribution of the disk to the circular rotational velocity at $r = 2.2L$ is 73%. © *2003 MAIK "Nauka/Interperiodica"*.

1. INTRODUCTION

Our understanding of Galactic structure and of physical processes in the Galaxy has evolved as photometric and kinematic observational data have improved. One of the most important characteristics of the Galaxy is its rotation curve. The radial dependence of the rotational velocity of the dynamically cold component has been determined in many studies [1–6]. Various Galactic subsystems have different characteristic rotational velocities [7]. For example, the stellar disk rotates more slowly than the gaseous component: $V_* < V_{\mathrm{gas}}$, where $V_{\mathrm{gas}}(r)$ is the rotational velocity of the gas and young stars and $V_*(r)$ characterizes the old stellar population. One of the most important parameters used to constructs models of the Galaxy is the circular rotational velocity $V_c(r)$, which determines the spatial distribution of the gravitational potential and, consequently, of the mass. Various Galactic models [8–12] have shown that, along with the stellar and gaseous disks, the spheroidal subsystem also plays an important role. The disk and spheroidal subsystems have complex structures and are comprised of separate components with different physical properties. In particular, thin and thick components can be identified in the stellar disk [7], and a halo, bulge, and core, in the spheroidal subsystem.

The same rotation curve can be constructed using very different parameters for the disk and spheroidal components. This ambiguity can be reduced using data on the surface density of matter in the solar neighborhood $\sigma_\odot$ and the radial L and vertical h scales of the disk. Stellar-velocity dispersion data can impose additional constraints. This approach is based on the natural assumption that the disk formed by the old stellar population, which contains most of the disk mass, is gravitationally stable. Consequently, the condition $c_r \gtrsim c_r^{crit}$ is satisfied for the radial stellar-velocity dispersion. The quantity c_r^{crit} specifies the minimum value of c_r required for gravitational stability in the plane of the disk and has been calculated, for example, in [13–15]. The critical value of the radial-velocity dispersion depends on the equilibrium parameters of the system in a complex way, and there is no fully satisfactory theory that can be applied to calculate c_r^{crit} for reasonably realistic models of a three-dimensional, nonuniform disk with differential rotation. Essentially the only way to estimate c_r^{crit} is to simulate the stellar disk using dynamical models based on numerical integration of the N-body problem. This approach has made it possible to distinguish the masses of the spheroidal and disk components in a number of galaxies whose velocity dispersions are known from observations [16]. An additional constraint on the distribution of matter in the Galaxy is provided by the requirement that the disk be stable against bending perturbations, since this imposes conditions on the vertical-velocity dispersion c_z and the vertical structure of the disk [17, 18].

As a rule, it is assumed that $V_c = V_{\mathrm{gas}}$; i.e., if the motions are purely circular, the pressure gradient can be neglected when considering the radial force balance. One of the first Galactic models, constructed by Schmidt [8], was developed and substantially refined

1063-7729/03/4706-0443$24.00

in [9–12, 19–22]. A number of these axially symmetrical models have very different masses for their main components. The seven-component model proposed in [23] demonstrated the important role of pressure gradients in forming some parts of the Galactic rotation curve. Non-axially-symmetrical models, in particular, those taking into account the bar, can be constructed only via dynamical modeling [24, 25].

In contrast to the situation for other galaxies, where only the velocity dispersion along the line of sight is known from observations, all three components of the velocity dispersion in the Galaxy (c_r, c_φ, and c_z) are known in the solar neighborhood [26]. This information leads to additional constraints on models for the distribution of matter in the Galaxy. The aim of the present study is to develop a model for the Galaxy taking into account the latest data on the distributions of the components of the stellar-velocity dispersion. For each model satisfying the observed rotation curve, we determined the radial distributions of the velocity dispersion in the stellar disk via dynamical modeling. As a result, we were able to obtain a model that agrees well with the observational data for a wide range of observational parameters, including the distribution of the surface density of matter in the disk, the disk's thickness, the rotational velocities of the gaseous and stellar components, the velocity dispersions in the stellar disk, the presence of a bar, and data on the bulge.

2. DYNAMICAL MODELING

Our dynamical model of the Galaxy is based on numerical integration of the equations of motion for N particles interacting via their mutual gravitational attraction. We study the evolution of the disk subsystem in the gravitational field of spherical components with the volume density distribution

$$\varrho_s = \sum_m \frac{\varrho_{0m}}{(1+(r^2+z^2)/a_m^2)^n}, \qquad (1)$$

where the subscripts $m = b, h$ refer to the bulge and halo, respectively, $n = 1$ for a quasi-isothermal halo and $n = 3/2$ for the bulge (a King law), ϱ_{0m} is the central density of the corresponding component, and the parameters a_m specify the radial scales of the bulge and halo. One of the bulge subsystems is the core, whose density is also given by law (1) with the scale a_n. The density distribution (1) in the bulge is limited to the radius $r < (r_b)_{max}$. The law (1) is exponentially cut off at $r > (r_b)_{max}$, so that the mass of the bulge M_b is finite, and the mass of the halo $M_h(r)$ increases with radius. If the surface-density profile is exponential, $\sigma = \sigma_0 \exp(-r/L)$, the disk mass will be $M_d = 2\pi L^2 \sigma_0$, with about 95% of this mass concentrated at $r < 4L$. The relative mass of the halo inside a specified radius $\mu(r) = M_h(r)/M_d$ is considered.

The initial surface-density profile, $\sigma(r)$, is taken to be axially symmetric. The vertical volume density distribution in the disk, $\varrho(r,z)$, is determined by the condition that the system be in equilibrium. We obtain the vertical density profile by solving the equation [27]

$$\frac{d^2\varrho}{dz^2} - \frac{1}{\varrho}\left(\frac{d\varrho}{dz}\right)^2 + \frac{1}{c_z^2}\frac{dc_z^2}{dz}\frac{d\varrho}{dz} + \frac{4\pi G}{c_z^2}\varrho\,(\varrho+\varrho_s) - \frac{\varrho}{rc_z^2}\frac{dV_c^2}{dr} = 0 \qquad (2)$$

with the conditions $\frac{d\varrho(0)}{dz} = 0$ and $\int_\infty^\infty \varrho(r,z)dz = \sigma(r)$ for the specified distributions of the matter surface density $\sigma(r)$, vertical stellar-velocity dispersion $c_z(r,z)$, matter density in the spheroidal component $\varrho_s(r,z)$, and circular rotational velocity $V_c(r)$, which is determined by the gravitational potential Φ:

$$V_c = \sqrt{r\partial\Phi/\partial r}.$$

When $dc_z/dz = 0$, $\varrho_s = 0$, and $V_c = \text{const}$, the solution of (2) is

$$\varrho(z) = \frac{\sigma}{2z_0}\mathrm{ch}^{-2}(z/z_0) \qquad (3)$$

with the characteristic vertical scale height $z_0 = \sqrt{c_z^2/2\pi G\varrho(0)} = c_z^2/\pi G\sigma$.

The disk is taken to be initially in equilibrium in the radial and vertical directions but weakly gravitationally unstable: $Q_T = c_r/c_T < 1$ in the region $L \le r \le 2L$ ($c_T = 3.36G\sigma/\varkappa$ and $\varkappa = 2\Omega\sqrt{1+rd\Omega/(2\Omega dr)}$ is the epicyclic frequency) [13]. The system is heated as the instability develops, increasing the velocity dispersion. Specifying the initial state $Q_T \gtrsim 1$, we can refine the minimum radial-velocity dispersion necessary for gravitational stability of the disk.

The gravitational forces of the disk particles were calculated using the TREEcode method [28]. The number of particles in the models was $N = (60–300) \times 10^3$. The results for the models that were in the best agreement with the observational data were compared with those obtained using the particle–particle algorithm with $N = 40 \times 10^3$ (the gravitational force is computed via direct summation of the contributions of all the particles), and good agreement was found.

3. THE BASIC ASSUMPTIONS

We shall make the following assumptions when comparing the dynamical models with the observational data.

(1) If noncircular motions are not taken into consideration and the contribution of the pressure is not included in the radial force balance, we can assume that $V_c(r) \simeq V_{\rm gas}(r)$ for the rotational velocity of the youngest objects (i.e., the gaseous disk, young stars, and planetary nebulae). The circular velocity V_c in the $z = 0$ plane is determined by the distribution of matter in the three main components, namely, the disk, bulge, and halo. As a result, we obtain

$$V_c = \sqrt{(V_c^{disk})^2 + (V_c^{bulge})^2 + (V_c^{halo})^2}, \quad (4)$$

where V_c^{disk}, V_c^{bulge}, and V_c^{halo} specify the corresponding contributions of each of the separate components to the circular velocity. We restrict our consideration here to a stationary spheroidal subsystem.

(2) The observed old stellar disk of the Galaxy will be assumed to be gravitationally stable: $c_r > c_r^{crit}$. As was shown in [16, 19], the ratio of the radial-velocity dispersion to the circular velocity of the disk at a specified radius c_r/V_c decreases as the relative mass of the halo $\mu = M_h/M_d$ at the stability limit increases. Therefore, varying the parameters of the halo, bulge, and disk for a fixed circular velocity, we can change the radial dependences of the velocity dispersion c_r required for gravitational stability of the disk. Thus, we can determine the mass distributions in the subsystems of the model Galaxy by finding the parameters for which the model values $c_r(r)$ are equal to the observed ones $c_r^{obs}(r)$. Note that this approach yields a lower limit for the halo mass, since several additional factors can result in further increase of the velocity dispersion in the real stellar disk (for example, the multicomponent composition of the disk and the presence of the gaseous subsystem). We shall not discuss various mechanisms for heating the disk here [29]. It is important that the observed stellar velocity dispersion in the Galaxy ceases to increase starting from a certain stellar age ($\simeq 3 \times 10^9$ yr) [30].

(3) We shall assume that the observed old stellar disk is stable against bending perturbations at least within $\sim$10 kpc of the Galactic center. This condition imposes constraints on the vertical-velocity dispersion in the disk $c_z/c_r \geq Q_z \equiv (c_z/c_r)_{crit}$ [17, 18]. The ratio c_z/c_r can vary with radius [31], but the inequality $Q_z \gtrsim 0.4$ is always satisfied [17]. We shall assume that the observed vertical structure of the disk (the vertical-velocity dispersion and vertical density profile) corresponds to a stationary stable state.

The velocity dispersions and radial and vertical scales of the disk component in the dynamical models will be compared with observations for the old stellar disk. The matter forming the disk surface density will be taken to be composed of stars and interstellar medium.

To minimize the dependence of the results on the fitting method used in the multidimensional parameter space, the determination of the structure of the Galaxy was divided into several steps. Each will be considered separately, beginning with those for which the number of free parameters is smallest.

(a) *The solar neighborhood.* The presence of a local minimum in the circular velocity V_c depends only on the spatial distribution of matter in the disk at 6 kpc $\lesssim r \lesssim$ 10 kpc, and the main variable parameter is the vertical scale height of the disk.

(b) *The central region of the Galaxy.* The properties of the kinematics inside the central kiloparsec do not depend on the model parameters in the region $r \gtrsim 1$ kpc, at least within the uncertainty allowed by the data. On the other hand, the opposite is not true. In particular, it is obvious that the bar affects the outer regions. The parameter that admits the most variation is the size of the central nucleus, while its mass is uniquely defined for a specified dependence $V_c(r)$. All other quantities (the velocity dispersions, structure of the bar, etc.) are not free parameters of the dynamical models and are calculated in a self-consistent way. Thus, we determine the parameters of the central spheroidal subsystem in the second step.

(c) *The problem of the dark halo.* The problem of the mass in the dark halo is directly related to the disk surface density in the solar neighborhood, $\sigma_\odot$. We vary $\sigma_\odot$ to attain agreement of the model velocity-dispersion components with the observations. The accuracy of these kinematic parameters based on observations in the solar neighborhood is no worse than 3%, with the largest uncertainties in $\sigma_\odot$ being about 30%.

(d) *The vertical structure.* The last step is the determination of the vertical scale height of the disk Δ, based on the assumption that the stellar disk is stable (or nearly stable) against bending perturbations. Vertical heating of the disk due to bending instabilities is much slower than relaxation processes in the plane of the disk. Therefore, the vertical structure (with scale height Δ) is formed against the background of the other parameters having nearly become steady state, but in a self-consistent model.

4. THE ROTATION CURVE

The rotation curve for the young Galactic population has been found in many studies; the observational data of [1, 3–6, 32–36] are presented in Fig. 1. The kinematic data for both the gaseous component and for various types of objects (OB stars, planetary nebulae, Cepheid variables, HI and HII regions, and carbon stars) have been used to derive Galactic rotation curves. We will denote all such curves based on observations of young populations by $V_{\rm gas}$.

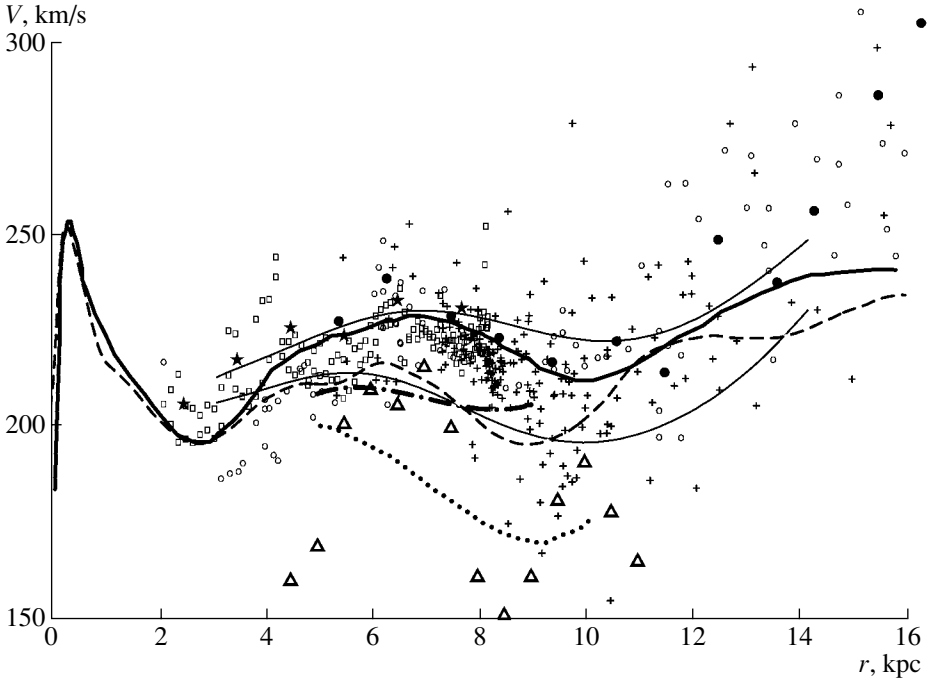

Fig. 1. Galactic rotation curves derived in various ways: from HI and CO data with $R_\odot = 8.5$ kpc [1, 4] (solid thick curve); from CO and H_α data with $R_\odot = 8.5$ kpc [6] (dashed curve); from the radial velocities and proper motions of classical Cepheids with $R_\odot = 7.1$ kpc [33] (dotted curve) and with $R_\odot = 7.5$ kpc and $R_\odot = 8.5$ kpc [36] (solid thin curve); from the kinematic parameters of OB associations with $R_\odot = 7.1$ kpc [35] (dash–dot curve); from 21 cm (open circles), HI (squares), and CO (crosses) data with $R_\odot = 8.2$ kpc [37]; from HI (asterisks) and HII (solid circles) data with $R_\odot = 8.5$ kpc [3]; and from the kinematics of planetary nebulae and AGB stars with $R_\odot = 7.9$ kpc [32] (triangles).

There are two characteristic features in the observed Galactic rotation curve: (1) a local minimum in the solar neighborhood ($r \simeq 6$–11 kpc, Fig. 1) and (2) a local inner maximum inside the central kiloparsec [1] (Fig. 1). Let us discuss the consequences of these features when constructing the model for the circular velocity assuming $V_c = V_{\rm gas}$. We shall consider the particular example of the rotation curves presented by Sofue *et al.* [4, 6] (thick solid and dashed curves in Fig. 1). Our conclusions do not depend on various discrepancies between the rotation curves constructed by various authors using different values of $R_\odot$ and observations of different objects. For example, the rotational velocity of [3] changes only slightly when $R_\odot$ is varied in the range 7.5–9.5 kpc. When $R_\odot$ and $V_{gas\odot}$ are varied, the absolute values of the spatial scales for various components and their masses in the dynamical models change, but their relative values are nearly constant.

Let us discuss these features of the Galactic rotation curve.

4.1. The Galactic Rotation Curve at $r \gtrsim 6$ kpc

The local minimum in the circular rotational velocity in the solar neighborhood could be due to the density distribution in the disk [34, 37] or halo. In the former case, we can assume that the radial surface-density distribution is described, for example, by a sum of two exponential laws with different radial scales, $L_{\sigma 1}$ and $L_{\sigma 2}$. The disk with the shorter scale must be sharply cut off at $r \simeq 6$–7 kpc, and the second disk, at $r \simeq 12$–15 kpc. Figure 2a presents the circular velocity for this type of model with a fairly massive disk (total mass $M_d = 7 \times 10^{10} M_\odot$) for the case of an infinitely thin disk ($z_0 = 0$). To obtain the minimum value $\Delta V = 15$ km/s, the total surface density must decrease by approximately a factor of two in the narrow zone $r = (6$–$6.4)$ kpc (Fig. 2b). The gravitational contribution of the disk matter is dominant at 3 kpc $\lesssim r \lesssim 15$ kpc (Fig. 2c). This is the maximum-disk model,[1] which, as we will show in Section 5.1, does not yield agreement with the observed stellar velocity dispersions.

Taking into account the finite thickness of the disk decreases ΔV to 6 km/s for $z_0 = 500$ pc (Figs. 2d, 2e). The quantity ΔV decreases as the

[1] In this model, the contribution of the disk component to the Galactic circular velocity is the maximum possible. As a result, $85 \pm 10\%$ of the circular velocity ($V_c^{disk}/V_c = 0.75$–0.95) is attained at the radius $r = 2.2 L_\sigma$ (where the circular velocity of the exponential disk is maximum) [22].

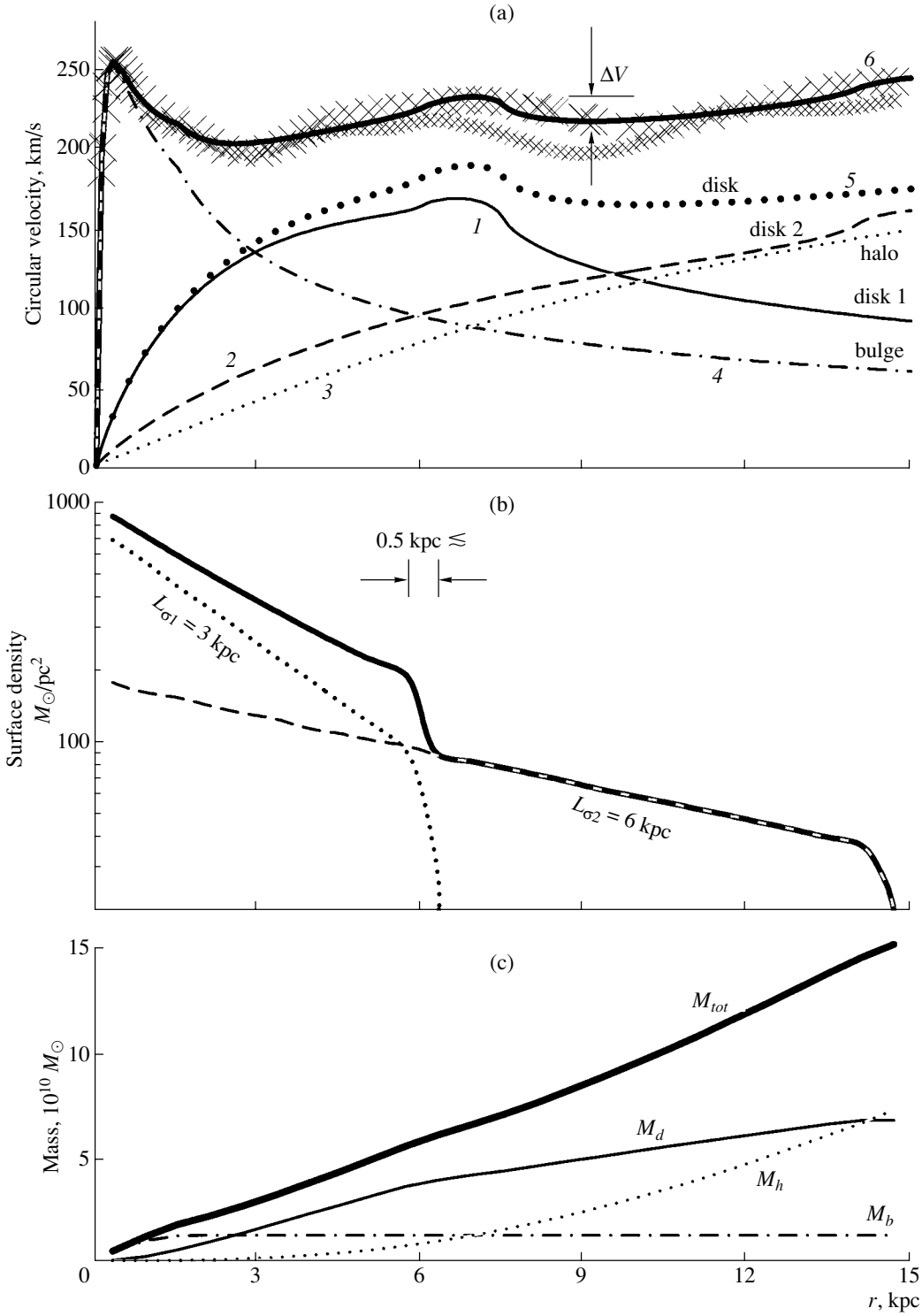

Fig. 2. (a) Circular velocity V_c in a model with an infinitely thin disk (solid curve *6*). The crosses represent the rotational velocity according to [4, 6] (see Fig. 1). Shown are the contributions to the circular velocity from disk 1 (curve *1*), $L_{\sigma 1} = 3$ kpc, with the disk cut off at 6 kpc; disk 2 (curve *2*), $L_{\sigma 2} = 6$ kpc, with the disk cut off at 14 kpc; the halo (curve *3*); the bulge (curve *4*); and the sum of the two disks (curve *5*). (b) Profiles of the surface density of the disk components for the model shown in Fig. 2a. (c) Radial dependences of the masses of various components within a radius r. (d) Radial dependence of the circular velocity V_c and the corresponding contributions of disk components 1 and 2, the bulge, and the halo for a disk of finite thickness with a vertical scale height of $z_0 = 0.5$ kpc. The relative halo mass inside a radius of 12 kpc is $\mu = 0.51$. All notation is the same as in Fig. 2a. (e) Radial distributions of the surface densities of the two disks and the sum of these distributions for the model in Fig. 2d. (f) Circular velocity for the model with a massive halo $\mu = 1.9$ (inside a radius of 12 kpc) and an infinitely thin disk. (g) Radial profiles of the surface density for the model in Fig. 2f.

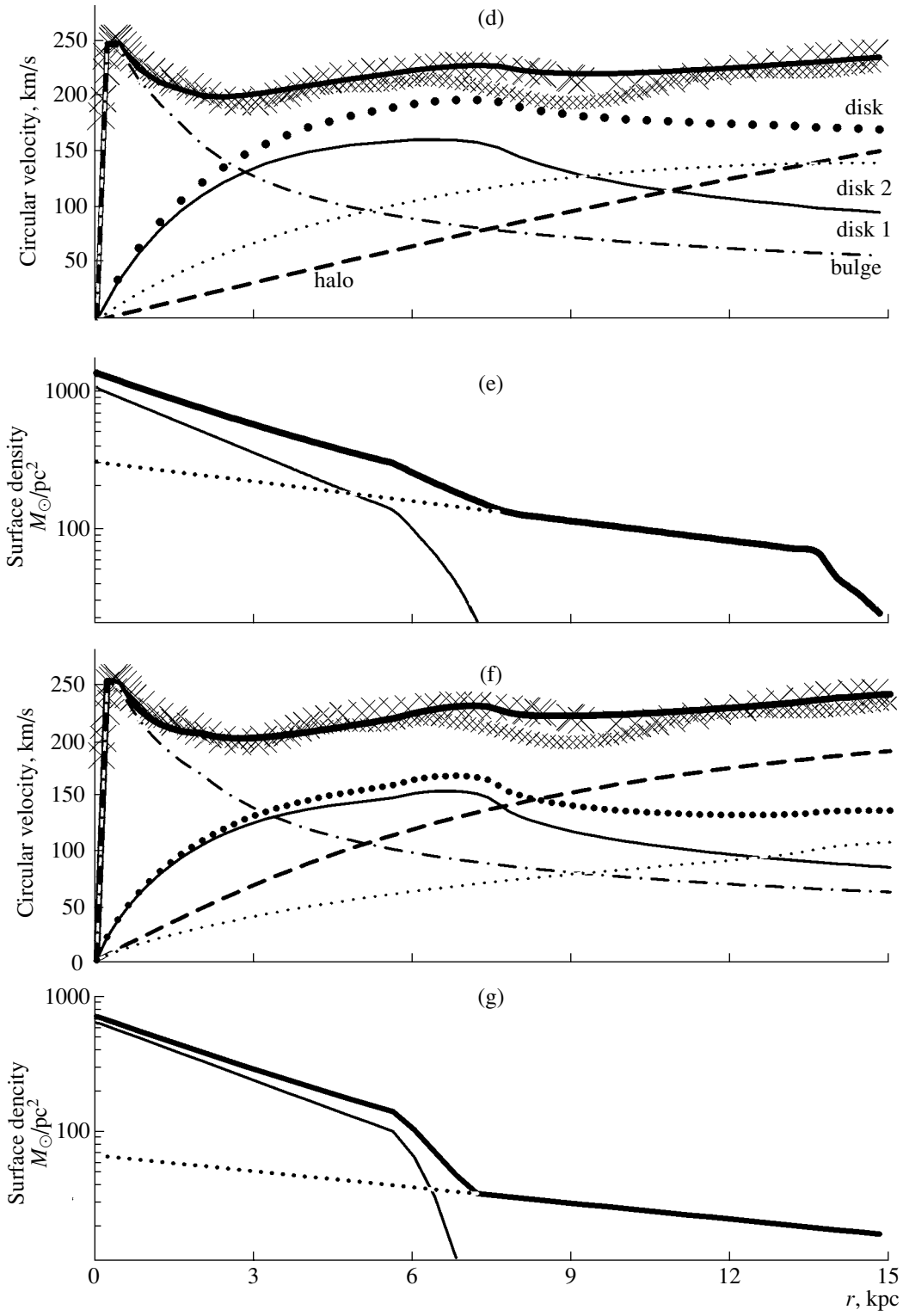

Fig. 2. (Contd.)

halo mass increases (and the disk mass correspondingly decreases), since the relative contribution of the disk to the circular velocity becomes lower, in accordance with (4). To obtain the minimum value $\Delta V = 9$ km/s in a model with a more massive halo $\mu = M_h(4L)/M_d = 1.9$ and infinitely thin disk (Fig. 2f), the surface-density change must be $\sigma(r = 5.8 \text{ kpc})/\sigma(r = 7 \text{ kpc}) \gtrsim 3$ (Fig. 2g). The velocity

minimum decreases to $\Delta V = 3$ km/s as the vertical scale height increases to the observed value $z_0 \simeq 500$ pc for a specified run of the surface density.

In other S galaxies, appreciable deviations from exponential photometric profiles are observed either at the edge [38, 39] or center of the galaxy, as a central depression of the stellar disk [40]. One possible explanation for the universal nature of the exponential brightness distributions of the disk components may be characteristic features of the evolution of a viscous gas in the presence of star-formation processes [41]. Computations show that, acting over several billion years, these factors do indeed form an exponential stellar-disk profile for any initial gas distribution. The sharp decrease in the surface density at $r = 6$–7 kpc is not directly confirmed by observations.

The minimum in $V_c(r)$ could, in principle, also be due to specific features of the density distribution in the halo, but this requires a sharper decrease in the volume density near $r \simeq 6$ kpc than in the disk case (Fig. 2). If the diameter of the epicyclic motion in the disk in the solar neighborhood is $\Delta r = 2c_r/\varkappa \simeq 2$ kpc (slightly less than the characteristic size of the velocity minimum), the required jump in the density distribution can, in principle, be reproduced. On the other hand, a narrow radial dip in the distribution of matter in the halo cannot be long-lived, since the typical velocity dispersion in the halo is on the order of 100 km/s.

Another argument against the existence of a strong local minimum in the circular velocity $V_c(r)$ follows from kinematic data. The particles in a collisionless system move in epicyclical orbits, resulting in the condition

$$\frac{c_r}{c_\varphi} = \frac{2\Omega}{\varkappa}, \qquad (5)$$

where c_φ is the azimuthal-velocity dispersion. Relation (5) was adopted in the dynamical models at the initial time and then checked during the computations. In all cases, this condition was satisfied with very good accuracy, providing direct proof of the collisionless nature of the constructed models. We emphasize that condition (5) is satisfied in the dynamical models for the angular stellar-rotation velocity $\Omega = V_*/r$.

The radial dependences of $N_\Omega \equiv 2\Omega/\varkappa$ and $n \equiv -d\ln\Omega/d\ln r$ for the rotation curve of Sofue *et al.* [6] are shown in Fig. 3. We can see substantial variations in the parameter $2\Omega/\varkappa \simeq 1$–$2.1$ at $r = 8$–10 kpc. In the solar neighborhood, $2\Omega/\varkappa \simeq 1.7$, which yields, in accordance with (5), $c_r/c_\varphi \simeq 1.7$. Let us now turn to the observational data. For the old stellar population in the solar neighborhood, $c_r/c_\varphi \simeq 1.55$ [26], which

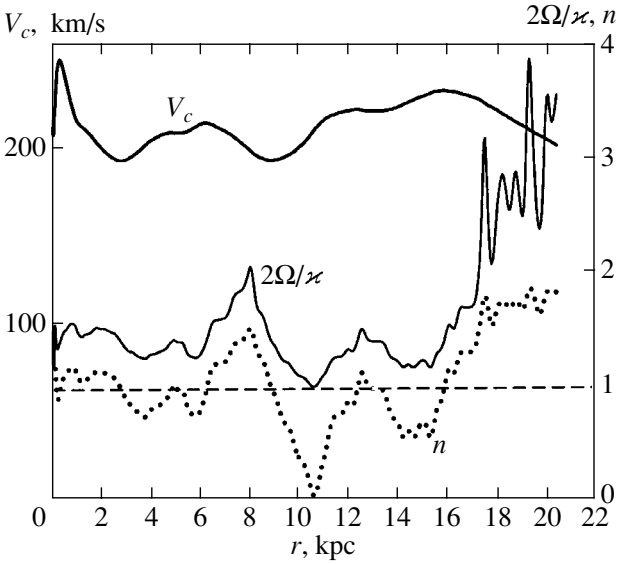

Fig. 3. Radial dependences of $2\Omega/\varkappa$ and $n = -d\ln\Omega/d\ln r$ (right-hand axis) for the rotation curve $V_c = r\Omega$ (left-hand axis), which coincides with dashed curve *2* in Fig. 1.

gives $n = 1.15$. As a result, we obtain a very flat rotation curve, $V \propto r^{-0.15}$. For the young stellar population, $c_r/c_\varphi = 8.2/5.8 = 1.41$ [35], which also yields $V \simeq$ const. Analysis of the velocity distribution for the nearest stars from *Hipparcos* data shows that the angular speed of rotation in the solar neighborhood is nearly independent of the radius: $\Omega \propto r^{-1/9}$ [42].

The velocity dispersions of young stars (Cepheid variables and stars in young clusters) found in [5] were $(c_r, c_\varphi, c_z) = (15.0, 10.3, 8.5)$ km/s. The mean age of these objects is 10^7 yr. It is very interesting that the parameter $c_r/c_\varphi = 1.46$ is close to the ratio $2\Omega/\varkappa$ if $n = 1.06$ (i.e., $V \propto r^{-0.06}$). Consequently, the characteristic time for the formation of the epicyclic motion is substantially less than the Galactic rotation period.

Therefore, there are arguments supporting the possibility that the observed minimum in the rotation curve of the gaseous and young stellar components is not related to some specific features of the radial distribution of the gravitational mass but instead most likely represents a dynamical phenomenon that could be associated, for example, with noncircular motions due to the propagation of a spiral density wave. We also cannot rule out the possibility that the minimum in the rotation curve found in [4–6, 33, 37] is due to systematic effects associated with the local coordinate system.

Data on the kinematics of OB stars and classical Cepheid variables at radii $r = 6$–12 kpc are consistent with the rotational velocity of the Galaxy being

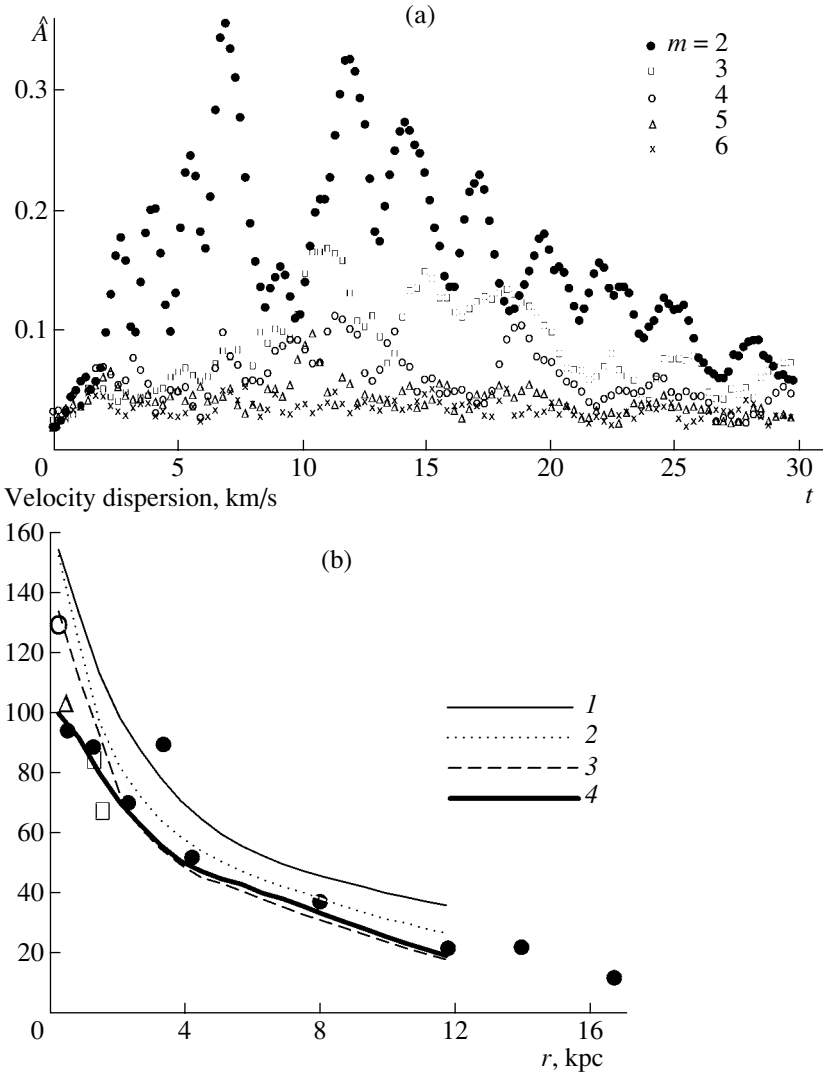

Fig. 4. (a) Time dependence of the integrated amplitudes of the Fourier harmonics for azimuthal numbers $m = 1, 2, \ldots, 6$ in a model with a massive, concentrated nucleus. A bar initially forms and is later disrupted, as follows from the decreasing amplitude of the $m = 2$ harmonic. The time $t = 30$ corresponds to 2.8×10^9 yr. (b) Radial dependences of the radial stellar-velocity dispersion c_r. The observational data used are the results of [2, 26] (solid circles), the velocity dispersion of late-type giants inside $r = 0.3$ kpc [45, 46] (open circles), the data of [47] (triangles), and the data of [48] (squares). The dynamical modeling with various parameters of the halo and bulge ($\mu = M_h/M_d$ is the relative mass of the halo inside $4L = 12$ kpc) yielded dependences for (*1*) $\mu = 0.95$, (*2*) $\mu = 1.42$, (*3*) $\mu = 1.5$, and (*4*) $\mu = 1.6$. The first three models include a concentrated nucleus with scale $a_n \leq 100$ pc, while there is no nucleus in the fourth model, with the bulge scale being $a_b = 200$ pc. It is clear that c_r decreases with increasing halo mass. To decrease the radial-velocity dispersion to values of about 100–120 km/s in the central region, $r \lesssim 2$ kpc, it is necessary to consider a bulge with a scale of $a_b \gtrsim 200$ pc.

constant in this region [43]. On the other hand, the kinematics of planetary nebulae, dust-envelope stars, and carbon stars show a rotational-velocity minimum in the solar neighborhood at $r = 8.5$ kpc [32] (triangles in Fig. 1). If the local minimum is associated with the spiral structure, the amplitude of the corresponding perturbations must be extremely large [32].

4.2. Kinematics of the Central Region ($r \lesssim 1$ kpc) and the Bar

The results of several studies have shown [1, 4, 6] that the rotational velocity of the cold subsystem in the central region $r \lesssim 1$ kpc possesses a well-defined maximum at $r \simeq 0.3$ kpc. Let us assume that $V_c = V_{\rm gas}$. Then, to explain the central maximum of the circular velocity, we must take into consideration a massive bulge with a concentrated nucleus, whose King model parameters are $a_n \simeq 100$ pc, $M_b \simeq 0.6 \times$

$10^{10}M_\odot$, and $(r_b)_{\max} \simeq 0.8$ kpc. In this case, the central density of the spheroidal subsystem exceeds 400 $M_\odot/\mathrm{pc}^3$.

The concentrated, massive bulge prevents the formation of a long-lived bar in the dynamical models. The bar is disrupted via a mechanism similar to the action of a massive, central black hole [44]. The deviation from axial symmetry of the distribution of disk matter at each time can conveniently be characterized by the amplitudes of the Fourier harmonics

$$A(p,m,t) = \frac{1}{N}\sum_{j=1}^{N} \exp\left\{i\Big[m\varphi_j(t) + p\ln(r_j(t))\Big]\right\}, \quad (6)$$

where p and m specify the structure of the perturbations in the radial and azimuthal directions, respectively. Figure 4a shows the time dependence of the integrated amplitudes

$$\hat{A}(m,t) = \sqrt{\sum_p |A(p,m)|^2}. \quad (7)$$

The value of $\hat{A}(2,t)$ describes the amplitude of the two-arm mode and, in particular, the bar. This parameter decreases during the evolution of the dynamical model, indicating the disruption of the bar and the formation of an initially axially-symmetric distribution of matter in the disk. The models with various bulge parameters show that the lifetime of the bar increases when the mass of the central spherical subsystem (bulge + nucleus) decreases and/or the scale of the bulge nucleus a_n increases. This imposes some constraints on the bulge parameters. Thus, a concentrated, massive bulge ($a_n \lesssim 100$ pc, $\varrho_{b0} \gtrsim 400 M_\odot/\mathrm{pc}^3$) is incompatible with the presence of a long-lived central bar (Fig. 4a).

Let us note another argument against the presence of a very concentrated mass distribution in the bulge, based on the line-of-sight velocity dispersion for late-type giants within 0.3 kpc of the Galactic center, $c^{obs}(0) \simeq 128 \pm 14$ km/s [45, 46]. Blum *et al.* [45, 46] believe that this quantity characterizes the stars in the bulge, so that the velocity dispersion for the disk component should be lower. A sample of K giants within 500 pc of the center has $c_r^{obs} \simeq 104 \pm 10$ km/s [47]. Lewis and Freeman [2] obtained the value $c_r^{obs} = 106$ km/s for the central velocity dispersion for disk stars. Figure 4b shows the radial distributions of the velocity dispersion c_r for disk stars derived from observations together with the results of the dynamical modeling for various relative disk masses. The thin curves represent models with massive, concentrated bulges ($a_n \simeq 100$ pc), which result in a central rotational velocity, in accordance with Fig. 1. Although it is possible to obtain agreement between the observed and model values of c_r at $r \gtrsim 3$ kpc for some disk mass, the velocity dispersion at the disk center obtained in the dynamical models exceeds 130 km/s (curves *1* and *2* in Fig. 4b). Agreement between the velocity dispersions at the disk center can be achieved only in models with a large bulge scale, $a_n \gtrsim 200$ pc (thick curve in Fig. 4b). In this case, the central volume density of the bulge does not exceed $100 M_\odot/\mathrm{pc}^3$, and the bulge mass is $\lesssim 10^{10} M_\odot$.

As follows from various studies, the radius of the bar is $r_{bar} = 2$–4.5 kpc, the ratio of the bar semiaxes in the plane of the disk is estimated to be 1.6–3, and the angle between the bar major axis and the solar direction is $\varphi_{bar} = 15°$–$35°$ [49–51]. To compare the modeling results with the observations, we shall adopt the values $\varphi_{bar} = 20°$ and $r_{bar} = 3.2$ kpc. Therefore, the dynamical model should allow the existence of a long-lived bar with a semiaxis ratio of $\gtrsim 1.6$. From this point of view, the models with a massive, concentrated bulge ($a_b \simeq 100$ pc) cannot explain the observed bar. Even if the bar begins to appear during the early evolution of a cold disk, it is later disrupted due to scattering on the central potential of the bulge.

The sharp central maximum of the circular velocity V_c cannot be explained in models with $a_n \gtrsim 200$ pc and $M_b \simeq 10^{10} M_\odot$; however, the observed and model central velocity dispersions can be brought into agreement, and the formation of a long-lived bar is possible. Contours of equal surface density and velocity dispersion in the presence of a central bar are plotted in Figs. 5a–5c. Due to the specific nature of the motion of matter in the vicinity of the bar, the model central stellar rotational velocities are substantially different along the major and minor axes (Fig. 5d). The x component of the model stellar rotational velocity V_* displays a characteristic maximum near the center (which is absent in the direction from the Sun to the Galactic center, i.e., in the y direction).

Therefore, if we do not assume that $V_c = V_{\mathrm{gas}}$ near the central peak in the rotation curve, we can (i) obtain agreement with the observed central stellar-velocity dispersion and (ii) explain the existence of a long-lived bar. The local velocity maximum could be due to motion in the asymmetric potential near the bar or to the presence of an inner disk or ring [53]. Note also that the King model for the matter density in the bulge is in better agreement with the infrared photometric profile (from *COBE/DIRBE* data) at 100 pc $\lesssim r \lesssim 1$ kpc [52] for $a_b \gtrsim 0.2$ kpc than for $a_b \simeq 0.1$ kpc.

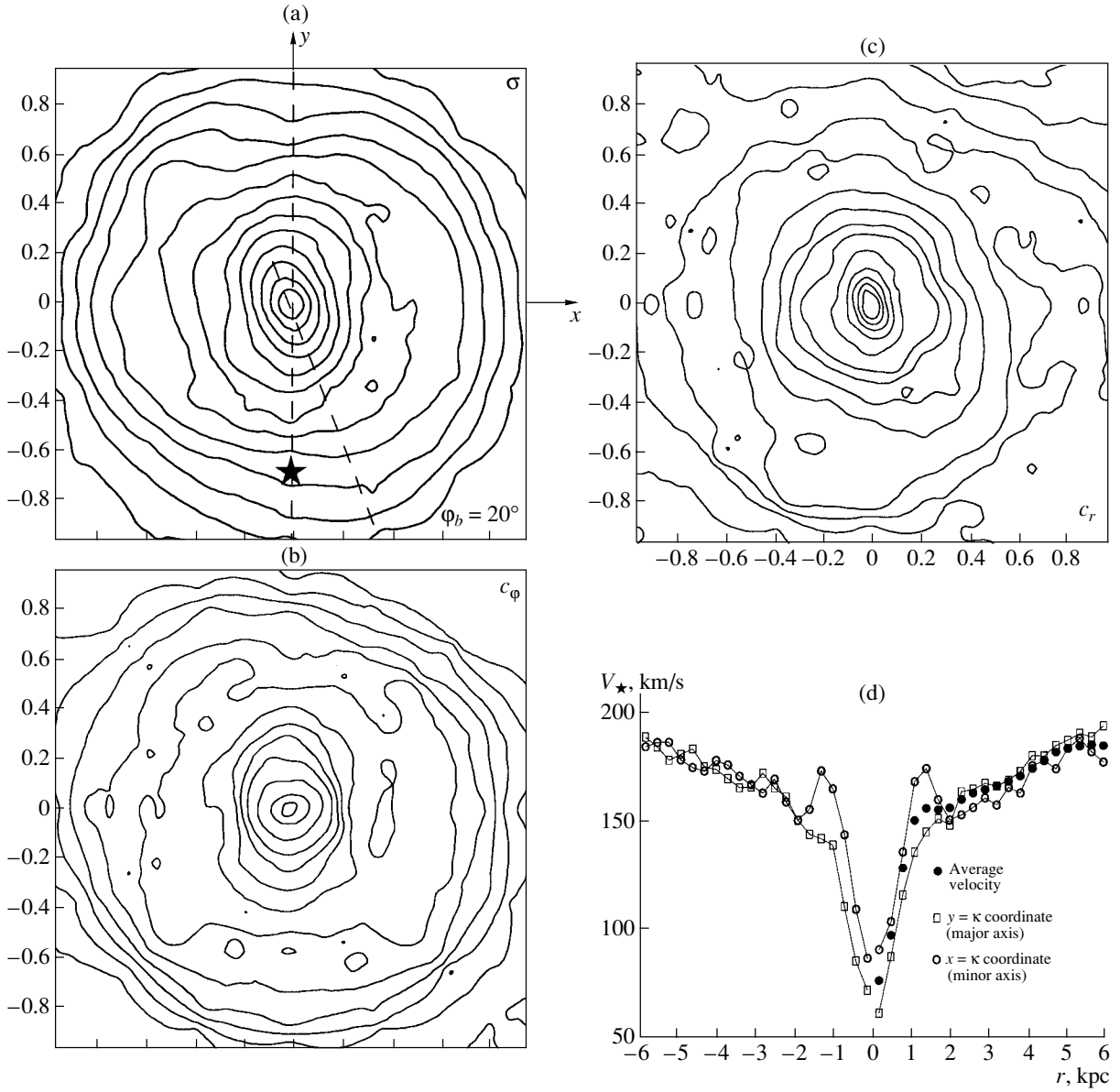

Fig. 5. Properties of the disk with bar in the Galaxy. (a) Surface-density distribution in the plane of the disk $\sigma(x, y)$. The asterisk denotes the position of the Sun. The angle between the bar's major axis and the line passing through the disk center and the solar neighborhood is $\varphi_{bar} = 20°$. (b) Contours of equal azimuthal-velocity dispersion in the disk $c_\varphi(x, y)$. (c) Contours of equal radial-velocity dispersion in the disk $c_r(x, y)$. (d) Rotational velocity of the disk matter V_* as a function of distance from the center in various directions: $V_*(x)$ (open circles) and $V_*(y)$ (squares). The coordinates x and y correspond to those in Fig. 5a. The rotational velocity averaged in azimuth is shown by the solid circles.

5. DISTRIBUTION OF MATTER IN THE DISK

In accordance with Section 4.1, we shall assume that the circular velocity does not have any significant local minima in the outer regions of the Galaxy. Therefore, we shall consider exponential surface-density profiles $\sigma(r) = \sigma_0 \exp(-r/L)$ with $L = \text{const}$ in the region $r < R_\odot$. Models showing deviations from an exponential law beyond the solar orbit will be considered separately. The observations do not enable us to determine the radial scale L with certainty, and estimates cover a broad interval $L = 2$–5 kpc (see [51–58] and references therein). Infrared observations provide relatively reliable estimates of the disk radial scale ($L = 2$–3.5 kpc). Accordingly, we will adopt $L = 3$ kpc for our basic model, with the bulge being described by the King model (1) with $a_b = 0.2$ kpc and $\varrho_{b0} = 72 M_\odot/\text{pc}^3$.

5.1. Limits on the Surface Density

The stellar-velocity dispersion is one of the most accurately known disk parameters in the solar neighborhood. In accordance with [26], we shall use the values $(c_r, c_\varphi, c_z) = (38, 24, 20)$ km/s for the oldest stellar population.

Figure 6a shows the model dependence of the stellar radial-velocity dispersion on the surface density in the solar neighborhood $\sigma_\odot$ when gravitational stability of the disk is achieved for a specified halo mass. The results for $L = 3$ kpc are marked by the symbol $\star$. The derived value of c_r clearly exceeds the observed value $c_r = 38$ km/s when the surface density is large, $\sigma_\odot \gtrsim 70 M_\odot/\mathrm{pc}^2$. On the other hand, there is a considerable margin of stability if the surface density is small, $\sigma_\odot \lesssim 40 M_\odot/\mathrm{pc}^2$. The best agreement between the model and observations is achieved for $\sigma_\odot \simeq 58 M_\odot/\mathrm{pc}^2$. In this case, the halo scale is approximately twice the radial disk scale: $a_h/L = 6.3$ kpc/3 kpc (Fig. 6b), and the halo mass within a radius $R_\odot = 8$ kpc will be $M_h = 3 \times 10^{10} M_\odot$, i.e., about 87% of the disk mass (Fig. 6c). The total mass of the disk in this model reaches $4.4 \times 10^{10} M_\odot$ (within 12 kpc), and the central surface density is $\sigma_0 = 840 M_\odot/\mathrm{pc}^2$. The contribution of the disk to the circular velocity at $r = 2.2L$ is $(V_c^{disk}/V_c)\big|_{r=2.2L} = 0.73$ (this is the radius where V_c^{disk} is maximum for an exponential surface-density profile). The contribution of the bulge to the circular velocity at radius $r = 2.2L$ is $(V_c^{bulge}/V_c)\big|_{r=2.2L} = 0.43$. Note that a similar result, $(V_c^{disk}/V_c)\big|_{r=2.2L} = 0.76$, was obtained in the dynamical model of Fux [24] for $L = 3$ kpc.

The relative halo mass within $r = 4L = 12$ kpc was found to be $\mu = M_h/M_d = 1.6$, in agreement with the analysis of the vertical structure of the disk of [59] ($\mu = 1.8$). Our Galaxy is a typical system, in which the dark halo not only determines the kinematics of outer regions but also plays an appreciable dynamical role in the stellar disk ($r < 4L = 12$ kpc). The estimate of the disk surface density $\sigma_\odot = 58 M_\odot/\mathrm{pc}^2$ indicates the dominant contribution of the disk to the vertical force balance. On the other hand, the observational data show a considerable scatter for the surface density in the solar neighborhood: $\sigma_\odot = 39\text{–}71 M_\odot/\mathrm{pc}^2$, although the most trustworthy values are in the range $50\text{–}60 M_\odot/\mathrm{pc}^2$ [22].

The measured radial disk scale is $L = 3 \pm 1$ kpc [22] for models with both thin and thick disks. If the disk scale L is varied in the dynamical models but the ratio $L/R_\odot$ is fixed, all our conclusions for the ratio $\mu = M_h/M_d$ remain valid, although the absolute masses of the components change.

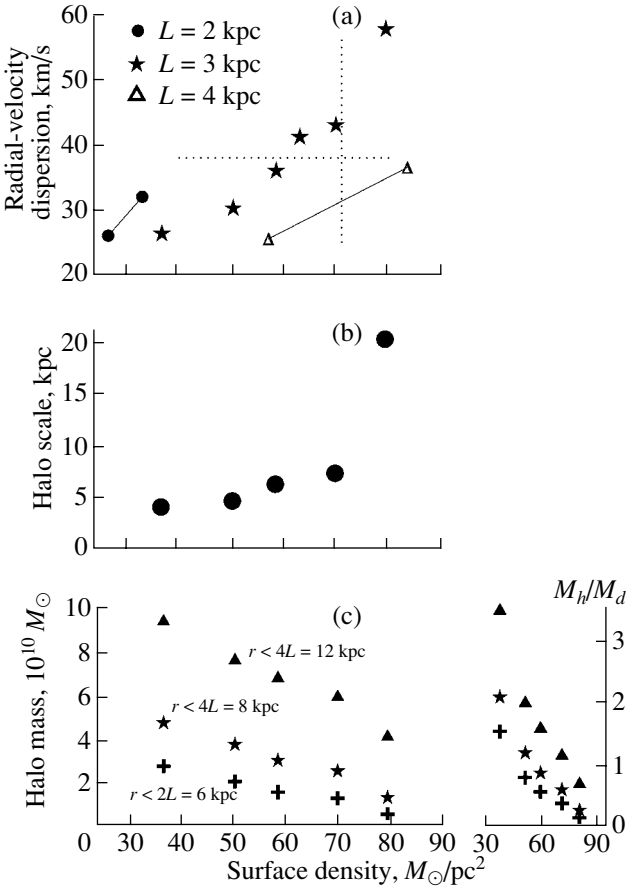

Fig. 6. Dependence of the model parameters on the disk surface density at $R_\odot = 8$ kpc. (a) Radial-velocity dispersion for various radial disk scales $L = 2$, 3, and 4 kpc. The horizontal line shows the observed value $c_r = 38$ km/s. The vertical line corresponds to the surface density of matter $\sigma_\odot = 71 \pm 6 M_\odot/\mathrm{pc}^2$ located within $|z| < 1.1$ kpc [61]. (b) The halo scale a_h in accordance with (1) for a series of models with $L = 3$ kpc. (c) The halo mass M_h and ratio of the halo mass to the disk mass within various radii ($r = 6$ kpc$= 2L$, $r = 8$ kpc, $r = 12$ kpc$= 4L$).

Let us consider models with a larger disk scale, $L = 4$ kpc (Fig. 6a). The results show that the disk is at the stability limit when the surface density $\sigma_\odot$ is $\simeq 80 M_\odot/\mathrm{pc}^2$, in contradiction to the observations [51, 60, 61]. Agreement between the observed and model surface densities can be achieved only if we suppose that the disk possesses a considerable margin of gravitational stability: $\Delta c_r = c_r^{obs} - c_r = (38 - 26)$ km/s$= 12$ km/s. If the entire disk is taken into consideration (rather than only the solar neighborhood), the agreement between the radial distributions c_r and c_r^{obs} in the models with $L = 4$ kpc turns out to be substantially worse than in the models with $L = 3$ kpc.

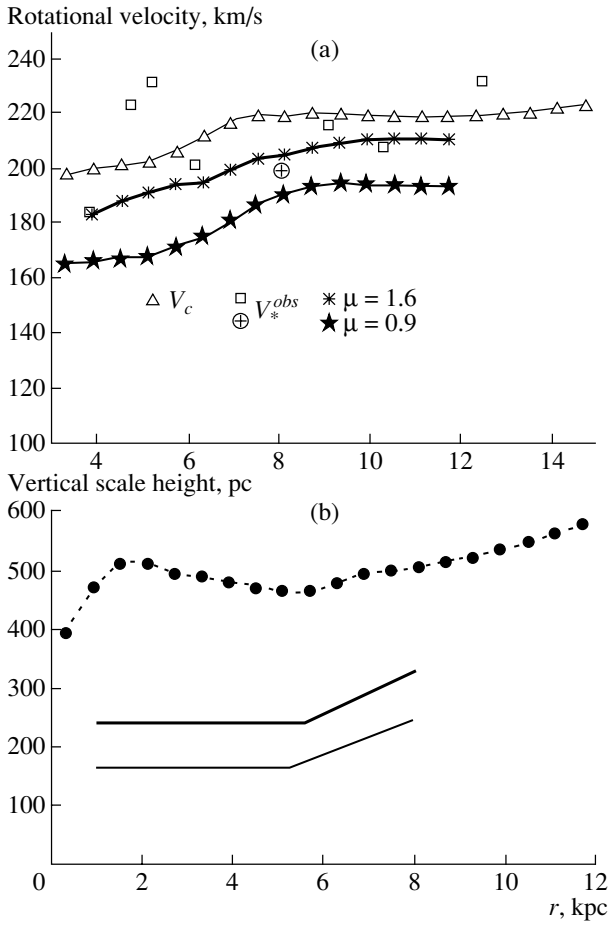

Fig. 7. (a) Rotational velocity of stars in the disk V_*^{obs} for the data of [2] (squares) and [7] (circled crosses). The thick and thin curves correspond to the models with $\mu = 1.6$ and $\mu = 0.9$. The circular velocity is plotted as triangles. (b) Radial dependence of the vertical disk scale height Δ in the model with $\mu = 1.6$ (solid circles). The solid lines delimit the observed distributions of the exponential vertical scale height h_{exp}.

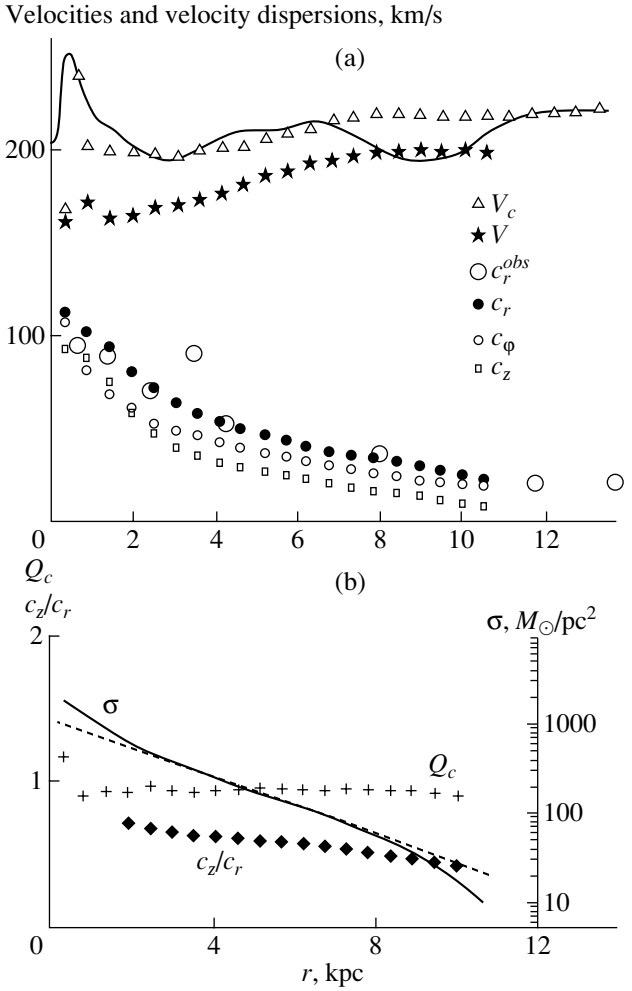

Fig. 8. Radial dependences of the disk parameters for the best-fitting dynamical model of the Galaxy compared to the observational data. (a) Kinematic parameters: the rotation curve (solid curve), circular velocity V_c, model disk rotational velocity V, observed velocity dispersion c_r^{obs}, and model velocity dispersions c_r, c_φ, and c_z. (b) Radial dependences of the ratio c_z/c_r (diamonds) and the parameter Q_c (crosses) [left-hand axis], and also the surface density σ (solid and dotted curves, right-hand axis).

Using the short scale $L = 2$ kpc and the fixed value $R_\odot = 8$ kpc, we obtain $c_r = 32$ km/s at the stability limit, even in the maximum-disk model, for which $(V_c^{disk}/V_c)\big|_{r=2.2L} = 0.89$. Thus, the surface density is low, $\sigma_\odot = 33 M_\odot/\ \mathrm{pc}^2$ (Fig. 6a). The mass of the spheroidal subsystem within $r < 4L = 8$ kpc is only 63% of the disk mass. Consequently, there is a margin of stability, since it is possible to increase $\sigma_\odot$ to $50 M_\odot/\ \mathrm{pc}^2$ (and the corresponding radial-velocity dispersion to the observed value, $c_r^{obs} = 38$ km/s) for the given rotation curve. Therefore, the models with $L = 3$ kpc are in better agreement with the entire set of observational data than those having disks with scales of $L = 2$ kpc or $L = 4$ kpc.

In the dynamical model that is in agreement with the observed rotation curve for the cold component, the stellar rotational velocity, and the velocity dispersions in the old disk, the total volume density at radius $R_\odot = 8$ kpc is $\varrho_\odot = 0.068 M_\odot/\mathrm{pc}^3$, with the disk component comprising $\varrho_\odot^{disk} = 0.058 M_\odot/\mathrm{pc}^3$). The difference $\varrho_\odot^s = \varrho_\odot - \varrho_\odot^{disk} = 0.01 M_\odot/\mathrm{pc}^3$ corresponds to the contribution of the spheroidal component (the halo and thick disk). This volume density is consistent with the most recent observations, $\varrho_{\odot,obs} = 0.076 \pm 0.015 M_\odot/\mathrm{pc}^3$ [62]. If the disk surface density in the solar neighborhood is only $\sigma_\odot^{obs} = 40 M_\odot/\mathrm{pc}^2$ [63], we expect there to be a margin of gravitational stability in the stellar disk and a larger halo mass relative to the disk within $r = 8$ kpc.

5.2. Rotational Velocity of the Old Disk

The dynamical models clearly demonstrate that the difference between the circular velocity V_c and the rotational velocity of the matter in the stellar disk V_* increases as the halo mass decreases, due to the larger contribution of the thermal motion of the stars to the radial force balance. Therefore, the difference between the circular velocity and the rotational velocity of the old population can be used to derive an independent estimate of the disk mass. According to the observations of [2], the rotational velocity of the old stellar population at $r > 5$ kpc exceeds 200 km/s. The stellar rotational velocity in the $z = 0$ plane in the solar neighborhood was found in [7] to be 200 km/s. Therefore, the difference between the rotational velocities of the youngest and oldest stars is less than 20 km/s. This provides an additional argument in favor of a stellar disk with a moderate mass (Fig. 7a). If the disk contributes more than 70% of the mass inside the solar orbit, the difference between the circular velocity V_c and the rotational velocity of the old stellar disk V can be no smaller than 30 km/s (the model with $\mu = 0.9$ in Fig. 7a).

5.3. Vertical Scale Height of the Stellar Disk

The following exponential law is often used to approximate the vertical profile of the volume disk density:

$$\varrho(z) = \varrho_0 \exp(-z/h_{exp}), \qquad (8)$$

where h_{exp} is the vertical exponential scale height of the disk. Estimates of $(h_{exp})_\odot$ for the old disk range from 200 pc to 350 pc [64–66], and the gradient of the vertical scale height in the radial direction may be positive [55, 56]. For example, according to the data of [52], $h_{exp} < 210$ pc in the central region. The vertical scale height of the old disk found in [7] after subtracting the contribution of stars in the thick disk is $h_{exp} \simeq 330$ pc. The vertical distribution of M dwarfs is better approximated by the combined law $\varrho \propto 0.8 \times \mathrm{ch}^{-2}(z/323\ \mathrm{pc}) + 0.2 \times \exp(-|z|/656\ \mathrm{pc})$ [63], which roughly corresponds to $z_0 = 400$ pc for the law (3) at $|z| < 1$ kpc. However, the surface density of M dwarfs does not exceed $\sigma = 14 M_\odot/\mathrm{pc}^2$ and represents a smaller fraction of the total disk density [63].

Figure 7b presents the radial dependence of the parameter

$$\Delta^2 = \frac{\int_{-\infty}^{\infty}(z - \langle z\rangle)^2 \varrho(z) dz}{\int_{-\infty}^{\infty} \varrho(z) dz} \qquad (9)$$

derived in the dynamical model that provides a satisfactory description of the distribution of the kinematic parameters of the old disk ($\langle \ldots \rangle$ denotes averaging over z). The numerical value of Δ determined using (9) nearly coincides with the disk half-thickness z_0 in the vertical-density law $\varrho \propto \mathrm{ch}^{-2}(z/z_0)$ [27]. Since both these z density distributions possess the same asymptotics at large distances from the plane $z = 0$, we can approximate $z_0 \simeq 2h_{exp}$. The nonmonotonic behavior of Δ in the central region is due to the bar. The increase in the vertical scale height with radius in the outer regions is characteristic of many galaxies, including our own [67].

5.4. Stellar-Velocity Ellipsoid (c_r, c_φ, c_z)

Figure 8a presents the radial dependences of the parameters of the dynamical model that provides the best agreement with the observed distribution of the stellar-velocity dispersion in the solar neighborhood, $(c_r, c_\varphi, c_z) = (38, 24, 20)$ km/s [26] and, consequently, $c_r/c_\varphi = 1.58$, $c_z/c_r = 0.53$.

The surface-density profile $\sigma(r)$ and the parameters $Q_c \equiv c_r \varkappa/2\Omega c_\varphi$ and c_z/c_r for this model are shown in Fig. 8b. An exponential profile with the scale $L = 2.8$ kpc is plotted by the dotted curve. The dispersion ratio $Q_z = c_z/c_r$ decreases monotonically with radius, where $Q_z(r = 0) \simeq 0.8$. In the outer regions of the Galaxy, beyond the solar orbit, this parameter can be as small as $Q_z(r > 10\ \mathrm{kpc}) \simeq 0.4$.

There is reason to believe that the halo is a flattened system with the density distribution $\varrho_h \propto 1/(1 + (r/a_h)^2 + (z/qa_h)^2)$, where $q < 1$ [12]. If the halo is not spherical, then all the halo masses obtained in the present work should be treated as lower limits.

6. DISCUSSION AND CONCLUSIONS

Taking into account the stellar-velocity dispersions jointly with the Galactic rotation curve has enabled us to narrow the range of admissible values for the disk mass. The assumption that the disk component is close to the gravitational-stability limit imposes constraints on the distributions of matter in various subsystems and on the kinematic parameters of the disk. We have constructed a series of dynamical models of the Galaxy with various masses for the disk, bulge, and halo and with a range of radial and vertical disk scales. The fits of the parameters of the dynamical models to the observational data leads us to draw the following conclusions.

(1) To explain the local velocity minimum at $6\ \mathrm{kpc} \lesssim r \lesssim 12$ kpc, we must assume that the surface density changes by over a factor of two within a narrow zone with width ~ 0.5 kpc at a radius of $r \simeq 6$ kpc. The observed relation between the radial- and azimuthal-velocity dispersions indicates that

the rotational velocity in the solar neighborhood is nearly independent of radius. Therefore, the observed local minimum in the rotation curve formed by the gaseous subsystem and young stars does not reflect the behavior of the circular velocity.

(2) The presence of a well-defined maximum of the circular velocity V_c in the central region ($r \lesssim 1$ kpc) imposes constraints on the lifetime of the bar and the stellar-velocity dispersion in the central region of the disk. The constructed dynamical models limit the scale of the bulge nucleus to $a_n \gtrsim 200$ pc, with the resulting total mass of the bulge being $M_b \lesssim 1.2 \times 10^{10} M_\odot$. Our results show that the central maximum of the rotation curve at $r \simeq 200$–300 pc is not due to the distribution of matter in the bulge and is probably associated with the presence of the bar. Therefore, we cannot equate the rotational velocity $V_{\rm gas}$ to the circular velocity V_c in order to estimate the masses of the various subsystems in the central region of the Galaxy. Another possible explanation for the sharp maximum in the circular velocity in the central region is that it is associated with an inner disk with a sharp boundary [23, 53].

(3) The best agreement with the observed distributions of the stellar-velocity dispersions is achieved in models in which the surface density in the solar neighborhood is $\sigma_\odot \leq 58\ M_\odot/\mathrm{pc}^2$, with the corresponding total mass of the disk being $M_d \leq 4.4 \times 10^{10} M_\odot$. The relative mass of the halo at $r \leq 8$ kpc is $(M_h/M_d)\big|_{r<8\ \mathrm{kpc}} = 0.87$. The contribution of the disk component to the circular velocity at $r = 2.2L$ (where the circular velocity of the exponential disk is maximum) is $V_c^{disc}/V_c = 0.73$.

(4) The model with a radial exponential disk scale of $L = 3$ kpc and a vertical scale height of $z_0 = 0.5$ kpc can explain the entire set of observational data better than models with either $L = 2$ kpc or $L = 4$ kpc.

ACKNOWLEDGMENTS

This work was supported by the Russian Foundation for Basic Research (project no. 01-02-17597). We are grateful to A.S. Rastorguev for numerous consultations, A.V. Zasov for fruitful and stimulating discussions, I.I. Nikiforov for kindly presenting his data, and A.M. Fridman for valuable comments.

REFERENCES

1. D. P. Clemens, Astrophys. J. **295**, 422 (1985).
2. J. R. Lewis and K. C. Freeman, Astron. J. **97**, 139 (1989).
3. J. Brand and L. Blitz, Astron. Astrophys. **275**, 67 (1993).
4. Y. Sofue, Astrophys. J. **458**, 120 (1996).
5. A. S. Rastorguev, E. V. Glushkova, A. K. Dambis, and M. V. Zabolotskikh, Pis'ma Astron. Zh. **25**, 689 (1999) [Astron. Lett. **25**, 595 (1999)].
6. Y. Sofue, Y. Tutui, M. Honma, *et al.*, Astrophys. J. **523**, 136 (1999).
7. T. C. Beers and J. Sommer-Larsen, Astrophys. J., Suppl. Ser. **96**, 175 (1995).
8. M. Schmidt, Stars Stell. Syst. **4**, 513 (1965).
9. J. A. R. Caldwell and J. P. Ostriker, Astrophys. J. **251**, 61 (1981).
10. K. Rohlfs and J. Kreitsehmann, Astrophys. Space Sci. **79**, 289 (1981).
11. B. Dauphole and J. Colin, Astron. Astrophys. **300**, 117 (1995).
12. R. P. Olling and M. R. Merrifield, Mon. Not. R. Astron. Soc. **311**, 361 (2000).
13. A. Toomre, Astrophys. J. **139**, 1217 (1964).
14. A. G. Morozov and A. V. Khoperskov, Astrofizika **24**, 467 (1986).
15. V. L. Polyachenko, E. V. Polyachenko, and A. V. Strel'nikov, Pis'ma Astron. Zh. **23**, 598 (1997) [Astron. Lett. **23**, 525 (1997)].
16. A. V. Khoperskov, A. V. Zasov, and N. V. Tyurina, Astron. Zh. **78**, 213 (2001) [Astron. Rep. **45**, 180 (2001)].
17. V. L. Polyachenko and I. G. Shykhman, Pis'ma Astron. Zh. **3**, 254 (1977) [Sov. Astron. Lett. **3**, 134 (1977)].
18. A. V. Zasov, D. I. Makarov, and E. A. Mikhailova, Pis'ma Astron. Zh. **17**, 884 (1991) [Sov. Astron. Lett. **17**, 374 (1991)].
19. A. G. Morozov, Astron. Zh. **58**, 734 (1981) [Sov. Astron. **25**, 421 (1981)].
20. J. N. Bahcall and R. M. Soneira, Astrophys. J., Suppl. Ser. **44**, 73 (1980).
21. A. A. Sumin, A. M. Fridman, and U. A. Khaud, Pis'ma Astron. Zh. **17**, 698 (1991) [Sov. Astron. Lett. **17**, 295 (1991)].
22. P. D. Sackett, Astrophys. J. **483**, 103 (1997).
23. A. A. Sumin, A. M. Fridman, and U. A. Khaud, Pis'ma Astron. Zh. **17**, 779 (1991) [Sov. Astron. Lett. **17**, 329 (1991)].
24. R. Fux, Astron. Astrophys. **327**, 983 (1997).
25. R. Fux, Astrophys. Space Sci. **276**, 367 (2001).
26. W. Dehnen and J. J. Binney, Mon. Not. R. Astron. Soc. **298**, 387 (1998).
27. J. N. Bahcall, Astrophys. J. **276**, 156 (1984).
28. J. E. Barnes and P. Hut, Astrophys. J., Suppl. Ser. **70**, 389 (1989).
29. A. M. Fridman, O. V. Khoruzhii, and A. E. Piskunov, in *Physics of the Gaseous and Stellar Disks of the Galaxy*, ASP Conf. Ser. **66**, Ed. by I. R. King (Astronomical Society of the Pacific, San Francisco, 1994), p. 215.
30. A. C. Quillen and D. R. Garnett, in *Galaxy Disks and Disk Galaxies*, ASP Conf. Ser. **230**, Ed. by J. G. Funes and S. J. Corsini (Astronomical Society of the Pacific, San Francisco, 2001), p. 87; astro-ph/0004210.

31. E. A. Mikhailova, A. V. Khoperskov, and S. S. Sharpak, in *Stellar Dynamics: From Classic to Modern*, Ed. by L. P. Ossipkov and I. I. Nikiforov (St. Petersburg, 2001), p. 147.
32. L. H. Amaral, R. Ortiz, J. R. D. Lepine, and W. J. Maciel, Mon. Not. R. Astron. Soc. **281**, 339 (1996).
33. A. K. Dambis, A. M. Mel'nik, and A. S. Rastorguev, Pis'ma Astron. Zh. **21**, 331 (1995) [Astron. Lett. **21**, 291 (1995)].
34. I. I. Nikiforov, in *Stellar Dynamics: From Classic to Modern*, Ed. by L. P. Ossipkov and I. I. Nikiforov (St. Petersburg, 2001), p. 28.
35. A. K. Dambis, A. M. Mel'nik, and A. S. Rastorguev, Pis'ma Astron. Zh. **27**, 68 (2001) [Astron. Lett. **27**, 58 (2001)].
36. A. S. Rastorguev, M. V. Zabolotskikh, and A. K. Dambis, Astron. Lett. **28**, 454 (2002).
37. I. I. Nikiforov, *IAU Coll. 174: Small Galaxy Groups*, ASP Conf. Ser. **209**, Ed. by M. J. Valtonen and C. Flynn (Astronomical Society of the Pacific, San Francisco, 2000), p. 403.
38. P. C. van der Kruit and L. Searle, Astron. Astrophys. **95**, 116 (1981).
39. P. C. van der Kruit, in *Galaxy Disks and Disk Galaxies*, ASP Conf. Ser. **230**, Ed. by J. G. Funes and E. M. Corsini (Astronomical Society of the Pacific, San Francisco, 2001), p. 119.
40. A. V. Barabanov and A. V. Zasov, Astron. Zh. **56**, 252 (1979) [Sov. Astron. **23**, 138 (1979)].
41. A. M. N. Ferguson and C. J. Clarke, Mon. Not. R. Astron. Soc. **325**, 781 (2001).
42. W. Dehnen, Astron. J. **115**, 2384 (1998).
43. S. Frink, B. Fuchs, S. Roser, and R. Wiellen, Astron. Astrophys. **314**, 430 (1996).
44. H. Hasan and C. Norman, Astrophys. J. **361**, 69 (1990).
45. R. D. Blum, J. S. Carr, D. L. DePoy, *et al.*, Astrophys. J. **422**, 111 (1994).
46. R. D. Blum, J. S. Carr, K. Sellgren, and D. M. Terndrup, Astrophys. J. **449**, 623 (1995).
47. R. M. Rich, Astrophys. J. **362**, 604 (1990).
48. D. Minniti, S. D. M. White, E. W. Olszewski, and J. M. Hill, Astrophys. J. **393**, L47 (1992).
49. K. Z. Stanek, A. Udalski, M. Szymaski, *et al.*, Astrophys. J. **477**, 163 (1997).
50. B. J. Weiner and J. A. Sellwood, Astrophys. J. **524**, 112 (1999).
51. O. E. Gerhard, in *Galaxy Disks and Disk Galaxies*, Ed. by J. G. Funes and E. M. Corsini (Astron. Soc. of the Pacific, San Francisco, 2001), p. 21.
52. J. Binney, O. Gerhard, and D. Spergel, Mon. Not. R. Astron. Soc. **288**, 365 (1997).
53. A. M. Fridman, in *Physics of the Gaseous and Stellar Disks of the Galaxy*, ASP Conf. Ser. **66**, Ed. by I. R. King (Astronomical Society of the Pacific, San Francisco, 1994), p. 15.
54. T. J. Jones, M. Ashley, A. R. Hyland, and A. Ruelas-Mayorga, Mon. Not. R. Astron. Soc. **197**, 413 (1981).
55. S. M. Kent, T. M. Dame, and G. Fazio, Astrophys. J. **378**, 131 (1991).
56. R. Fux and L. Martinet, Astron. Astrophys. **287**, L21 (1994).
57. H. T. Freudenreich, Astrophys. J. **492**, 495 (1998).
58. P. L. Hammersley, M. Cohen, F. Garzon, *et al.*, Mon. Not. R. Astron. Soc. **308**, 333 (1999).
59. J. N. Bahcall and S. Casertano, Astrophys. J. **284**, L35 (1984).
60. A. Gould, Mon. Not. R. Astron. Soc. **244**, 25 (1990).
61. K. Kuijken and G. Gilmore, Astrophys. J. Lett. **367**, L9 (1991).
62. M. Creze, E. Chereul, O. Bienayme, and C. Pichon, Astron. Astrophys. **329**, 920 (1998).
63. A. Could, J. N. Bahcall, and C. Flynn, Astrophys. J. **465**, 759 (1996).
64. N. I. Reid and S. R. Majewski, Astrophys. J. **409**, 635 (1993).
65. M. Haywood, A. C. Robin, and M. Creze, Astron. Astrophys. **320**, 440 (1997).
66. A. Vallenari, G. Bertelli, and L. Schmidtobreick, Astron. Astrophys. **361**, 73 (2000).
67. C. Alard, Mon. Not. R. Astron. Soc. (2001); astro-ph/0007013.

Translated by Yu. Dumin

Astronomy Reports, Vol. 47, No. 6, 2003, pp. 458–466. Translated from Astronomicheskiĭ Zhurnal, Vol. 80, No. 6, 2003, pp. 499–507.

Radio and Optical Spectral Studies of Radio Sources

V. L. Afanas'ev[1], S. N. Dodonov[1], A. V. Moiseev[1], A. G. Gorshkov[2], V. K. Konnikova[2], and M. G. Mingaliev[1]

[1]*Special Astrophysical Observatory, Nizhniĭ Arkhyz, Russia*

[2]*Sternberg Astronomical Institute, Universitetskiĭ pr. 13, 119992 Moscow, Russia*

Received March 26, 2002; in final form, January 15, 2003

Abstract—Optical identifications and an analysis of the radio spectra of eight radio sources from a flux-density-complete sample at declinations 4°–6° (B1950) are presented. The observations were carried out at 4000–9000 Å on the 6-m telescope of the Special Astrophysical Observatory and at 0.97–21.7 GHz on the RATAN-600 telescope. Five of the eight sources are quasars and three are emission-line radio galaxies.

1. INTRODUCTION

This paper presents results of optical identifications of radio sources from a sample complete to a specified flux density. This work is targeted at deriving the radio luminosity function of the sample objects and its cosmological dependences. This requires that the redshifts of the majority of the sample objects be known.

All the objects whose spectra are presented here are optical counterparts of radio sources from a complete sample derived from the Zelenchuk survey at 3.9 GHz. This sample, which we have studied since 1980, contains all sources with fluxes $S_{3.9} > 200$ mJy, declinations 4°–6° (B1950), right ascensions 0–24 h, and Galactic latitudes $|b| > 10°$ [1–3]. Currently, approximately 75% of the flat-spectrum sources in the sample have been optically classified. Previous results on optical identifications of the sample objects are published in [4–6].

2. RADIO AND OPTICAL OBSERVATIONS

Optical spectra of the objects were obtained in June and November 2000 on the 6-m telescope of the Special Astrophysical Observatory (SAO) of the Russian Academy of Sciences. The observations of 1522+0400 and 1600+0412 were obtained using a multipupil spectrograph (http://www.sao.ru/gafan/devices/mpfs/mpfs_main.htm) with a TK1024 CCD detector, which has 1024 × 1024 channels and a counting noise of three electrons. The wavelength range observed was 4000–9000 Å, with a dispersion of 5 Å/pixel. The effective instrumental resolution was about 15 Å. The spectra of the remaining objects were obtained using the multipurpose SCORPIO instrument (http://www.sao.ru/moisav/scorpio/scorpio.html) in its long-slit mode together with the same CCD detector; the wavelength range was 3800–9200 Å, with a dispersion of about 6 Å/pixel. The effective instrumental resolution was about 20 Å. The spectra were reduced in the standard way using programs developed in the Laboratory of Spectroscopy and Photometry of the SAO.

Radio observations of the sample sources were carried out on the Southern sector of the RATAN-600 plane-reflector radio telescope at 3.9 and 7.5 GHz in 1980–1991 and on the Northern sector at 0.97, 2.3, 3.9, 7.7, 11.1, and 21.7 GHz in 1996–1999. The parameters of the receivers used on the Southern and Northern sectors are described in [1, 7], respectively, and the characteristics of the antenna beams for the Northern and Southern sectors are presented in [2, 8]. In each series of observations, the sources were observed daily for from 15 to 100 days.

The observations on the Northern sector of the RATAN-600 were obtained in a fixed-focus regime [9]. The position of the main mirror could be adjusted within elevations of ±1° from the center of the observation zone. An equal number of panels was used at all elevations, in order to reduce the influence of variations in the radiation of the edge panels in the presence of variations in the curvature of the circular reflector. The effective area of the antenna was taken to be constant at all elevations.

The source 2128+048 was used as a calibrator for all observations at declinations 4°–6°. The size of this radio source is much less than the horizontal section of the antenna beam at all frequencies, right up to 21.7 GHz. The flux density of 2128+048 was taken

1063-7729/03/4706-0458$24.00

Table 1. Object coordinates

Source name	Radio coordinates J2000.0		Optical–radio		Ref
	RA	DEC	ΔRA	ΔDEC	
0323+0446	03 23 14.72	+04 46 12.59	0.02^s	$0.01''$	JVAS
0323+0534	03 23 20.21	+05 34 11.20	0.05	1.10	NVSS
0354+0441	03 54 24.13	+04 41 07.27	−0.02	0.21	JVAS
0357+0542	03 57 46.13	+05 42 31.28	0	−0.04	JVAS
0427+0457	04 27 47.57	+04 57 08.34	0.02	−0.10	JVAS
1522+0400	15 22 32.76	+04 00 29.70	0.05	0.18	NVSS
1600+0412	16 00 02.54	+04 12 57.84	0	0.03	JVAS
2301+0609	23 01 53.46	+06 09 12.84	−0.02	0.03	JVAS

to be 4.25, 3.07, 2.35, 1.57, 1.24, and 0.75 Jy at 0.97, 2.3, 3.8, 7.7, 11.1, and 21.7 GHz, respectively.

The data were reduced using programs that enabled derivation of the flux density for an individual scan of a source, as well as determination of the mean flux density over the entire series of observations. The basis of the data reduction was optimal filtration of the input data using the method described in detail in [10]. Before this filtration, nonlinear filters were used to clean the input data of impulsive interference, jumps, and trends with time scales longer than the scale of the antenna beam in right ascension. When obtaining the mean flux densities for the entire observation time, we used only those recordings for which the noise dispersion at the location of the source was consistent with the noise properties of the total dataset; the method used to identify such recordings is described in [11].

We derived the mean flux density by applying optimal filtration to the average of the recordings, with the ith point for the filtration being the median of all the ith points for the cleaned input recordings. As a check, we also determined the mean flux density

$$\bar{S} = (\sum_i^n S_i)/n, \qquad (1)$$

where S_i is the flux density of the ith observation and n is the number of observations. There is no reason to introduce a weighting function here, since we are summing only those recordings that have already been determined to have noise characteristics consistent with those for the total dataset.

It is clear that the flux densities obtained in these two ways should be close and that substantial differences indicate the presence of a bad recording that has not been removed by the preliminary filtering. Our experience shows that significant differences are encountered only rarely, testifying to the correctness of the filtration algorithm applied. The few bad recordings that were still present are primarily those in which the antenna setup was incorrect. When significant flux-density differences were observed, we inspected all the corresponding recordings visually and removed any that appeared suspicious, then repeated the entire reduction procedure.

The measurement errors were also determined in two ways:

$$\sigma_\Sigma = \left(\sigma^2 / \sum_i A_i^2\right)^{\frac{1}{2}},$$

where σ^2 is the dispersion of the residual noise in the mean recordings after removing the detected source signal and A_i is the tabulated value of the antenna beam, and

$$\sigma_s = \left(\left(\sum_i^n (S_i - \bar{S})^2\right) \Big/ n(n-1)\right)^{\frac{1}{2}},$$

where $\bar{S}$ is the mean flux density derived using (1).

These two estimates should also be quite similar. If they corresponded to different distributions according to the Fisher criterion, we searched for bad recordings. In any case, we adopted the larger of the two estimates as the uncertainty in the measured flux density. In this approach, the resulting errors include the rms error in the flux density due to variability of the source during the series of observations.

3. RADIO AND OPTICAL COORDINATES

Table 1 presents the radio coordinates of the studied objects at epoch 2000.0 and the difference between the optical and radio coordinates for each object. We took the radio coordinates from the JVAS[1] catalog at 8.4 GHz [12] (rms coordinate error $0.014''$) and the NVSS[2] survey [13] at 1.4 GHz (average

[1] Jodrell Bank–VLA Astrometric Survey.
[2] NRAO VLA Sky Survey.

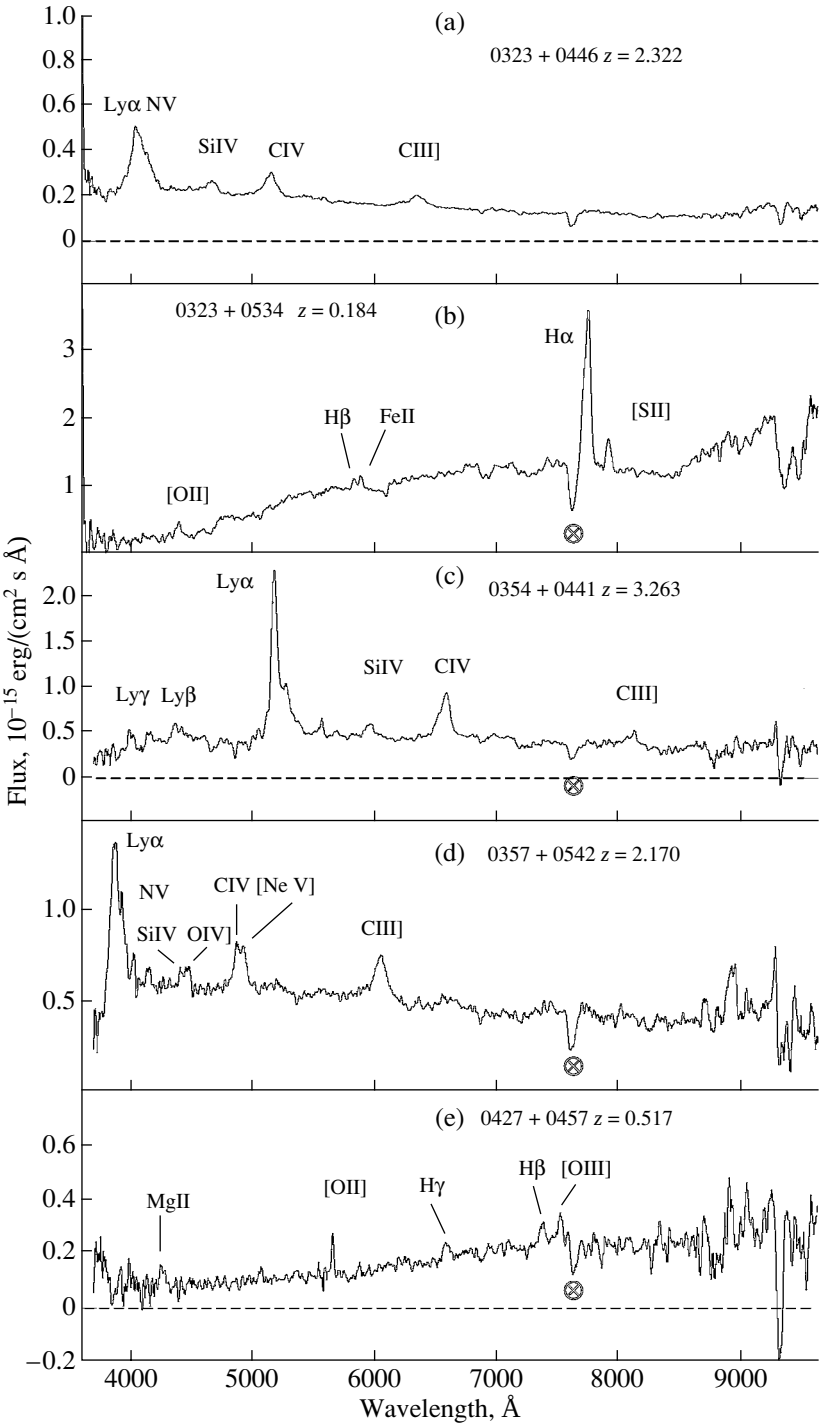

Fig. 1. Optical spectra of 0323+0446, 0323+0534, 0454+0441, 0357+0542, and 0427+0457 obtained on the 6-m telescope of the SAO.

rms errors about 0.11″ and 0.56″ in right ascension and declination, respectively). The source names are comprised of the hours and minutes of right ascension and degrees and minutes of declination corresponding to their coordinates. We obtained the optical coordinates from the USNO astrometric survey [14] or the Palomar Sky Survey APM database [15]. Taking into account the errors in both coordinates, the radio and optical coordinates for all the sources agree to within 3σ.

4. RESULTS

Figures 1–4 show optical and radio spectra of the objects.

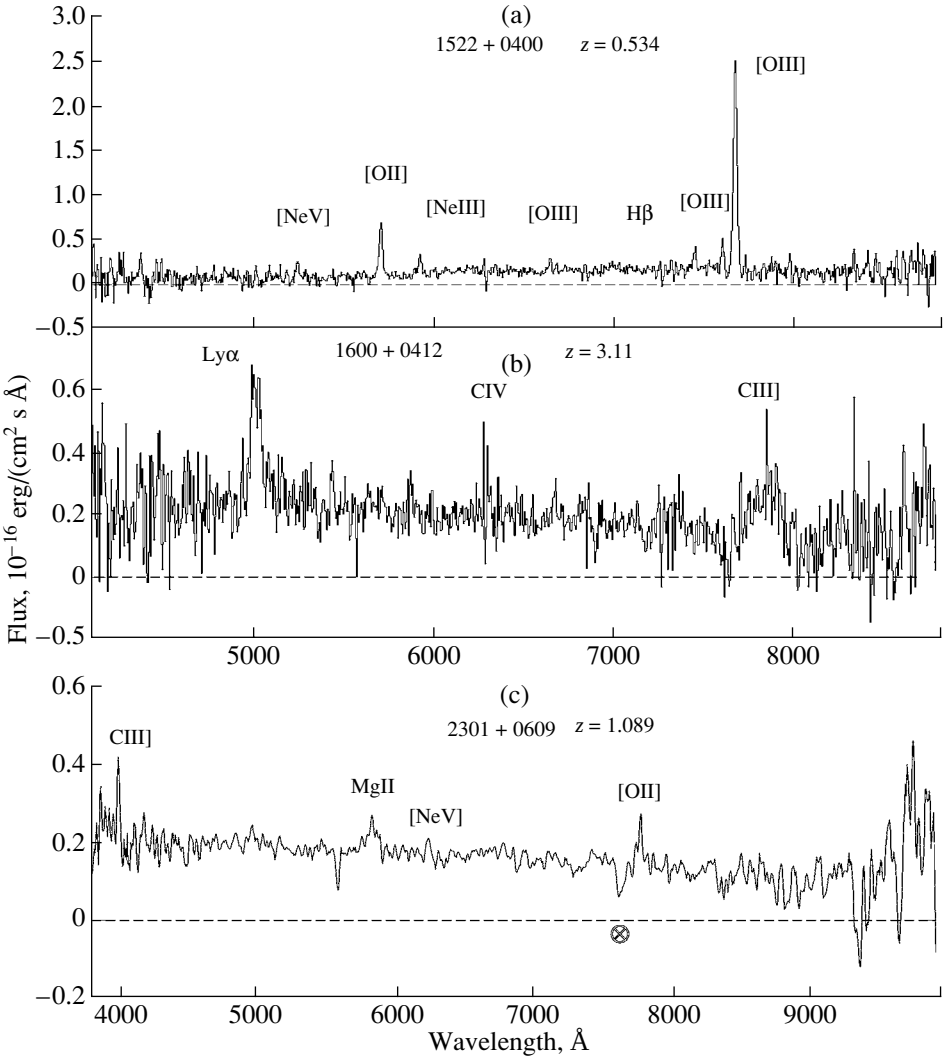

Fig. 2. Optical spectra of 1522+0400, 1600+0412, and 2301+0609 obtained on the 6-m telescope of the SAO.

Table 2 presents the optical data. The columns give (1) the source name, (2) lines present in the spectrum, (3) the rest-frame and observed wavelengths of these lines, (4) the corresponding redshift, (5) the classification of the object, (6) the observed B magnitude from [14, 15], (7) the observation date, and (8) the exposure in minutes.

Table 3 presents the flux densities of all the sources shown in Figs. 3 and 4. The columns give (1) the source name, (2)–(7) the flux densities and corresponding rms errors for 0.97, 2.3, 3.9, 7.7, 11.1, and 21.7 GHz in mJy, and (8) the observation epoch.

We present comments on individual sources below.

4.1. 0323+0446

The radio spectrum of this source, obtained in 1998 (Fig. 3a), falls off and then flattens toward higher frequencies. It can be approximated by the logarithmic parabola $\log S = -0.652 - 0.512 \log \nu + 0.171 \log^2 \nu$ (with the flux density in Jy and the frequency in GHz). The source does not display significant variability; over ten years of observations at 7.7 GHz obtained roughly once per year, the measured flux densities ranged from 135 ± 30 to 104 ± 4 mJy (covering a factor of 1.3 ± 0.3).

The optical spectrum had been obtained earlier at 4500–9000 Å using the 2.1-m telescope of the Guillermo Haro Observatory in Mexico. Based on the two lines CIV 1549 Å and CIII] 1909 Å, the object was classified as a quasar with a redshift of 2.322 [6]. Six lines can be identified in the optical spectrum obtained using the SAO 6-m telescope (Fig. 1a): a powerful, broad Lyα 1216 Å line (FWHM$\approx$ 130 Å), the NV 1240 Å line, the blended SiIV 1394,1403 Å doublet and OIV] 1406 Å line, and the CIV 1549 Å and

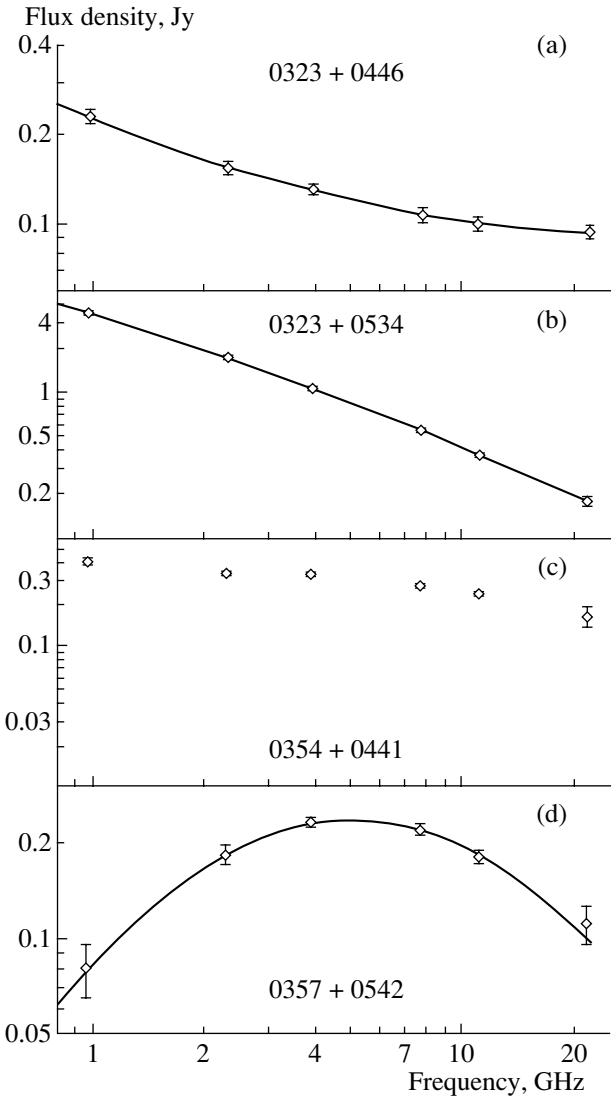

Fig. 3. Radio spectra of 0323+0446, 0323+0534, 0354+0441, and 0357+0542.

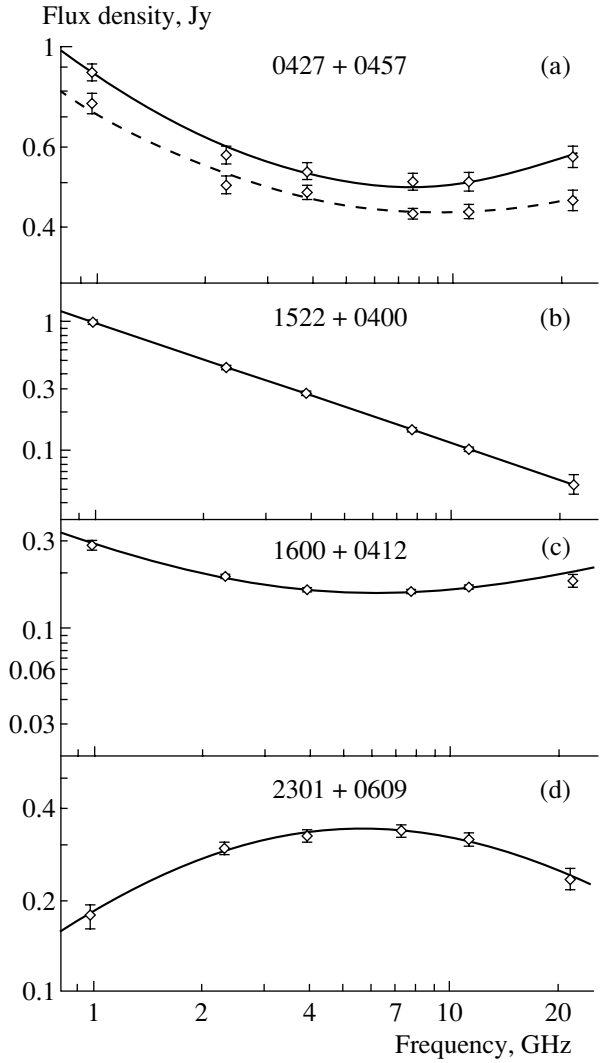

Fig. 4. Radio spectra of 0427+0457, 1522+0400, 1600+0412, and 2301+0609. The upper spectrum of 0427+0457 was obtained at epoch November 1997 and the lower at epoch July 1999.

CIII] 1909 Å lines. The redshift derived using all these lines is $z = 2.322 \pm 0.001$, confirming that the object is a quasar.

4.2. 0323+0534

The flux densities at 0.97–21.7 GHz are not variable, and the radio spectrum at 2.3–21.7 GHz is approximated well by the power law $S = 3976\,\nu^{-0.968}$ mJy (Fig. 3b). The spectrum flattens at lower frequencies. Based on the frequency of the turnover due to self-absorption ($\nu_m \approx 0.25$ GHz) and the flux density at this frequency ($S_m \approx 8$ Jy), we infer that the size of the radiating region exceeds 200 kpc (adopting the value H$= 10^{-4}$ Oe for the magnetic field in the jet).

Two Balmer lines—strong Hα 6563 Å and weak Hβ 4861 Å—can be identified in the optical spectrum (Fig. 1b), as well as the [OII] 3727 Å and FeII 4924 Å lines and the [SII] 6717, 6731 Å forbidden doublet. The widths of the hydrogen lines are FWHM$\approx$ 70 Å. All these lines are visible in emission, and the redshift is $z = 0.186 \pm 0.005$; the object is an emission-line radio galaxy.

4.3. 0354+0441

This source was observed in 1985 at 3.9 and 7.7 GHz. Figure 5a shows the flux-density variations at 7.7 GHz. Beginning in 1980, the flux density gradually decreased, reaching a minimum in 1995, after which it began to grow. The characteristic time

Table 2. Optical data

Source name	Lines present	Wavelength, Å	z	Spectral classification	B	Date	T, min
0323+0446	Lyα	1216/4040	2.322	QSO	19.1	Nov. 5, 2000	8
	SiIV/OIV]	1400/4650					
	CIV	1549/5145					
	CIII]	1909/6340					
0323+0534	[OII]	3727/4400	0.184	EmG	19.6	Nov. 4, 2000	10
	Hβ	4861/5820					
	FeII	4924/5890					
	Hα	6563/7760					
	[SII]	6724/7960					
0354+0441	Lyγ	973/4150	3.263	QSO	19.9	Nov. 4, 2000	10
	Lyβ	1026/4375					
	Lyα	1216/5185					
	NV	1240/5285					
	SiIV/OIV]	1400/5940					
	CIV	1549/6600					
	CIII]	1909/8135					
0357+0542	Lyα	1216/3865	2.170	QSO	19.6	Nov. 5, 2000	10
	NV	1240/3930					
	SiIV/OIV]	1400/4440					
	CIV	1549/4875					
	[NeV]	1575/4930					
	CIII]	1909/6056					
0427+0457	MgII	2798/4245	0.517	EmG	19.3	Nov. 5, 2000	10
	[OII]	3727/5654					
	Hγ	4340/6590					
	Hβ	4861/7375					
	[OIII]	4959/7522					
1522+0400	[NeV]	3426/5255	0.534	EmG	20.9	June 6, 2000	40
	[OII]	3727/5725					
	[NeIII]	3869/5930					
	[OIII]	4363/6655					
	Hβ	4861/7465					
	[OIII]	4959/7615					
	[OIII]	5007/7685					
1600+0412	Lyα	1216/5000	3.11	QSO	21.1	June 6, 2000	40
	CIV	1549/6320					
	CIII]	1909/7850					
2301+0609	CIII]	1909/4000	1.089	QSO	19.1	Nov. 2, 2000	10
	MgII	2798/5830					
	[NeV]	2973/6210					
	[OII]	3727/7780					

Table 3. Radio data

Source name	Flux densities and their errors, mJy						Epoch
	0.97 GHz	2.3 GHz	3.9 GHz	7.7 GHz	11.1 GHz	21.7 GHz	
0323+0446	230 21	149 06	132 05	105 06	97 05	95 06	01.1998
0323+0534	3568 52	1750 27	1070 10	556 06	380 07	190 12	07.1999
0354+0441	420 18	331 10	344 08	278 08	252 10	146 17	01.1998
0357+0542	80 15	182 11	232 09	220 07	181 06	112 15	07.1999
0427+0457	902 35	576 25	534 20	504 20	498 22	577 25	11.1997
	712 30	475 20	460 15	412 10	418 12	442 22	07.1999
1522+0400	1010 33	450 15	284 08	147 07	104 05	58 08	07.1999
1600+0412	289 15	189 07	159 05	163 06	172 07	182 16	01.1998
2301+0609	177 16	295 12	322 10	336 12	324 12	235 18	08.1997

scale for the variability (from maximum to minimum) is more than ten years. The 0.97–21.7 GHz spectrum in Fig. 3c was obtained in 1998 (diamonds). The spectrum is complex and cannot be approximated by a simple logarithmic parabola.

Three Lyman lines—Lyγ 973 Å, Lyβ 1026 Å, and powerful Lyα 1216 Å—can be identified in the optical spectrum (Fig. 1c), as well as the NV 1240 Å line, the blended SiIV 1394, 1403 Å doublet and OIV] 1406 Å line, and the CIV and CIII] 1549 and 1909 Å lines. The redshift derived using all the lines is $z = 3.263 \pm 0.002$, and we classified the object as a distant quasar.

4.4. 0357+0542

The 0.97–21.7 GHz spectrum of the source at epoch July 1999 can be well approximated with the logarithmic parabola $\log S = -1.076 + 1.266 \log \nu - 0.902 \log^2 \nu$; the spectral maximum is at 5.0 GHz, and the maximum flux density is 230 mJy (Fig. 3d). The source shows modest long-term variability. Observations at 7.7 GHz over 11 years obtained roughly once per year show flux-density variations from 275 ± 9 to 220 ± 5 mJy (covering a factor of 1.25 ± 0.05).

The optical spectrum (Fig. 1d) shows strong Lyα 1216 Å emission and the nearby NV line, the SiIV 1394, 1403 Å, doublet and the nearby OIV] 1406 Å line, the blended CIV 1549 Å and NeV 1575 Å lines, and the semiforbidden CIII] 1909 Å line at a redshift of $z = 2.17 \pm 0.007$. The object was classified as a quasar.

4.5. 0427+0457

This source displays appreciable long-term variability. Figure 5b shows the flux-density variations at 7.7 GHz from 1980 to 1999. The maximum 7.7-GHz flux-density variation has an amplitude $S_{\max}/S_{\min} = 2 \pm 0.14$. Figure 4a presents spectra obtained in November 1997 (upper) and July 1999 (lower). Both spectra have a minimum and can be approximated by the parabolas $\log S = -0.057 - 0.570 \log \nu + 0.327 \log^2 \nu$ and $\log S = -0.165 - 0.455 \log \nu + 0.236 \log^2 \nu$. Note the appreciable variability at low frequencies.

Five weak emission lines can be identified in the optical spectrum (Fig. 1d): MgII 2798 Å, the OII] 3727 Å forbidden line, the two Balmer lines Hγ 4340 Å and Hβ 4861 Å, and the [OIII] 4959 Å line at a redshift of $z = 0.517 \pm 0.008$. The object is an emission-line radio galaxy.

4.6. 1522+0400

The radio spectrum is power-law from 0.97–11.1 GHz, $S = 985\nu^{-0.927}$ mJy (Fig. 4b), and the flux density is not variable.

A strong [OIII] 5007 Å line, weaker OII] 3727 Å, [OIII] 4363 Å, and [OIII] 4959 Å lines, and weak NeV 3426 Å, [NeIII] 3869 Å, and Hβ 4861 Å lines can be identified in the optical spectrum (Fig. 2a). With the exception of Hβ, all these lines are forbidden and visible in emission. The redshift derived from all the lines is $z = 0.534 \pm 0.001$, and we classified the object as an emission-line radio galaxy.

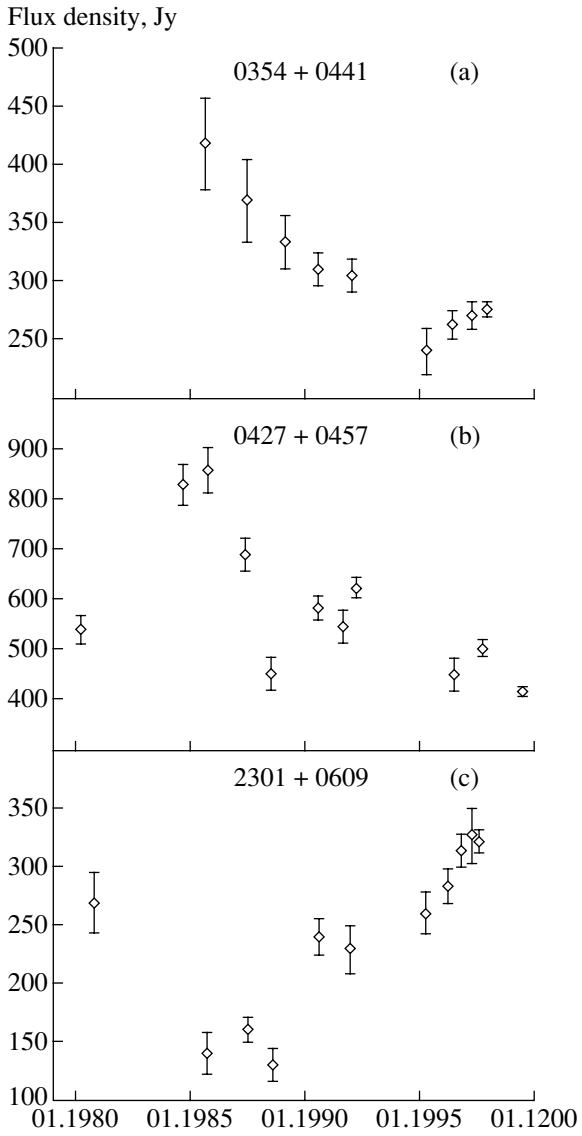

Fig. 5. 7.7-GHz light curves of 0427+0457 and 2301+0609. The flux densities before 1991 were obtained on the Southern sector and those after 1995 on the Northern sector of the RATAN-600 telescope.

4.7. 1600+0412

Observations made from 1989 through 1999 roughly once per year at 3.9 and 7.7 GHz did not reveal any flux-density variations within the errors. The ratio of the maximum and minimum flux densities measured at 7.7 GHz is $S_{\max}/S_{\min} = 1.1 \pm 0.15$. The spectrum (Fig. 4c) has a minimum near 6 GHz and can be approximated by the parabola $\log S = -0.553 - 0.617 \log \nu + 0.384 \log^2 \nu$ at epoch January 1998.

One broad line is clearly visible in the optical spectrum (Fig. 2b), which we have interpreted as a blend of Lyα 1216 Å and the nearby NV line at a redshift of $z = 3.11 \pm 0.01$. There are also weak CIV 1549 Å and HeII 1640 Å lines present near the noise level. We classified the object as a quasar.

4.8. 2301+0609

This source was observed at 3.9 and 7.5 GHz starting in 1980. Figure 5c presents the 7.7 GHz flux densities for 1980–1997. The flux density reached a minimum in 1987, after which it began to grow. The characteristic variability time scale (from maximum to minimum) is more than ten years, and the maximum flux-density variation at 7.7 GHz is $S_{\max}/S_{\min} = 2.7 \pm 0.5$. The spectrum (Fig. 4d) for August 1997 is well approximated by the logarithmic parabola $\log S = -0.733 + 0.695 \log \nu - 0.456 \log^2 \nu$, and has a maximum at 5.8 GHz, with the maximum flux density being 340 mJy.

Four emission lines can be identified in the optical spectrum (Fig. 2c): CIII] 1909 Å, MgII 2798 Å, and forbidden NeV 2973 Åand OII] 3727 Å. The redshift derived from these lines is $z = 1.089 \pm 0.003$, and the object was classified as a quasar.

5. CONCLUSIONS

Of the eight objects studied, five proved to be quasars (two with redshifts $z > 3$) and three to be emission-line radio galaxies. The radio galaxies 0323+0534 and 1522+0400 have constant flux densities and power-law spectra. The $z = 0.517$ emission-line radio galaxy 0427+0457 and $z = 1.089$ quasar 2301+0609 display appreciable radio variability. We did not detect any significant variability of the distant ($z = 3.11$) quasar 1600+0412 at 3.9 and 7.7 GHz over the ten years covered by our observations. As expected, long characteristic variability time scales are observed for all the objects with high redshifts. Nearly all the optical spectra show a rich selection of lines, enabling very accurate determinations of the corresponding redshifts.

6. ACKNOWLEDGMENTS

This work was supported by the Russian Foundation for Basic Research (project no. 01-02-16331), a Universities of Russia grant (project no. UR.02.03.005), and a grant of the State Science and Technology Program “Astronomy” (project no. 1.2.5.1).

REFERENCES

1. A. G. Gorshkov and V. K. Konnikova, Astron. Zh. **72**, 291 (1995) [Astron. Rep. **39**, 257 (1995)].
2. A. M. Botashov, A. G. Gorshkov, V. K. Konnikova, and M. G. Mingaliev, Astron. Zh. **76**, 723 (1999) [Astron. Rep. **43**, 631 (1999)].
3. A. G. Gorshkov, V. K. Konnikova, and M. G. Mingaliev, Astron. Zh. **77**, 407 (2000) [Astron. Rep. **44**, 353 (2000)].
4. V. Chavushyan, R. Mujica, A. G. Gorshkov, *et al.*, Pis'ma Astron. Zh. **26**, 403 (2000) [Astron. Lett. **26**, 339 (2000)].
5. V. Chavushyan, R. Mujica, A. G. Gorshkov, *et al.*, Astron. Zh. **78**, 99 (2001) [Astron. Rep. **45**, 79 (2001)].
6. V. Chavushyan, R. Mujica, R. Valdes, *et al.*, Astron. Zh. **79**, 771 (2002) [Astron. Rep. **46**, 697 (2002)].
7. A. B. Berlin, A. A. Maksyasheva, N. A. Nizhel'skiĭ, *et al.*, Abstracts of Papers, *XXVII Radio Astronomy Conference* (St. Petersburg, 1997), Vol. 3, p. 115 .
8. V. R. Amirkhanyan, A. G. Gorshkov, and V. K. Konnikova, Astron. Zh. **69**, 225 (1992) [Sov. Astron. **36**, 115 (1992)].
9. N. S. Soboleva, A. V. Temirova, and T. V. Pyatunina, Preprint SAO (Spets. Astrofiz. Obs., Nizhniĭ Arkhyz, 1986), p. 32.
10. A. G. Gorshkov and O. I. Khromov, Astrofiz. Issled. (Izv. Spets. Astrofiz. Obs.) **14**, 15 (1981).
11. A. G. Gorshkov and V. K. Konnikova, Astron. Zh. **73**, 351 (1996) [Astron. Rep. **40**, 314 (1996)].
12. I. W. A. Browne, Mon. Not. R. Astron. Soc. **293**, 257 (1998).
13. J. J. Condon, W. D. Cotton, E. W. Greisen, *et al.*, Astron. J. **115**, 1693 (1998).
14. D. Monet, A. Bird, B. Canzian, *et al.*, *USNO-SA 1.0* (U.S. Naval Observatory, Washington, 1996).
15. R. L. Pennington, R. M. Humphreys, S. C. Odewahn, *et al.*, Pub. Astron. Soc. Pac. **105**, 103 (1993).

Translated by D. Gabuzda

Astronomy Reports, Vol. 47, No. 6, 2003, pp. 467–479. Translated from Astronomicheskiĭ Zhurnal, Vol. 80, No. 6, 2003, pp. 508–521.

Physical Properties of Molecular Clouds as Functions of Their Galactocentric Distance from CS and $C^{34}S$ Observations

A. G. Kislyakov[1,2], I. I. Zinchenko[1,2], and L. E. B. Johansson[3]

[1] *Nizhni Novgorod State University, pr. Gagarina 23, Nizhni Novgorod, 603600 Russia*

[2] *Institute of Applied Physics, Russian Academy of Sciences, ul. Ul'yanova 46, Nizhni Novgorod, 603600 Russia*

[3] *Onsala Space Observatory, Chalmers University of Technology, S-43992 Onsala, Sweden*

Received June 20, 2002; in final form, January 10, 2003

Abstract—Twenty-eight CS molecular clouds toward HII regions with Galactocentric distances from ~4 to 20 kpc have been studied based on observations obtained in the $J = 2 \rightarrow 1$ lines of CS and $C^{34}S$ on the 20-meter radio telescope of the Onsala Space Observatory (Sweden) in March 2001. All 28 clouds have been mapped with an angular resolution of $\sim 40''$. The peak intensity in the $C^{34}S$ line has been measured for 20 objects. An LTE analysis has been performed and the parameters of the molecular cloud cores derived. The core sizes are $d_A = 0.3$–4.8 pc, with a median value of ~1.6 pc. The mean hydrogen densities in the cloud cores are $n_{H_2} = 3.5 \times 10^2$–$3.7 \times 10^4$ cm^{-3}, with a median value of $\sim 7.2 \times 10^3$ cm^{-3}. The value of n_{H_2} tends to decrease with increasing Galactocentric distance of the cloud. The masses of most clouds are 10^2–6×10^3 $M_\odot$, with the most probable value being $M_{CS} \sim 10^3$ $M_\odot$. The data follow the dependence $M_{CS} \propto d_A^{(2.4-3.2)}$. As a rule, the cloud masses are lower than the virial masses for $M_{CS} < 10^3 M_\odot$. © *2003 MAIK "Nauka/Interperiodica".*

1. INTRODUCTION

The distributions of diffuse and stellar material in the Galactic disk must be known if we wish to uncover their intrinsic connection. Though star formation is considered to be a result of the gravitational contraction of matter in gas–dust complexes, the distributions of the stellar and diffuse components are sometimes very different. For instance, the latitude scale of the stellar component of the Galactic disk can considerably exceed the thickness of the disk's molecular layer [1]. On the other hand, star-forming regions in the Galaxy are traced by HII regions, which are often also associated with molecular clouds. In this connection, observations of molecular clouds become a good test for the physical conditions in star-forming regions. A number of papers have analyzed the dependences of the physical parameters of molecular clouds on their Galactocentric distances (which we will call their Galactic radii R), which could shed light on various stages of star formation (see, e.g., [2–7]). The data presented in these studies, based on CO observations, were supplemented with the results of studies of clouds in the outer Galaxy (112 objects) and analyzed by Brand and Wouterloot [8] (a total of 204 objects at $R = 3$–21 kpc). This is probably the most comprehensive study of CO-cloud parameters (temperature T_R^*, equivalent radius R_A, mass $M_{W_{CO}}$, and line width Δv) as functions of R. However, interpretation of the CO data is hindered by the large line optical depths and blending, which is especially important for objects in the inner Galaxy (at $R < R_\odot$). One consequence of blending and saturation can be the empirical relationship $M_{W_{CO}} \propto R_A^2$. We expect a cubic dependence for the case of homogeneous, spherical cloud cores. There is also the problem of isolating the cloud cores against the extended CO background emission, as well as possible uncertainties in deriving Δv due to the presence of several clouds with similar velocities lying in the line of sight. Finally, the $M_{W_{CO}}(R)$ dependence can be distorted by variations of the parameter X along the Galactic radius, since the hydrogen column density is $N(H_2) = X \times W_{CO}$ $(= \int T_R^* dv)$. Observations of lines of different CO isotopes subject to an LTE analysis demonstrate that, for objects in the inner Galaxy, the value $X = 2.3 \times 10^{20}$ cm^{-2} (K km/s)$^{-1}$, derived taking into account the Galactic gradient of the $H_2/^{13}CO$ ratio [8], can be used. As shown in [8], using this value of X for objects in the outer Galaxy shifts the resulting estimates of the cloud masses at $R > R_\odot$. These circumstances compel us to seek other methods for determining the physical parameters of molecular clouds as functions of R. Kislyakov and Turner [9] presented observations of a relatively small number of CO clouds in the $J = 1 \rightarrow 0$ and $J = 2 \rightarrow 1$ lines of

1063-7729/03/4706-0467$24.00

the $C^{18}O$ isotope. That study, which made it possible to avoid the effects of line saturation and blending, showed that the cloud-core masses were described by the relation $M_{C^{18}O} \propto r_A^3$. There are also other discrepancies between this work and [8], which will be considered below. Zinchenko *et al.* [10] studied the physical parameters of 55 molecular-cloud cores in the $J = 2 \rightarrow 1$ lines of CS and $C^{34}S$. Their LTE analysis of the observational data yielded estimates of the R dependences of the mean hydrogen number density n_{H_2} and the cloud-core masses $M_{C^{34}S}$. Zinchenko *et al.* [10] obtained an unambiguous decrease in n_{H_2} with increasing R in the interval $5 \leq R \leq 14$ kpc, whereas the data of [9] do not demonstrate this effect. To elucidate the origins of these discrepancies and to expand the interval of R covered by the observations [9, 10], we carried out a new cycle of CS and $C^{34}S$ observations.

2. SELECTION OF OBJECTS AND RESULTS OF THE OBSERVATIONS

We selected objects for the study with the aim to cover the fairly broad interval $R \sim 4$–20 kpc. Furthermore, we gave preference to molecular clouds in the directions of compact HII regions (with optical radii $\leq 5'$) that have relatively simple kinematic structures (i.e., single, fairly symmetric CO lines). This yielded a sample of about 50 objects, many of which could not be observed due to limitations on the observing time. Table 1 lists the observed HII regions, and includes the majority of objects studied in [9]. We took the positions and optical sizes [D(opt) in Table 1] from [11, 12]. The distances to the objects (heliocentric r and Galactocentric R) were adopted in accordance with [13–15] [labeled (hunt), (wb), and (ave), respectively in Table 1]. We adopted the effective temperatures of the clouds in the $J = 1 \rightarrow 0$ CO line and their radial velocities (T_{CO} and V_{CO} in Table 1) from [11, 12]. The diameters of the molecular condensations D(CO) were measured in [9] using $C^{18}O$ observations. The asterisks in Table 1 denote objects observed in the $J = 2 \rightarrow 1$ CS line [16], in which case the velocities V_{CO} in Table 1 are those for this CS line. We observed the molecular clouds associated with Galactic HII regions in March 2001 on the 20-m radio telescope of the Onsala Space Observatory (Sweden), using a radiometer with a SIS receiver at the front end and a 1600-channel correlation spectrum analyzer. The frequency resolution of the analyzer is 25 kHz, which corresponds to a radial-velocity resolution of 0.076–0.078 km/s for the $C^{34}S$ and CS lines. The system noise temperature was 150–700 K, depending on the elevation and atmospheric conditions. When observing the $J = 2 \rightarrow 1$ CS line (resonant frequency 97 981 MHz), we used a frequency-switching regime. The weaker lines of the $C^{34}S$ isotope (resonant frequency 96 913 MHz) were observed using an on–on regime to achieve better baseline stability. The telescope pointing accuracy was periodically checked using observations of maser (SiO) sources, and errors were $\leq 5''$. Figure 1 presents selected spectra of some objects to illustrate the quality of the data. An integration time of 120–240 s was sufficient to measure the CS spectra. The isotope line spectra were obtained using longer integration times, from 600 s (S 187) to 3120 s (S 266).

We mapped the CS-line intensity for all the objects listed in Table 1. The telescope beamwidth is about $40''$, and we used a grid with this step for the mapping. Exceptions are S 90, which was mapped with a step of $20''$, and the two $CS^{34}S$ maps for S 106 and S 247. The maps of some objects are shown in Fig. 2. The preliminary data reduction was done online during the observations using the Xspec software developed at the Onsala Space Observatory (P. Bergman). The results of the observations are summarized in Table 2. Figure 3 combines the data for the emission temperatures T_{mb} in the CS and $C^{34}S$ lines. These temperatures together with the line widths and central radial velocities were determined via Gaussian approximation of the line profiles. When deriving T_{mb} from the antenna temperatures, we introduced a correction for the antenna efficiency. Table 2 lists the observed maximum T_{mb} values for the CS line for each object; the coordinates of this point correspond to the offsets in α and δ given in the second and third columns of Table 2 (offsets relative to the positions in Table 1). The temperature $T_{mb}(C^{34}S)$ was measured primarily at the CS-line peaks. If the source had two pronounced CS peaks, the isotope line was observed at both of them. In addition, we obtained two maps in the isotope line for S 106 and S 247 (discussion of these data is beyond the scope of this paper). The temperatures $T_{mb}(CS)$ and $T_{mb}(C^{34}S)$ in Fig. 3 display a fairly clear correlation. The Pearson correlation coefficient ρ_p is 0.83. The line in Fig. 3 was calculated via a regression analysis and corresponds to the equation

$$\log T_{mb}(C^{34}S) = -1.06(\pm 0.056) + 1.15(\pm 0.08) \times \log T_{mb}(CS). \quad (1)$$

Equation (1) yields $T_{mb}(CS)/T_{mb}(C^{34}S) \approx 11.5$. The simple average of this ratio is $\approx 12.6 \pm 1.6$. Points in Fig. 3 without error bars are those for which we could not measure $T_{mb}(C^{34}S)$, and the y values of these points were estimated using the average $T_{mb}(CS)/T_{mb}(C^{34}S)$ (these points are marked with asterisks in Table 2). Figure 4 shows the $T_{mb}(CS)(r)$ dependence for the data of Table 2. This plot shows

Table 1. Observed objects

No.	Name	α (1950.0)	δ (1950.0)	T_{CO}, K	V_{CO}, km/s	D(opt), arcmin	D(CO), arcmin	r, kpc	R, kpc	Reference
1	S 175	00:24:29.8	64:26:41	13	−49.8	2	1.6	1.7	9.5	hunt
2	S 201	02:58:59.4	60:14:46	18	−40.0	5	3.5	3.96	11.76	wb
3	BFS 31	03:21:08.8	54:49:01	17	−31.7	2	2.1	3.4	11.43	wb
4	BFS 32	03:47:54.4	51:21:00	17	−7.9	1.5	1.8	0.61	9.03	wb
5	S 209	04:07:18.0:	51:02:00	6	−52.2	14	–	9.85	17.78	wb
6	S 208	04:15:35.0	52:52:16	13	−30.3	1	2.5	4.0	12.16	wb
7	S 217	04:54:49.4	47:53:59	25	−18.3	9	1.5	4.2	11.7	wb, ave
8	S 235	05:37:42.0	35:49:00	32	−18.8	10	–	1.6	11.59	wb, ave
9	S 270	06:07:24.0	12:49:00	16	25.6	1	2.0	5.96	14.3	wb
10	S 266	06:16:00.0	15:18:00	10	32.2	1	–	9.42	17.76	wb
11	S 273	06:38:00.0	09:57:00	20	7.0	250	–	0.87	9.31	wb
12	S 286	06:52:03.8	−04:27:57	5	49.8	6	–	6.29	14.03	wb
13	BFS 58	06:58:34.4	−03:47:00	7	50.1	3	2.4	5.98	13.74	bw
14	S 302	07:29:24.0	−16:32:00	19	16.6	21	–	2.3	11.47	wb, ave
15	S 56	18:28:06.8	−10:00:00	10	69.9	7	3.4	5.57	3.91	ave
16	S 61	18:30:43.2	−04:59:35	15	44.0	2	4.0	2.5	6.4	hunt
17	S 65	18:44:06.1	−03:51:23	15	57.0	7	3.6	3.6	5.63	ave
18	S 82	19:28:01.6	18:13:11	20	24.9	9	–	1.5	7.7	ave
19	S 90	19:47:06.1	26:41:34	21	21.0	6	–	3.0	7.6	hunt
20	BFS 2	20:02:49.2	29:04:32	20	11.6	5	2.4	1.22	8.10	ave
21	S 106	20:25:33.8	37:12:52	25	−1.0	3	2.7	0.6	8.38	ave
22	BFS 11	21:41:41.3	65:51:50	21	−10.4	10	–	1.38	8.96	wb
23	S 135*	22:13:24.0	58:34:00	–	−18.3	15	–	1.4	9.3	wb, ave
24	S 158*	23:13:18.0	60:50:00	–	−56.3	10	–	3.6	11.96	wb, ave
25	S 187*	01:20:12.0	61:33:00	–	−13.9	10	–	1.08	10.65	wb
26	S 247*	06:05:48.0	21:38:00	–	3.1	9	–	2.9	11.4	hunt
27	S 295*	07:07:42.0	−10:26:00	–	13.7	8	–	0.7	10.85	wb, ave
28	WB 789	06:14:30.0	14:55:00	8.9	34.0	–	–	11.88	20.19	wb

two characteristic regions where $T_{mb}(\mathrm{CS})$ can be considered constant, and an area where it decreases steeply with increasing r, approximately as r^{-2}. In the next section, we show that the sizes of the cloud cores do not decrease with increasing r, leaving the possibility that the decrease in $T_{mb}(\mathrm{CS})$ is due to fragmentation of the clouds. The same conclusion was reached in [9] based on a similar analysis of $C^{18}O$ observations; the data from [9] are also presented in Fig. 4 (circles and lower lines). The upper lines in Fig. 4 intersect at $r \approx 3$ kpc; thus, the fragments' size can be estimated as ∼0.6 pc. This coincides with the scale size of a cloud fragment found in [9] from data for the $J = 1 \rightarrow 0$ $C^{18}O$ line.

3. PHYSICAL PARAMETERS OF MOLECULAR CLOUD CORES

Our analysis of the observational data in Table 2 yielded the following parameter estimates: effective

Table 2. Results of CS and $C^{34}S$ observations of HII regions

Name	Offsets		Int(CS), K km/s	Int($C^{34}S$), K km/s	T_{mbCS}, K	$T_{mb}C^{34}S$, K	ΔV, km/s
	α, arcsec	δ, arcsec					
BFS 2	0	0	2.34(0.13)	0.204(0.047)	1.61(0.033)	0.15(0.016)	1.48(0.035)
BFS 11	60	−160	6.03(0.14)	0.40(0.067)	2.56(0.070)	0.20(0.024)	2.22(0.07)
BFS 31	0	0	1.02(0.08)	0.076(0.030)	1.02(0.055)	0.10(0.015)	1.0(0.062)
BFS 32	0	−80	1.78(0.11)	0.054(0.065)	1.47(0.085)	0.05(0.06)	1.07(0.07)
BFS 58	−40	0	1.45(0.29)	0.1*	0.52(0.07)	0.043*	2.4(0.38)
S 56	40	−40	0.62(0.17)	0.057*	0.36(0.08)	0.03*	1.9(0.5)
S 61	−40	−40	6.04(0.36)	0.150(0.066)	3.03(0.13)	0.074(0.007)	1.84(0.09)
	120	−200	14.10(0.30)	1.60(0.10)	4.80(0.11)	0.49(0.03)	2.60(0.07)
S 65	0	−80	3.95(0.25)	0.37*	0.73(0.06)	0.06*	6.1(0.86)
S 82	−80	−80	2.54(0.06)	0.22(0.056)	2.47(0.09)	0.18(0.018)	1.85(0.08)
S 90	0	0	3.63(0.15)	0.74(0.08)	1.25(0.07)	0.08	2.60(0.16)
	60	60	7.52(0.16)	0.31(0.06)	2.65(0.07)	0.13(0.014)	2.60(0.08)
S 106	40	0	14.10(0.23)	1.43(0.07)	4.75(0.06)	0.46(0.07)	2.45(0.04)
	−100	0	10.40(0.15)	2.0(0.14)	5.18(0.07)	0.70(0.07)	1.89(0.03)
S 135a	0	0	9.12(0.05)	0.85(0.05)	2.84(0.09)	0.39(0.017)	3.0(0.11)
S 135b	0	0	10.30(0.23)	0.85(0.05)	3.12(0.08)	0.39(0.017)	3.1(0.09)
S 158	0	40	18.7(0.36)	1.18(0.05)	5.07(0.06)	0.40(0.012)	3.53(0.05)
S 175	−120	40	1.32(0.11)	0.11*	1.56(0.10)	0.13*	0.82(0.06)
S 187	80	40	14.9(0.22)	2.82(0.11)	7.47(0.108)	1.54(0.042)	1.81(0.03)
	0	40	12.9(0.23)	2.82(0.11)	6.90(0.11)	1.54(0.042)	1.82(0.03)
S 201	0	0	1.13(0.05)	$\leq$ 0.24	0.83(0.05)	$\leq$ 0.27	0.90(0.07)
	−40	0	0.75(0.05)	0.22(0.07)	0.51(0.04)	0.24(0.08)	1.36(0.13)
S 208	40	−80	3.30(0.13)	0.17(0.038)	1.75(0.048)	0.11(0.014)	1.76(0.056)
S 209	0	40	3.05(0.16)	0.46(0.05)	1.14(0.048)	0.19(0.015)	2.26(0.11)
S 217	−40	0	1.68(0.126)	$\leq$ 0.11	0.94(0.05)	$\leq$ 0.07	1.58(0.095)
S 235	40	−40	11.24(0.17)	0.51(0.08)	3.95(0.047)	0.25(0.02)	2.55(0.035)
S 247	80	60	30.50(0.30)	1.85(0.08)	8.40(0.09)	0.58(0.023)	3.38(0.04)
S 266	40	80	7.82(0.24)	0.48(0.056)	2.47(0.05)	0.27(0.007)	2.86(0.07)
S 270	0	40	3.30(0.16)	0.31(0.047)	1.57(0.05)	0.18(0.016)	1.68(0.057)
S 273	0	0	0.38(0.092)	0.018*	0.2(0.07)	0.017*	1.06(0.4)
S 286	40	−40	8.78(0.38)	0.45(0.096)	1.64(0.08)	0.075(0.015)	5.13(0.29)
S 295	40	−40	11.47(0.37)	1.73(0.072)	6.51(0.12)	0.79(0.157)	1.73(0.038)
S 302	0	0	1.3(0.5)	–	–	–	–
WB 789	40	40	2.43(0.20)	0.17*	0.81(0.04)	0.067*	2.6(0.15)

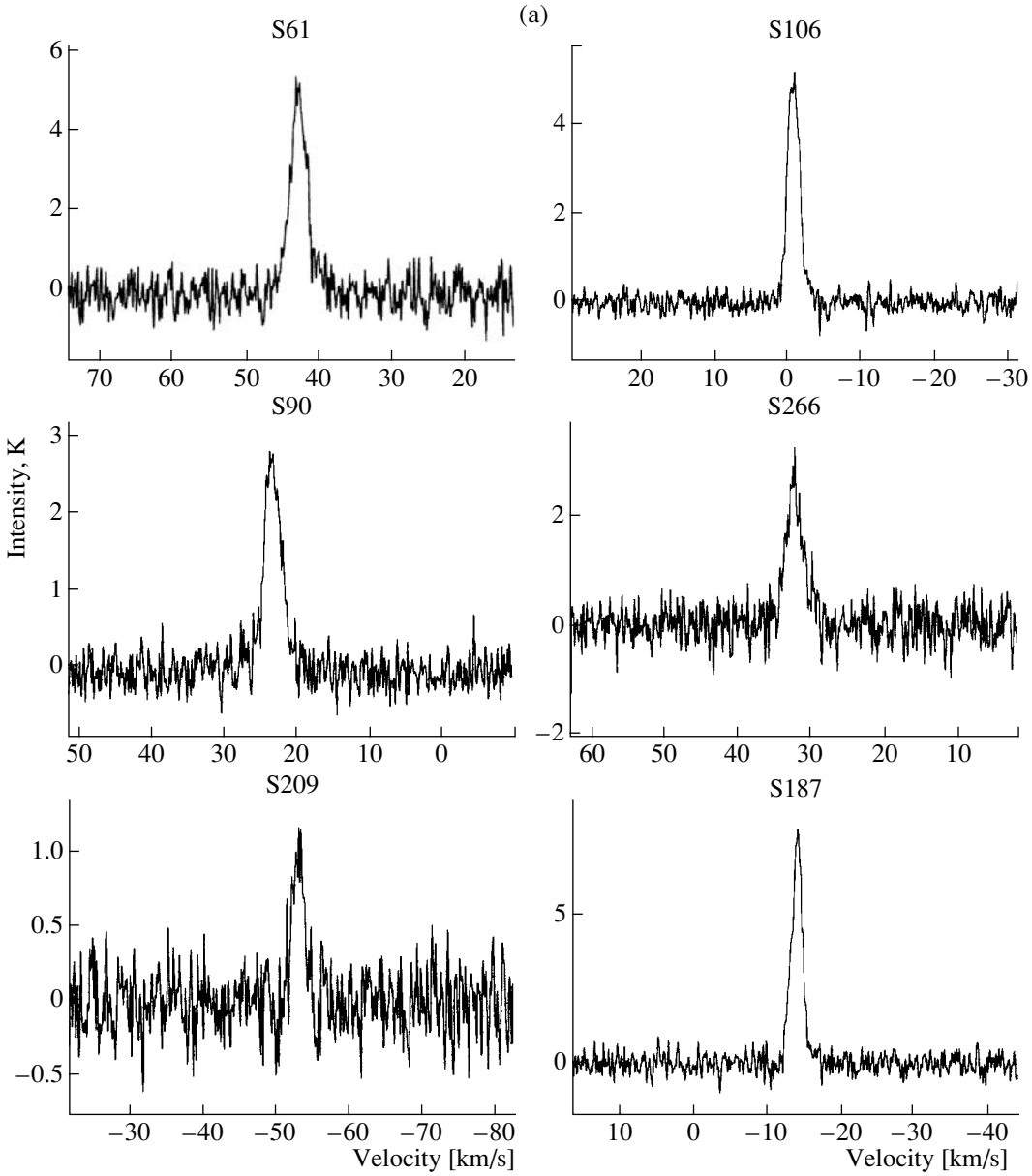

Fig. 1. Sample $J = 2 \rightarrow 1$ CS line spectra toward HII regions. The radial velocity range is ~62.4 km/s.

diameter of the core $d_A = 0.582\, r\sqrt{s_{ef}/\pi}$ pc (s_{ef} is the equivalent area of the object, computed from its CS map), mean hydrogen density in the core n_{H_2}, cloud mass M_{CS}, and virial mass $M_{VIR} = 105\, d_A\, \Delta v^2$. We corrected the derived cloud sizes for broadening by the telescope beam. The cloud-core sizes d_A are 0.3–4.8 pc, with the average value being $d_A = 1.6 \pm 0.2$ pc. The method used to derive the mean density of the molecular-cloud cores from the CS and $C^{34}S$ observations is described in detail in [17], and we will restrict our discussion here to explanations concerning a few points. It was shown in [17] that estimates of the $C^{34}S$ column density $N_{\ell 34}$ based on the LVG model with the cloud kinetic temperature derived from the temperature of its $J = 1 \rightarrow 0$ CO emission were similar to estimates of $N_{\ell 34}$ obtained in an LTE approximation for the transition excitation temperature $T_{ex} \approx 10$ K. In both cases, the inhomogeneity of the cloud must be taken into account. Here, we derived the $C^{34}S$ column density from LTE calculations, as was done in [10]. We took the [CS]/[$C^{34}S$] abundance ratio to be equal to the terrestrial value, 22.5, and determined the hydrogen abundance assuming that [CS]/[H_2]= 4×10^{-9}. The translation to the number density n_{H_2} was done assuming the core was spherically symmetrical. The derived physical parameters for the molecular-cloud cores are listed in Table 3. Figure 5 shows

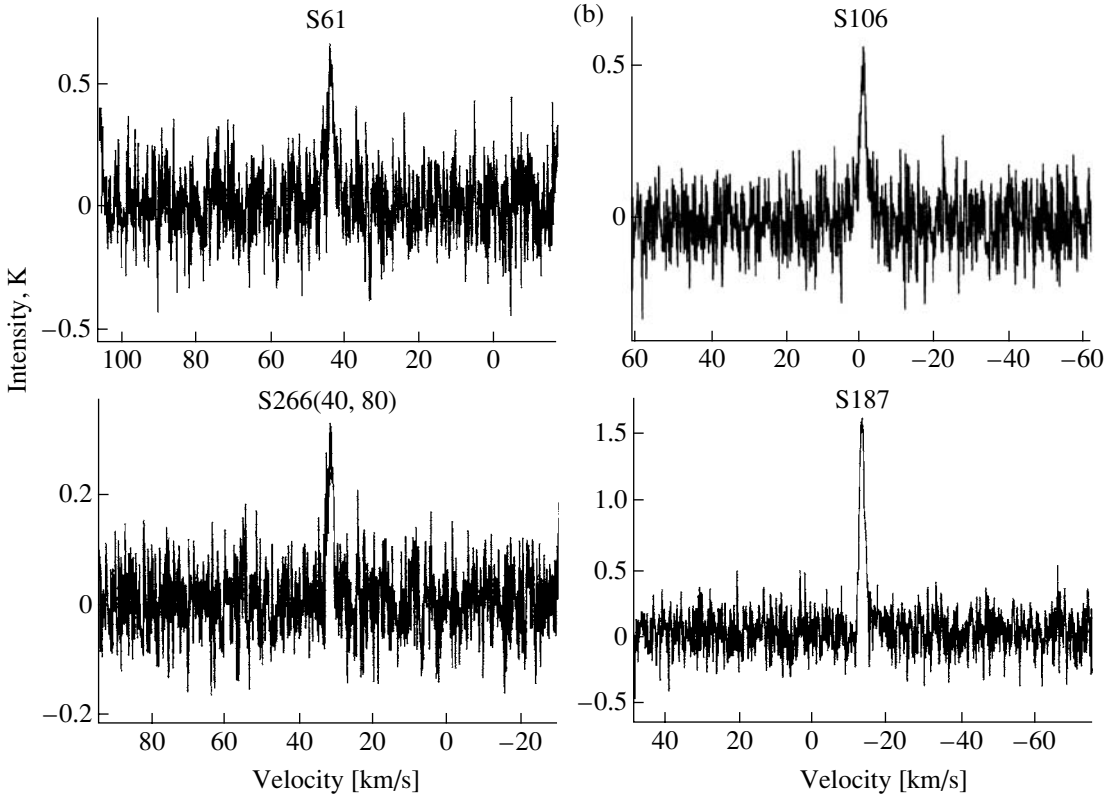

Fig. 1. (Contd.)

these parameters as functions of their heliocentric distances: $n_{H_2}(r)$, $M_{CS}(r)$, and $d_A(r)$. The first two plots do not display any clear tendency for systematic changes in n_{H_2} and M_{CS} with increasing r, while $d_A(r)$ shows a clear growth of the cloud diameter with increasing r; this is probably a selection effect. On the one hand, we have chosen compact HII regions; on the other hand, the minimum angular size of the objects is limited by the finite antenna beamwidth. In reality, the sizes of almost all the objects lie above the straight line $2 \times 10^{-4} r$ corresponding to the angular resolution of the radio telescope (Fig. 5). Thus, essentially all the objects considered were resolved by the antenna beam. The relationship between the cloud size and widths of the molecular lines describes the dynamics of the object. Figure 6 presents the relationship $\Delta v(d_A)$. The scatter of the data is fairly large, and a regression analysis does not yield a clear-cut result. The correlation coefficients for the $\Delta v(d_A)$ dependences are low: $\rho_p = 0.24$ and $\rho_p = 0.45$ for CS (crosses) and $C^{18}O$ (open circles in Fig. 6 according to [9]), respectively. It is obvious that the $C^{18}O$ lines are appreciably narrower than the CS lines and lie close to the line $\Delta v = d_A^{0.25}$ (thin line in Fig. 6), which closely matches a Kolmogorov subsonic turbulence law. It is possible that the CS lines are broadened by saturation, since, as a rule, the corresponding $C^{34}S$ lines are somewhat narrower. For comparison, Fig. 6 shows the line $\Delta v = 2\sqrt{d_A}$ (bold line), a relation that has been observed in multiple studies (see, e.g., [1, 8]). The mean hydrogen volume densities in the cloud cores are $3.5 \times 10^2 - 3.7 \times 10^4$ cm $^{-3}$, with the average value being $(7.2 \pm 1.8) \times 10^3$ cm^{-3}. There is a tendency for n_{H_2} to decrease with increasing core size. This tendency is traced most clearly in the densest objects, for which n_{H_2} has been measured relatively accurately (Fig. 7). The H_2 volume density in these objects follows the relationship $n_{H_2} \simeq 1.5 \times 10^4 d_A^{-1}$ (thin line in Fig. 7). The cloud masses are $1-6 \times 10^3\ M_\odot$ (Table 3). The most probable value of M_{CS}, found by averaging after eliminating extreme values, is $\sim(1 \pm 0.3) \times 10^3\ M_\odot$. The cloud mass–diameter dependence is clearly visible in Fig. 8; the correlation coefficient ρ_p is 0.8 for the CS data and increases slightly to $\rho_p = 0.83$ when the masses $M_{C^{18}O}$ from [9] are included (open circles in Fig. 8). The regression analysis applied (a combination of several regression methods) also yields somewhat different equations:

$$\log M_{CS} = 2.24(\pm 0.10) + 2.68(\pm 0.29) \times \log d_A, \quad (2)$$

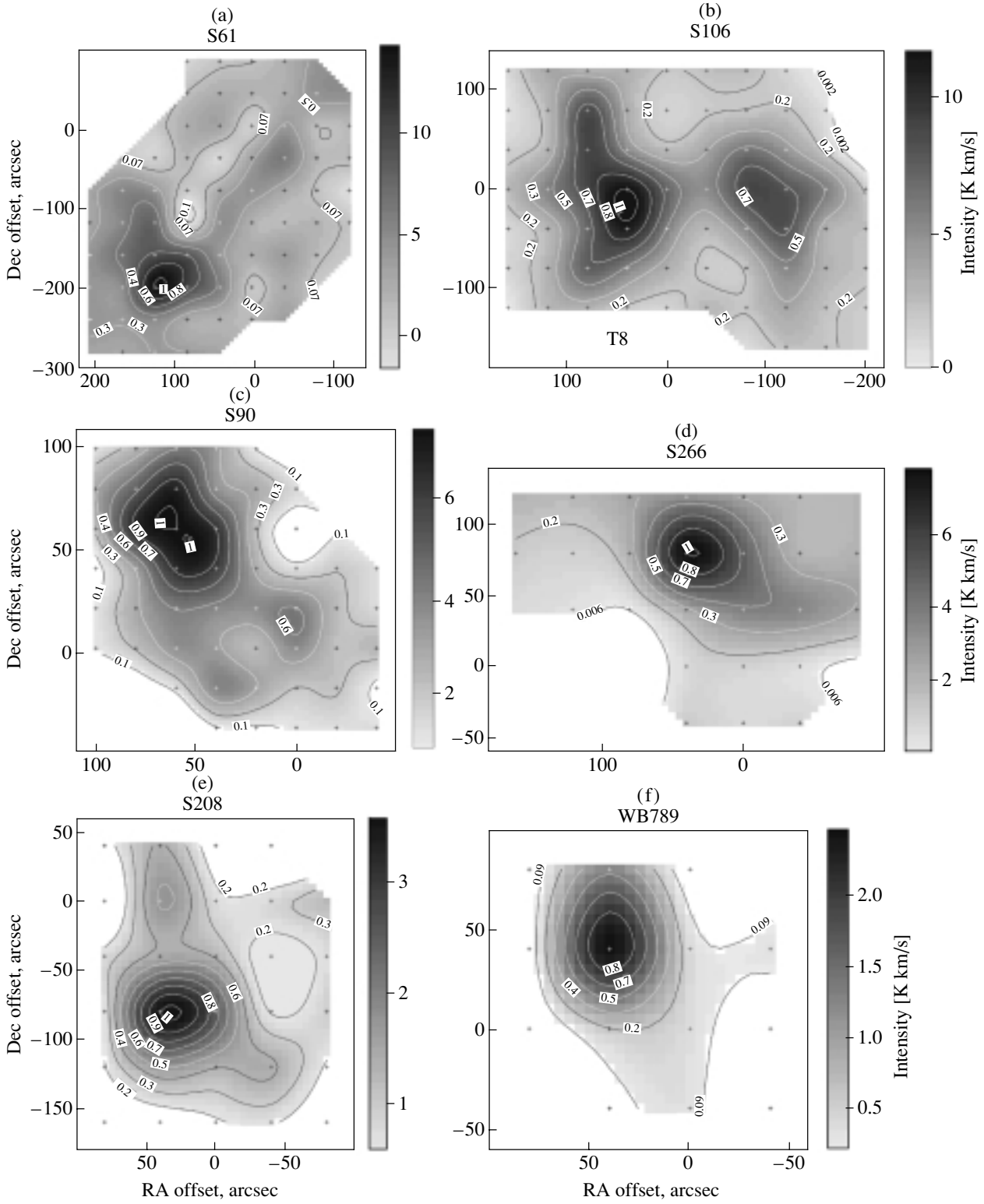

Fig. 2. CS $J = 2 \rightarrow 1$ line maps for some of the observed objects.

$\log M_{\mathrm{CS}}, \mathrm{C}^{18}\mathrm{O} = 2.1(\pm 0.11) + 3.0(\pm 0.25) \times \log d_{\mathrm{A}}$.

Thus, the mass–size dependence for molecular cloud cores is close to a cubic function. As noted above, we also obtained a cubic relationship in [9], $M_{\mathrm{C}^{18}\mathrm{O}}(d_{\mathrm{A}})$. This implies that a model in which the clouds are, on average, uniform but fragmented is adequate to

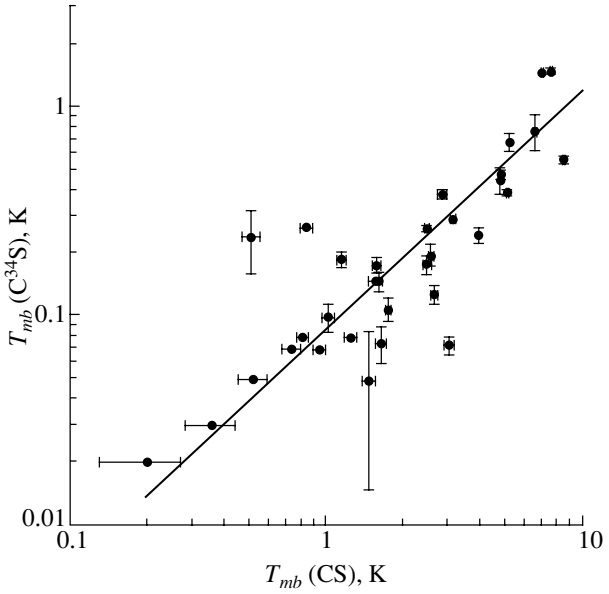

Fig. 3. Temperatures of the CS and $C^{34}S$ emission of HII regions.

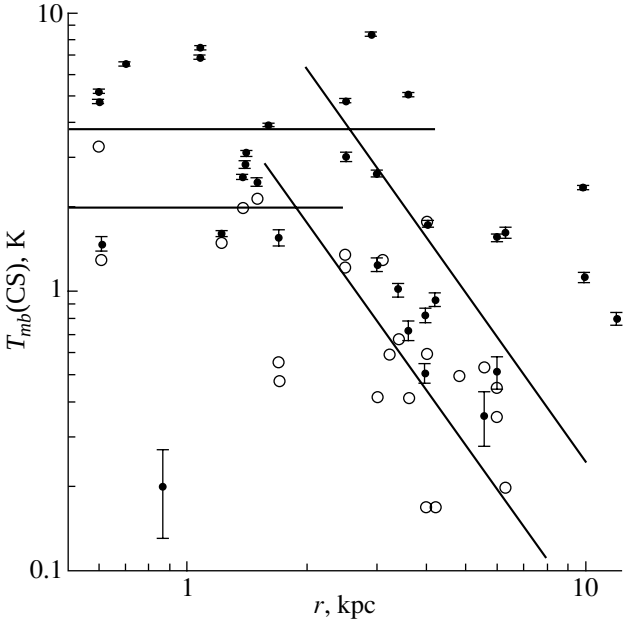

Fig. 4. Temperatures of the CS (crosses) and $C^{18}O$ (circles) emission of HII regions.

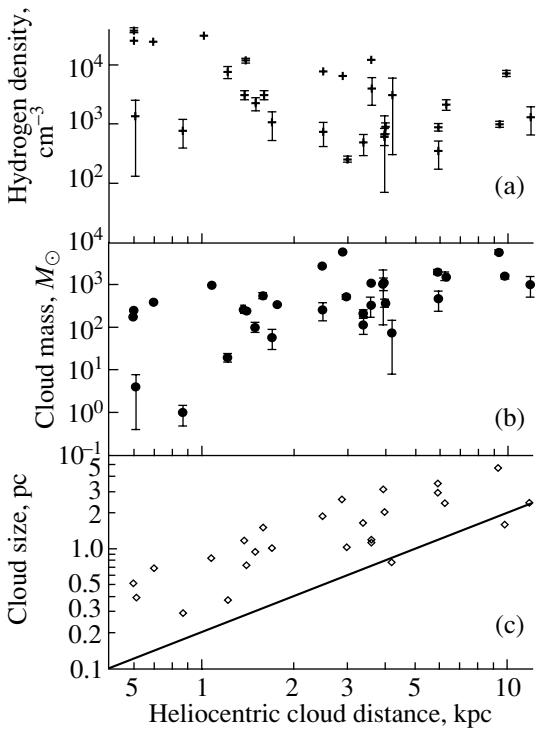

Fig. 5. (a) Hydrogen number density, (b) masses, and (c) sizes of CS molecular cloud cores.

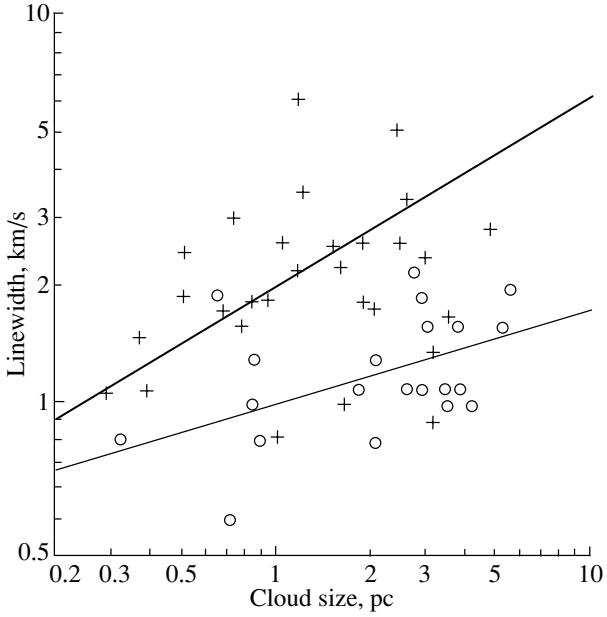

Fig. 6. CS (crosses) and $C^{18}O$ (circles) line widths as a function of the sizes of cloud cores.

describe the observations. The regression line corresponding to the latter equation of (2) is drawn in Fig. 8. It is clear that the scatter of points about this line considerably exceeds the accuracy of the estimated masses and probably reflects differences in the structure of the clouds. It is of interest to compare the cloud-core masses with their virial masses, as in Fig. 9, which plots M_{CS} as a function of M_{VIR} (also listed in Table 3). We can see that, for $M_{VIR} \leq 10^2 M_\odot$, the M_{CS} values lie much lower than the line $M_{CS} = M_{VIR}$. At sufficiently large core masses, the derived masses reach, and in many objects even exceed, the virial masses. Similar effects have been noted in other papers (see, e.g., [8, 9]).

Table 3. Physical parameters of the molecular clouds

Object ($\Delta\alpha$, $\Delta\delta$)	r, kpc	R, kpc	d_A, pc	n_{H_2}, cm^{-3}	M_{CS}, $M_\odot$	M_{VIR}, $M_\odot$
BFS 2 (0, 0)	1.22	8.1	0.37	7800 (1800)	20 (5)	80
BFS 11 (60, −160)	1.38	8.96	1.17	3200 (550)	270 (50)	600
BFS 31 (0, 0)	3.4	11.43	1.66	490 (190)	120 (45)	175
BFS 32 (0, −80)	0.61	9.03	0.39	1350 (1100)	4 (3)	50
BFS 58 (−40, 0)	5.98	13.74	2.97	360* (180)	500* (240)	1800
S 61 (−40, −40)	2.5	6.4	1.88	760 (300)	270 (300)	670
S 61 (120, −200)	2.5	6.4	–	8100 (490)	2800 (170)	1300
S 65 (0, -80)	3.6	5.63	1.16	4300* (2100)	350* (170)	4500
S 82 (−80, −80)	1.5	7.7	0.95	2300 (570)	100 (25)	340
S 90 (0, 0)	3.0	7.6	1.05	8900 (900)	500 (60)	740
S 90 (60, 60)	3.0	7.6	–	3700 (410)	220 (40)	740
S 106 (40, 0)	0.6	8.38	0.51	26000 (1300)	180 (10)	320
S 106 (−100, 0)	0.6	8.38	–	37000 (2600)	250 (20)	190
S 135 (0, 0)	1.4	9.3	0.73	12300 (740)	247 (15)	690
S 158 (0, 40)	3.6	11.96	1.21	13000 (500)	1200 (50)	1600
S 175 (−120, 40)	1.7	9.5	1.02	1100* (550)	60* (30)	70
S 187 (80, 40)	1.08	10.65	0.84	32000 (1300)	1000 (40)	300
S 201 (0, 0)	3.96	11.76	3.17	$\leq$720	$\leq$1200	270
S 201 (−40, 0)	3.96	11.76	–	660 (200)	1100 (350)	620
S 208 (40, −80)	4.0	12.16	2.04	900 (200)	390 (85)	660
S 209 (0, 40)	9.85	17.78	1.62	7600 (800)	1700 (180)	870
S 217 (−40, 0)	4.2	11.7	0.78	$\leq$3000	$\leq$80	200
S 235 (40, −40)	1.6	11.6	1.51	3200 (500)	560 (90)	1000
S 247 (80, 60)	2.9	11.4	2.59	6800 (300)	6000 (240)	3100
S 266 (40, 80)	9.42	17.76	4.76	1100 (130)	6000 (700)	4100
S 270 (0, 40)	5.96	14.3	3.53	900 (130)	2000 (300)	1000
S 273 (0, 0)	0.87	9.31	0.29	800* (400)	1* (0.5)	30
S 286 (40, −40)	6.29	14.03	2.41	2200 (470)	1600 (660)	6650
S 295 (40, −40)	0.7	10.85	0.68	24000 (1000)	380 (15)	200
WB 789 (40, 40)	11.88	20.2	2.47	1350* (870)	1100* (530)	1750

4. CLOUD-CORE PARAMETERS AS A FUNCTION OF GALACTIC RADIUS

Let us first consider the $d_A(R)$ dependence, shown in Fig. 10. This plot also demonstrates the selection effect discussed above (Fig. 5c). We can see that the minimum core sizes are observed for $R \approx R_\odot$ (the position of the Sun is shown by the vertical line). An increase of d_A is observed to the right and to the left of this line due to the limited possible minimum size of the object due to the effect of dilution. Of course, these properties of the $d_A(R)$ distribution can distort the observed dependences of the physical parameters of the cores on Galactic radius to some extent. In this connection, we will be concerned primarily with

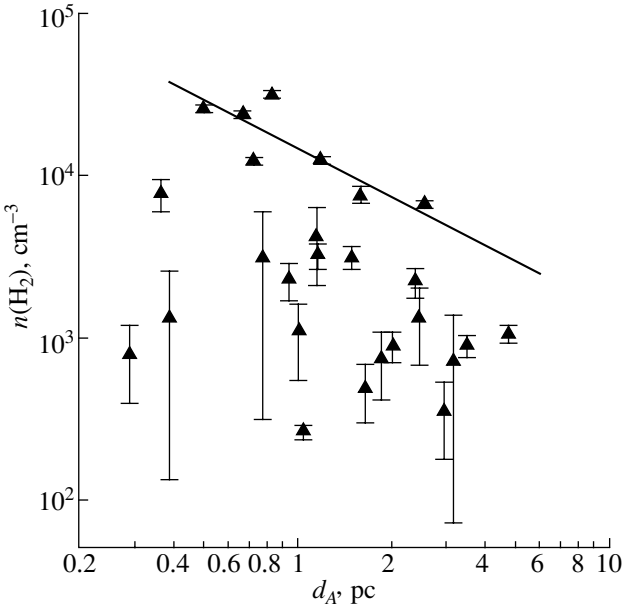

Fig. 7. Densities of molecular cloud cores as a function of their sizes.

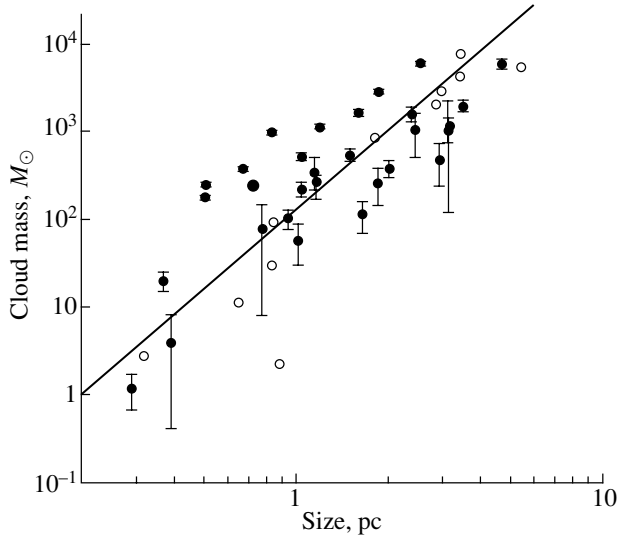

Fig. 8. Cloud-core masses derived from the CS (crosses) and $C^{18}O$ (circles) observations as functions of their sizes.

the large-scale characteristics of these relationships. Figure 11 presents two important parameters of the molecular-cloud cores (n_{H_2} and M_{CS}) as functions of Galactic radius. These same core parameters derived from the $C^{18}O$ observations of [9] are also plotted (open circles) and are in good agreement with the results of the present paper. Let us consider in more detail the $n_{H_2}(R)$ dependence. Due to the large scatter of the data, we cannot expect regression methods to be very efficient in this case. However, the calculated

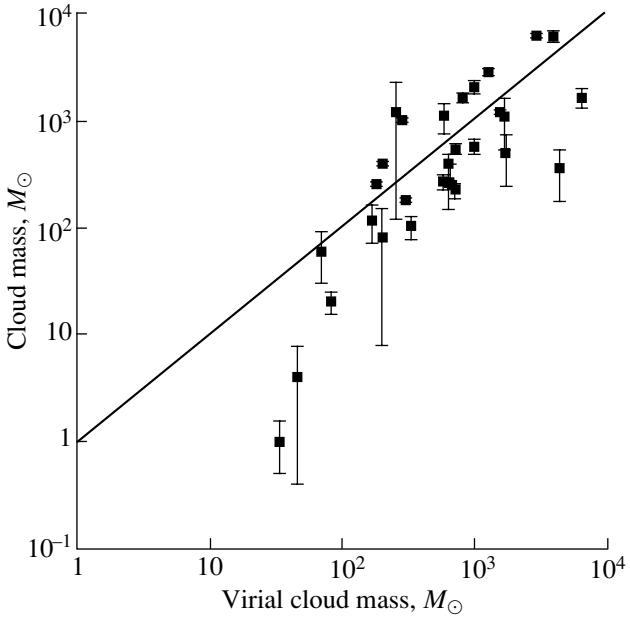

Fig. 9. Relationship between the CS cloud-core mass and its virial mass.

correlation coefficients indicate a definite tendency for the mean hydrogen density in the molecular cloud cores to decrease with increasing Galactic radius. Our analysis of the CS line observations yields $\rho_p \simeq -0.28$. The results obtained for the most frequently used regression analysis, based on minimizing the rms deviation of the points from the linear relationship, are

$$\log n_{H_2} = 4.73(\pm 0.63) - 1.2(\pm 0.6) \times \log R. \quad (3)$$
$$\log n_{H_2} = 4.0(\pm 0.27) - 0.047(\pm 0.023) \times R.$$

Due to the large scatter of the molecular-cloud parameters, the first regression line of (3) (bold line in Fig. 11) indicates only a tendency for the mean density of the cloud cores to decrease toward the periphery of the Galaxy. This effect could partly be a consequence of the above-mentioned decrease of n_{H_2} with increasing d_A. Zinchenko *et al.* [10] found the exponential relationship $\overline{n}_{H_2}(R) = n_0 \exp(-R/R_n)$, with a least-squares fit yielding the parameters $n_0 = (3.7 \pm 0.5) \times 10^5$ cm^{-3} and $R_N = (2.7 \pm 0.6)$ kpc. For comparison with this result, we obtained the second regression equation in (3) by analyzing the $\log n_{H_2}(R)$ dependence using the data considered here (in this case, the correlation coefficient ρ_P is also $\simeq -0.28$). The second equation in (3) presents the exponential dependence $\overline{n}_{H_2}(R) = n_{01} \exp(-R/R_{n1})$, with $n_{01} = 1.26\left(^{+0.66}_{-0.72}\right) \times 10^4$ cm^{-3} and $R_{n1} = 9.2\left(^{+9}_{-3}\right)$ kpc. The curve corresponding to this equation is also shown

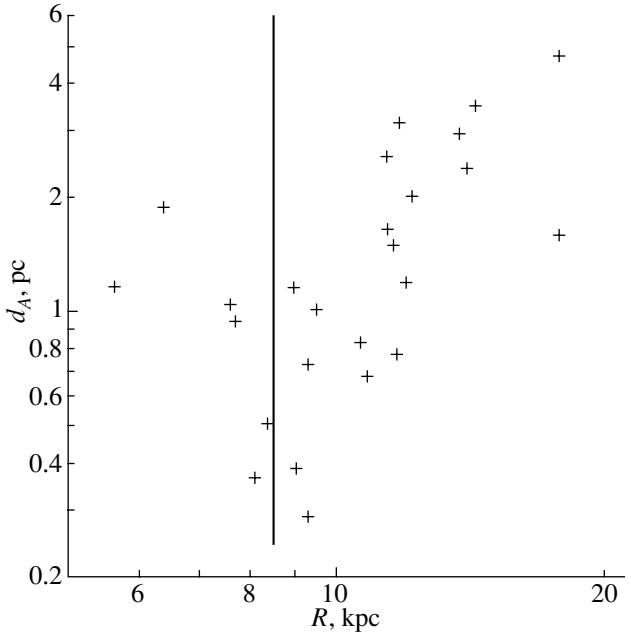

Fig. 10. CS cloud-core sizes as a function of Galactocentric radius.

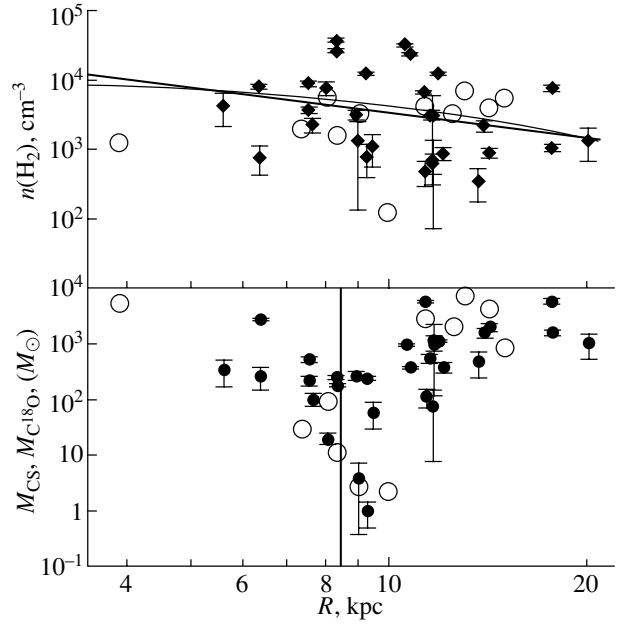

Fig. 11. Densities and masses of CS (dots) and $C^{18}O$ (circles) clouds as functions of Galactocentric distance.

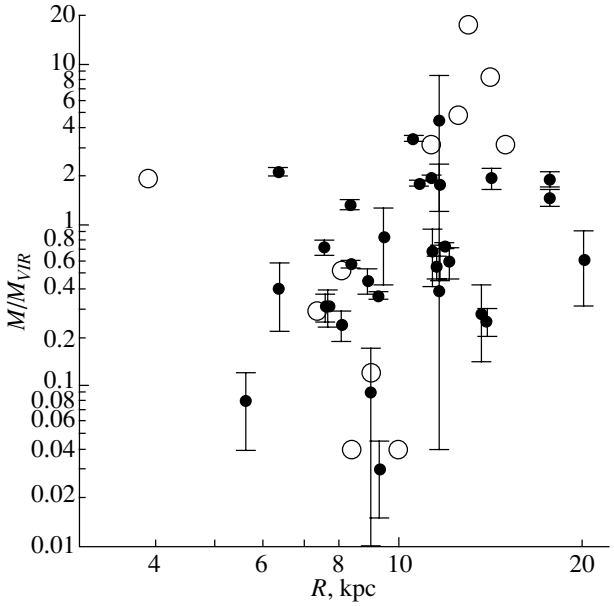

Fig. 12. Ratios of CS (dots) and $C^{18}O$ (circles) core masses to their virial masses.

in Fig. 11 (thin curve) and nearly coincides with the line drawn for the first equation in (3). Thus, Eqs. (3) indicate a weaker $\log n_{H_2}(R)$ dependence than that found in [10] (note that a more representative population of clouds was analyzed in [10]). We can see that the regression analysis of the $n_{H_2}(R)$ dependence using the data considered here yields excessively large errors. In this connection, let us compare the mean values of n_{H_2} for the inner ($R < R_\odot$) and outer ($R > R_\odot$) Galaxy. We obtain for the hydrogen number density $\overline{n}_{H_2}(I) = (1.08 \pm 0.48) \times 10^4$ cm^{-3} for $R < R_\odot$ and $\overline{n}_{H_2}(O) = (5.5 \pm 1.8) \times 10^3$ cm^{-3} for $R > R_\odot$, which also indicates a tendency for decreasing hydrogen number density in the molecular-cloud cores with increasing Galactic radius. However, the uncertainties in the obtained $\overline{n}_{H_2}$ values are so large that a constant hydrogen density also gives an acceptable fit. The result becomes more certain if we take into account the $C^{18}O$ data. In this case, we obtain $\overline{n}_{H_2}(I) = (8.5 \pm 3) \times 10^3$ cm^{-3} for $R < R_\odot$ and $\overline{n}_{H_2}(O) = (5.1 \pm 1.4) \times 10^3$ cm^{-3} for $R > R_\odot$. In a similar way, we can estimate the mean masses of the cloud cores for the inner and outer Galaxy. As a result, we obtain for the CS data $\overline{M}_{CS(I)} = 530 \pm 290\ M_\odot$ for $R < R_\odot$ and $\overline{M}_{CS(O)} = 1200 \pm 370\ M_\odot$ for $R > R_\odot$, indicating an increase of the core masses toward the periphery of the Galaxy. Including the $C^{18}O$ data makes the estimate more certain in this case as well: $\overline{M}_I = 790 \pm 440\ M_\odot$ for $R < R_\odot$ and $\overline{M}_O = 1550 \pm 390\ M_\odot$ for $R > R_\odot$. These estimates can be improved slightly by standard statistical "cleaning" (rejection of extreme values). However, we should also bear in mind the above-mentioned selection effects. A comparison of Figs. 10 and 11 demonstrates the influence of selection effects on the $M_{CS}(R)$ dependence. At the same time, it seems likely that the $n_{H_2}(R)$ dependence is less sub-

ject to distortion by selection effects. Finally, Fig. 12 presents $q = M_{\mathrm{CS,C^{18}O}}/M_{\mathrm{VIR}}$ as a function of Galactic radius. This plot displays a still larger scatter of the data, and regression analyses yield no correlations in this case. Let us resort to the method used above, i.e., estimating the average value of q for inner and outer regions of the Galaxy, adopting $R = 10$ kpc as a boundary between them. Based on the data of Table 3 and the results of [9], we obtain $\overline{q}_{\mathrm{I}} = 0.54 \pm 0.2$ for $R < 10$ kpc and $\overline{q}_{\mathrm{O}} = 2.1 \pm 0.5$ for $R > 10$ kpc. If we reject obvious underestimates $\overline{q} < 0.2$ at $R \approx R_\odot$, $\overline{q}_{\mathrm{I}}$ will increase to 0.74 ± 0.2, while $\overline{q}_{\mathrm{O}}$ will remain the same. Obviously, this result is a consequence of the fact that the masses of objects observed in the outer Galaxy exceed somewhat the masses of objects at $R < 10$ kpc; this probably reflects selection effects associated with observing distant objects (Fig. 5, 10), although the most massive cores were detected approximately at the boundary between the inner and outer Galaxy (Table 3). The ensemble average $\overline{q}_{\mathrm{T}}$ is 1.3 ± 0.3 (this is the error of the average, while the variance is about 1.5).

5. DISCUSSION

We have used our observations to derive information about the physical parameters of ~30 cores of CS molecular clouds and have traced the radial dependences of these parameters in the interval 4–20 kpc. Let us compare our results with those of other studies of molecular clouds. Analyses of the radial dependences of molecular-cloud parameters are hindered by a number of circumstances: selection effects, inaccuracies in the distances r and R, and uncertainties in the structures and general configurations of molecular clouds. It is especially difficult to interpret CO observations due to the effects of line saturation and blending. In our view, precisely these effects lead to the strong $M_{W_{\mathrm{CO}}}(R)$ dependence noted in [8]. For $3 < R < 5$ kpc, $M_{W_{\mathrm{CO}}} = 3 \times 10^4$–$5 \times 10^6\ M_\odot$, whereas $M_{W_{\mathrm{CO}}} = 5 \times 10^2$–$5 \times 10^4\ M_\odot$ in the interval $15 < R < 20$ kpc. In fact, the data of [8] refer to large molecular complexes, tens of parsecs in size. Owing to the high density of molecular clouds in the inner Galaxy, the effects of line saturation and blending are especially pronounced. This results in a loss of small clouds and problems with distinguishing cloud cores—a kind of selection effect. In the outer Galaxy, the density of the clouds is lower, making it possible to distinguish individual objects in molecular complexes and observe lower-mass clouds. The effects of line saturation and overlap are also reduced. Excitation of the $C^{18}O$ ($J = 2 \rightarrow 1$) lines (and especially the CS lines) requires a much higher hydrogen density than excitation of the CO $J = 1 \rightarrow 0$ line; therefore, the effects of line saturation and overlap are minor, and only the densest condensations in the clouds—their cores—are observed. As we have shown here and in other similar studies, the sizes of these cores are on the order of 1 pc, and their masses are in the range $\sim 3 \times 10^2$–$3 \times 10^4\ M_\odot$. Such cores are detectable in both the inner and outer Galaxy. The above-mentioned trend for increasing core masses with increasing R is probably due to another selection effect—the limited resolutions of radio telescopes. In [10], supplemented with the data of [18], it is shown that the masses of molecular-cloud cores are virtually independent of R in the interval $4 < R < 14$ kpc (note that these data are also not free of selection effects due to limited resolution). Wouterloot *et al.* [19], also based on CO data, found a steep Galactic gradient in the mean density of molecular clouds, which is probably also a consequence of the decrease in the cloud density in the outer Galaxy and reduction of the effects of line saturation and overlap. The $n_{\mathrm{H_2}}(R)$ dependence is probably less subject to selection effects. Our data demonstrate some tendency for a decrease in the average density of the CS molecular-cloud cores toward the periphery of the Galaxy, but it is not as strong as that for the data of [10], supplemented with the data of [18]. We took into account only the CS data when discussing the $n_{\mathrm{H_2}}(R)$ dependence, since $C^{18}O$ measurements [9] yield the maximum, not average, cloud density, which could have a different R dependence (as was already pointed out in [10]). Given the differences in the procedures used to select the corresponding samples, the mean parameters of CS cloud cores found in [10] and in the present work are in satisfactory agreement. There is a considerable discrepancy between the nearly cubic $M_{\mathrm{CS}}(d_{\mathrm{A}})$ dependence we have found and the $M_{W_{\mathrm{CO}}} \propto r_{\mathrm{A}}^2$ dependence of [8]. As noted above, the latter relationship could also be a consequence of line saturation and blending (see, e.g., [1]). Furthermore, errors in cloud distances can lead to the same result [8]. These possibilities were also put forward in [20], where the relationship $M_{\mathrm{CO}} \propto r_{\mathrm{A}}^3$ was obtained based on CO line observations (this paper was criticized in [8]). Finally, let us briefly consider further the M/M_{VIR} ratio as a function of R. This is also a difficult problem due to the considerable scatter in the observational data. Brand and Wouterloot [8], who also used the data of [2–7], showed that the data for the CO $J = 1 \rightarrow 0$ line provide evidence for a decrease in q toward the periphery of the Galaxy, from $\overline{q}_{\mathrm{I}} = 1.2$–$1.7$ at $R < R_\odot$ to $\overline{q}_{\mathrm{O}} = \sim 0.5$ at $R > R_\odot$. In this case, too, the standard deviations are close to the average values of q. This conclusion is opposite to that drawn above, that q increases toward the periphery of the Galaxy; this reflects the discrepancy between the estimated average cloud masses in the inner and outer Galaxy discussed

above. As already noted, these estimates are not free of selection effects. At the same time, we arrived at a qualitatively similar conclusion as that of [8], that q grows with increasing core mass (see Section 3). Though the value of q averaged over the entire sample of [8] (204 objects) is $0.7 \pm 0.65(1\sigma)$, in contrast to the result $\overline{q}_T = 1.3 \pm 0.3$ $(1\sigma/\sqrt{N-1})$ found above, given the large scatter in q, we cannot be sure that there is a discrepancy in the $q(R)$ dependences estimated from the CO and CS lines. However, it is appropriate to note that, owing to the unavoidable broadening of the optically thick CO lines and their overlap, considerable reassessments of the virial cloud masses may be required.

The derived molecular-cloud parameters are determined by the relative CS (more exactly, $C^{34}S$) abundance, which we assumed to be constant. At the same time, it is known that the relative (with respect to H_2) abundances of many elements (including sulfur and, possibly, carbon) vary with radius in the Galaxy (see, e.g., [21, 22]). However, this does not necessarily lead to changes in the relative number density of CS, whose abundance is determined by a rather complicated chain of reactions. There are no convincing data favoring the presence of gradients in the abundances of either CS or $C^{34}S$ in the Galaxy. Our data provide evidence against an appreciable gradient of this kind. This conclusion is based mainly on a comparison of the estimated masses of CS clouds with their virial masses. The virial mass is completely independent of the composition of the molecules. Therefore, the fact that $M(\mathrm{CS})/M_{\mathrm{vir}}$ is virtually independent of Galactocentric distance most likely testifies to a constant $C^{34}S$ abundance. Moreover, $M(\mathrm{CS})/M_{\mathrm{vir}}$ may even increase with increasing R; this could indicate an increase of the CS content, although the sulfur abundance decreases.

The results of our study demonstrate the effectiveness of the method applied to analyze the data for the molecular-cloud cores. At the same time, the value of obtaining similar CS observations with higher angular resolution is obvious; this will allow us to reduce the influence of selection effects on the radial dependences of the derived physical parameters of the molecular-cloud cores.

ACKNOWLEDGMENTS

The authors are grateful to the staff of the Onsala Space Observatory for help with the observations. This work was supported by NASA (the JURRISS program grant), INTAS (grant 99-1667), and the Russian Foundation for Basic Research (project no. 99-02-16556).

REFERENCES

1. F. Combes, Ann. Rev. Astron. Astrophys. **29**, 253 (1991).
2. T. M. Dame, B. G. Elmgreen, R. S. Cohen, and P. Thaddeus, Astrophys. J. **305**, 892 (1986).
3. P. M. Solomon, A. R. Rivolo, J. Barrett, and A. Yahil, Astrophys. J. **319**, 730 (1987).
4. K. N. Mead and M. L. Kutner, Astrophys. J. **330**, 399 (1988).
5. S. W. Digel, Ph. D. Thesis (Harvard University, 1991).
6. J. Sodroski, Astrophys. J. **366**, 95 (1991).
7. J. Brand and J. G. A. Wouterloot, Astron. Astrophys. **103**, 503 (1994).
8. J. Brand and J. G. A. Wouterloot, Astron. Astrophys. **303**, 851 (1995).
9. A. G. Kislyakov and B. E. Terner, Astron. Zh. **72**, 168 (1995) [Astron. Rep. **39**, 147 (1995)].
10. I. Zinchenko, L. Pirogov, and M. Toriseva, Astron. Astrophys., Suppl. Ser. **133**, 337 (1998).
11. L. Blitz, M. Fich, and A. Stark, Astrophys. J., Suppl. Ser. **49**, 183 (1982).
12. M. Fich and L. Blitz, Astrophys. J. **279**, 125 (1984).
13. D. A. Hunter, H. A. Thronson, and C. Wilton, Astron. J. **100**, 1915 (1990).
14. J. G. A. Wouterloot and J. Brand, Astron. Astrophys., Suppl. Ser. **80**, 149 (1989).
15. V. S. Avedisova and J. Palous, Bull. Astron. Inst. Czechosl. **40**, 42 (1989).
16. L. Bronfman, L. A. Nyman, and J. May, Astron. Astrophys., Suppl. Ser. **115**, 81 (1996).
17. I. Zinchenko, V. Forsström, A. Lapinov, and K. Mattila, Astron. Astrophys. **288**, 601 (1994).
18. M. Juvela, Astron. Astrophys., Suppl. Ser. **118**, 191 (1996).
19. J. G. A. Wouterloot, J. Brand, W. B. Burton, and K. Kwee, Astron. Astrophys. **230**, 21 (1990).
20. D. Leisawitz, Astrophys. J. **359**, 319 (1990).
21. J. I. Hou, N. Prantzos, and S. Boissier, Astron. Astrophys. **362**, 921 (2000).
22. S. M. Andrievsky, V. V. Kovtyukh, P. E. Luck, *et al.*, Astron. Astrophys. **381**, 32 (2002).

Translated by G. Rudnitskiĭ

Astronomy Reports, Vol. 47, No. 6, 2003, pp. 480–482. Translated from Astronomicheskiĭ Zhurnal, Vol. 80, No. 6, 2003, pp. 522–525.

A Model for the Dust Envelope of the Protoplanetary Nebula LSIV−12°111

M. B. Bogdanov

Chernyshevskiĭ State University, Saratov, Russia

Received October 17, 2002; in final form, November 27, 2002

Abstract—A model for the dust envelope of the protoplanetary nebula LSIV−12°111 is computed using measured fluxes of the object from the UV to the far-IR. It is assumed that the spherically symmetrical envelope is comprised of silicate particles with a standard MRN size distribution, whose number density varies inversely proportional to the square of the distance. The optical depth of the envelope, whose inner boundary is 5.6×10^{16} cm from the central star, is 0.072 at 0.55 μm. The temperature of the dust grains at the inner boundary of the envelope is 124 K. The estimated distance to LSIV−12°111 is 3.8 kpc. The current mass-loss rate of the object derived from a self-consistent solution for the radiative transport and motion of the dust in the envelope is $1.0 \times 10^{-5}\ M_\odot$/yr. © *2003 MAIK "Nauka/Interperiodica"*.

1. INTRODUCTION

The studies carried out in [1, 2] showed that the object LSIV−12°111 (=BD−13°5550 = IRAS 19590−1249) is associated with a star in the evolutionary stage following its stay on the asymptotic giant branch (a post-AGB star) and preceding the formation of a planetary nebula. Such objects have received the name "protoplanetary nebulae" [3]. The duration of this stage is so short that evolutionary variations in the effective temperature of the star could become appreciable in the lifetime of one generation of observers. Investigations of these objects can potentially elucidate the mechanism for the generation of the powerful stellar wind that leads to the ejection of the star's envelope, which is very important for studies of the final stages in the evolution of moderate-mass stars.

The analysis of the spectrum of LSIV−12°111 carried out in [1] demonstrated that the chemical composition of this object differs substantially from that for a main-sequence B star, testifying to its post-AGN nature. The spectral energy distribution (SED) obtained in [2] using IUE and IRAS data together with middle-IR photometric data shows an infrared excess associated with a cool dust envelope, which was presumably ejected by the star when it left the asymptotic giant branch. The IRAS Low Resolution Spectrometer data (7–24 μm) for LSIV−12°111 have large errors. However, a spectrum obtained by averaging three scans shows a characteristic peak near 10 μm [2], testifying to the presence of silicates in the dust of the stellar envelope. The presence of a silicate feature in the IR spectrum of LSIV−12°111 was confirmed by later ISO observations, although the uncertainties in the fluxes for this object registered by the spectrometer of this space observatory are also rather large.

Arkhipova *et al.* [4] recently studied the variability of LSIV−12°111 using UBV photometry. As for other protoplanetary nebulae, the amplitude of the rapid, chaotic brightness variability, which is probably due to fluctuations of the stellar wind, proved to be small, about $0^m.3$ in all three filters.

The aim of our current study is to compute a model for the dust envelope of LSIV−12°111 and estimate the object's mass-loss rate.

2. OBSERVATIONAL DATA

We selected the mean UBV magnitudes obtained by Arkhipova *et al.* [4] for comparison with the SED of the model envelope, as well as the $JHKLM$ photometry of [2] and the 12, 25, 60, and 100 μm IRAS fluxes. As is noted above, the IRAS and ISO spectrometer measurements have large uncertainties, and we will not consider those data further.

The region near LSIV−12°111 is characterized by appreciable interstellar extinction. Conlon *et al.* [2] estimated the color excess to be $E(B-V) = 0^m.37$ based on a comparison of the observed color indices and model-atmosphere data. However, Arkhipova *et al.* [4] have suggested that an appreciable role is also played by absorption in the circumstellar envelope. This conclusion is consistent with the upper limit $E(B-V) \leq 0^m.2$ derived from an analysis of the intensity of the λ 2200 Å interstellar band [2]. In addition, LSIV−12°111 lies between the $0^m.12$ and $0^m.15$ contours in maps of the distribution of the color

1063-7729/03/4706-0480$24.00

excess $E(B-V)$ constructed using data on the density of neutral hydrogen and galaxy source counts [5]. We corrected for the interstellar extinction using the color excess $E(B-V) = 0^m.16$, which is a mean value for 20 stars in the neighborhood of LSIV−12°111 [4]. When estimating the total absorption in the V band, $A_V = RE(B-V)$, we used the value $R = 3.3$ [6]. After accounting for interstellar extinction, the fluxes $F(\lambda)$ were derived from the observed magnitudes using data on the zero-air-mass fluxes presented by Straĭzhis [7]. Measurements of the logarithmic fluxes $F(\lambda)$ (in erg s^{-1} cm^{-2} cm^{-1}) are shown by circles in the figure.

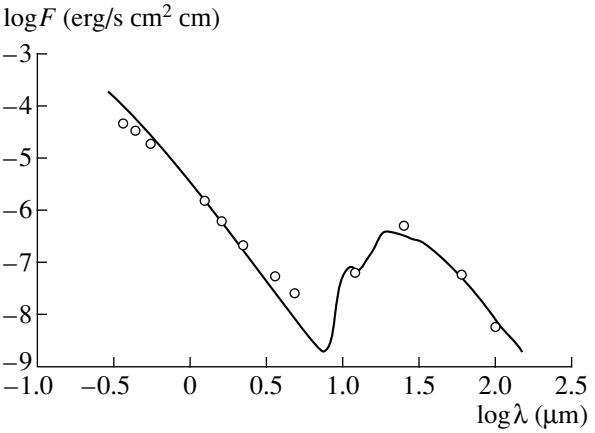

Observed fluxes from the protoplanetary nebula LSIV−12°111 (circles) as a function of the logarithm of the wavelength. The solid curve shows the SED for the computed model of the star and dust envelope.

According to the data of [1, 2], the effective temperature and mass of the central star are $T_{\rm eff} = 23\,750$ K and $M \approx 0.67\ M_\odot$. The rate at which the cores of planetary nebulae evolve depends strongly on their mass, and for the above mass, it is possible that the variations in the effective temperature would already have become observable. The absence of evolutionary effects noted in [4] argues for a somewhat lower mass for the central star. If we adopt $M \approx 0.60\ M_\odot$ and use the evolutionary tracks of planetary-nebula cores computed by Blocker [8], the luminosity of the star for the above value of $T_{\rm eff}$ is $L = 6300\ L_\odot$.

3. COMPUTATION OF THE MODEL DUST ENVELOPE

We applied the usual assumptions when computing the envelope models for LSIV−12°111. We assumed that the spherically symmetric dust envelope has a sharp inner boundary at a distance r_1 from the center, and that the concentration of dust decreases inversely proportional to the distance out to the outer boundary of the envelope at $r_2 = 1000r_1$. The optical properties of the material making up the dust grains were chosen to coincide with those of "warm" silicates [9], and their size distribution $n(a)$ is described by an MRN model [10] ($n(a) \propto a^{-q}$ for radii of spherical dust grains $a_{\rm min} \le a \le a_{\rm max}$) with $q = 3.5$, $a_{\rm min} = 0.005$ μm, and $a_{\rm max} = 0.25$ μm. The SED of the central source was taken to be a Planck spectrum whose temperature corresponds to the effective temperature of the star, $T_{\rm eff} = 23\,750$ K , and with the luminosity $L = 6300\ L_\odot$.

The radiative-transport equation in the dust envelope was solved using the DUSTY code (version 2.0) for grids with 30 points in radius and 99 wavelengths in the interval from 0.01 μm to 3.6 cm. The algorithm forming the basis of this code is described in [11, 12]. The input parameters for the models were the dust temperature at the inner boundary, T_1, and the optical depth of the envelope at 0.55 μm, τ_V. After computing the model SED, we searched for the distance d providing the minimum sum of squared differences between the observed and model fluxes. The overall best-fit values of the model parameters were $T_1 = 124$ K, $r_1 = 5.6 \times 10^{16}$ cm, $\tau_V = 0.072$, and $d = 3.8$ kpc. The solid curve in the figure shows the model SED, while the circles show the observed flux values. We can see that the model fits the observations well. The derived distance is in good agreement with the earlier estimate of 4 kpc [2]. The values of r_1 and d yield $2''.0$ for the angular diameter of the inner cavity of the dust envelope, which also agrees with the angular half-width of the line-emitting region found in [2], $1''.2 \pm 0''.2$.

We used the gas−dynamical mode of the DUSTY code with the derived optical dust of the envelope $\tau_V = 0.072$ to estimate the parameters of the stellar wind of LSIV−12°111 arising due to the action of radiation pressure on the dust and the subsequent transfer of momentum to the gaseous medium. In this case, a self-consistent procedure for solving for the radiative transport and the motion of the dust in the stellar envelope is realized [13]. It was assumed that the density of the dust grains ρ_d was 3 g/cm^3 and that the ratio of the gas and dust masses in the envelope r_{gd} was 200. Using these data, the DUSTY code computed the total mass-loss rate to be $\dot{M} = 1.0 \times 10^{-5}\ M_\odot$/yr. When required, $\dot{M}$ can easily be recalculated for other values of ρ_d and r_{gd}, using the fact that $\dot{M} \propto (\rho_d r_{gd})^{1/2}$ [13]. Note that this result was obtained for modern values of the parameters of the star and dust envelope. In addition, we have not taken into account the radiation pressure on the neutral gas and ionized matter in the nebula. Therefore,

the derived value of $\dot{M}$ should be treated as a lower limit to the mass-loss rate.

4. CONCLUSIONS

In spite of the comparatively small amount of observational data available, the good coincidence between the observed fluxes and the model spectral energy distribution suggests that the derived parameters of the dust envelope of LSIV−12°111 are fairly close to their real values. This envelope was probably ejected by the star when it was leaving the asymptotic giant branch. If we take the mass of the star to be $M \approx 0.60\ M_\odot$, then the evolutionary computations of Blocker [8] indicate that a time Δt of about 1500 yrs should have elapsed since then. A rough estimate of the mean velocity $V = r_1/\Delta t$ yields the value 12 km/s, consistent with the observed expansion velocities of planetary nebulae.

It is of interest to compare the parameters for the envelope of LSIV−12°111 with the values determined by us earlier for the similar objects V886 Her [14] and V1853 Cyg [15]. In the case of V886 Her, we found $T_1 = 410$ K, $r_1 = 4.3 \times 10^{15}$ cm, and $\tau_V = 0.48$. The dust envelope is located appreciably closer to the star, and is both denser and hotter. This provides evidence that the envelope was ejected comparatively recently. The mass of the central star of V886 Her is $M \approx 0.70\ M_\odot$, and it displays rapid evolutionary variations in its effective temperature [16]. The evolutionary tracks of Blocker [8] indicate that $\Delta t \approx 100$ yrs and the expansion velocity of the envelope is $V = 12$ km/s. In spite of the substantially higher optical depth of its envelope, the mass-loss rate of V886 Her is lower than that of LSIV−12°111 and is equal to $\dot{M} = 4.5 \times 10^{-6}\ M_\odot$/yr. The model parameters for V1853 Cyg are closer to the values for LSIV−12°111: $T_1 = 110$ K, $r_1 = 7.6 \times 10^{16}$ cm, $\tau_V = 0.18$, and $\dot{M} = 2.2 \times 10^{-5}\ M_\odot$/yr. If the mass of the central star is $M \approx 0.60\ M_\odot$, the evolutionary computations of [8] yield a time Δt of about 1300 yrs and an estimated mean expansion velocity of $V = 19$ km/s.

5. ACKNOWLEDGMENTS

The author is grateful to astrophysicists of the University of Kentucky Zeljko Ivezic, Maia Nenkova, and Moshe Elitzur for making possible the use of the DUSTY program for solving the radiative-transport equations and also to the collectives of the SIMBAD and ISO databases for making available observational data for LSIV−12°111. This work was supported by grants from the State Science and Technology Program "Astronomy," the Ministery of Education of the Russian Federation, and the program "Universities of Russia" (grants E00-11.0-31 and UR.02.01.003).

REFERENCES

1. R. J. H. McCausland, E. S. Conlon, P. L. Dufton, and F. P. Keenan, Astrophys. J. **394**, 298 (1992).
2. E. S. Conlon, P. L. Dufton, R. J. H. McCausland, and F. P. Keenan, Astrophys. J. **408**, 593 (1993).
3. K. M. Volk and S. Kwok, Astrophys. J. **342**, 345 (1989).
4. V. P. Arkhipova, N. P. Ikonnikova, R. I. Noskova, and G. V. Komissarova, Pis'ma Astron. Zh. **28**, 298 (2002) [Astron. Lett. **28**, 257 (2002)].
5. D. Burstein and C. Heiles, Astron. J. **87**, 1165 (1982).
6. C. Allen, *Astrophysical Quantities* (Athlone, London, 1973; Mir, Moscow, 1977).
7. V. L. Straĭzhis, *Multicolos Star Photometry* [in Russian] (Mokslas, Vilnyus, 1977).
8. T. Blocker, Astron. Astrophys. **299**, 755 (1995).
9. V. Ossenkopf, T. Henning, and J. S. Mathis, Astron. Astrophys. **261**, 567 (1992).
10. J. S. Mathis, W. Rumpl, and K. H. Nordsieck, Astrophys. J. **217**, 425 (1977).
11. Z. Ivezic and M. Elitzur, Mon. Not. R. Astron. Soc. **287**, 799 (1997).
12. Z. Ivezic and M. Elitzur, Mon. Not. R. Astron. Soc. **303**, 864 (1999).
13. Z. Ivezic and M. Elitzur, Astrophys. J. **445**, 415 (1995).
14. M. B. Bogdanov, Astron. Zh. **77**, 772 (2000) [Astron. Rep. **44**, 685 (2000)].
15. M. B. Bogdanov, Pis'ma Astron. Zh. **28**, 685 (2002) [Astron. Lett. **28**, 617 (2002)].
16. V. P. Arkhipova, N. P. Konnikova, R. I. Noskova, *et al.*, Pis'ma Astron. Zh. **25**, 30 (1999) [Astron. Lett. **25**, 25 (1999)].

Translated by D. Gabuzda

Astronomy Reports, Vol. 47, No. 6, 2003, pp. 483–491. Translated from Astronomicheskiĭ Zhurnal, Vol. 80, No. 6, 2003, pp. 526–534.

Estimates of Relaxation Times in Numerical Dynamical Models of Open Star Clusters

V. M. Danilov and L. V. Dorogavtseva

Astronomical Observatory, Ural State University, pr. Lenina 51, Yekaterinburg, 620083 Russia

Received June 25, 2002; in final form, January 10, 2003

Abstract—Relaxation times in the spaces of several stellar-motion parameters are obtained for a number of open-cluster models. The differences between the relaxation times in these spaces increase with the degree of nonstationarity of the cluster models. In the course of the cluster's evolution, the relaxation times increase in all the spaces considered. During violent relaxation, the stars occupy all domains accessible to them, first in absolute velocity and then in clustercentric distance. The dependence of the coarse-grained phase-space density of the cluster on small initial perturbations of the phase-space coordinates of its constituent stars tends to decrease at times exceeding the time scales for violent and "collisional" relaxation. © *2003 MAIK "Nauka/Interperiodica".*

INTRODUCTION

During violent relaxation in models of open star clusters [1–3], the equilibrium distribution of stars is conserved in the space corresponding to the three parameters of the stellar motion ε, l, and ε_ζ (the energy, angular momentum, and energy of the star's motion perpendicular to the Galactic plane per unit mass of the star). According to [1], this equilibrium exists in open-cluster (OC) models from the very beginning of their evolution until the end of the computations performed. In the OC models of [1–3], neither virial nor thermodynamical equilibrium are attained as t increases, and the virial coefficient for the cluster models at $t > \tau_{vr}$ continues to oscillate with nearly constant amplitude and the period P_r. The distributions of ε, ε_ζ, and l for the motions of individual stars remain well preserved over time intervals Δt on the order of P_r (where τ_{vr} is the initial time scale for violent relaxation for the cluster model). Danilov [2] determined the equilibrium phase-space density function of the number of stars corresponding to the equilibrium of the OC models in ε. This equilibrium is incomplete, because the coordinate and velocity distributions of the stars and the potential of the regular forces vary with the period P_r, and the phase-space density function in such models remains well preserved on time scales of the order of P_r. Violent relaxation proceeds under the conditions of this equilibrium in phase space, and leads to the development of an "equilibrium" oscillatory process whose parameters vary little with time. In his analysis of stellar fluxes in phase space, spaces of ε, l, and ε_ζ, and a number of other spaces of the cluster models, Danilov [1] found that there was an energy flux toward the cluster center, and a transfer of energy from large-scale to small-scale motions within the clusters. The dispersions of the increments of the stellar parameters ε, l, and ε_ζ over a time Δt obtained in [1] using the distributions of the stellar fluxes in ε, l, and ε_ζ can be used to estimate the relaxation times of the OC models in these spaces.

According to El-Zant [4], various dynamical quantities (including the particle energies) in N-body gravitating systems with exponentially unstable orbits may relax toward equilibrium at different rates. Indeed, small and slow variations of the particle energies in such systems can result in appreciable and rapid changes in the particle trajectories. Moreover, the phase space of such systems may contain barriers that slow the diffusion across them [4, 5, p. 155]. Therefore, the system's relaxation time in energy space may differ from the time scale for the development of trajectory instabilities in phase space [4].

Estimates of the local violent-relaxation time t_r based on the instability of the cluster phase-space density function relative to small initial perturbations of the phase-space coordinates of the stars have been obtained for only two OC models [3, 6]. The cluster models of [3, 6] were computed by integrating the stellar equations of motion using sixth- and seventh-order difference schemes over a time interval $t \in [0, t_0]$, where $t_0/\tau_{vr} \simeq 1.7$–2.2 and t_0 is the time interval for the dynamical evolution of the OC model over which the statistical criterion for computational accuracy of [7] is satisfied (in this case, the accuracy of the computed cluster phase-space density function can be considered sufficient to yield meaningful conclusions about its statistical properties). It is of inter-

1063-7729/03/4706-0483$24.00

Table 1. Parameters of open-cluster models

Model number	R_1/R_2	N_1/N_2	N_1	R_2/R_t	$\langle R\rangle/R_t$	$\langle\delta\alpha/\alpha\rangle$
1	0.24	0.25	100	0.9	0.57	0.53 ± 0.09
2	0.24	0.25	100	0.8	0.51	0.28 ± 0.03
3	0.34	0.67	200	0.8	0.44	0.15 ± 0.02
4	0.24	0.25	100	0.7	0.45	0.14 ± 0.02
5	0.45	1.50	300	0.8	0.40	0.07 ± 0.03
6	0.63	4.00	400	0.8	0.42	0.06 ± 0.03

est to construct OC models and analyze the characteristic features of the instability of their phase-space density functions at large t_0 due to the instability of the stellar trajectories relative to small variations in the initial phase-space coordinates of the stars. This requires that we increase the accuracy of the difference schemes used in the computations (which will enable the computations to more completely cover the ranges of the observed densities of open clusters and of the parameters of their core–halo structure [8]).

Estimates of the relaxation times for OC models based on the stellar fluxes in ε, l, and ε_ζ have been obtained for only five models [1]. It is of interest to increase both the number of models with such estimates and the number of stellar-motion parameters used to derive the relaxation times. Such estimates are of considerable interest for studies of the characteristic features of the diffusion of stars in the cluster-model phase space.

The aim of the current paper is to analyze the characteristics of the development of equilibrium in OC models that are nonstationary in the regular field and to estimate the relaxation times in such systems. One of our goals is to increase the accuracy of the difference schemes used to compute the stellar trajectories in the OC models.

DESCRIPTION OF THE MODELS

Following [1–3], we will consider a cluster containing $N = 500$ stars that moves in the Galactic plane in a circular orbit of radius 8200 pc about the Galactic center. At the initial time $t = 0$, the cluster is modeled as a system of two gravitating spheres with coincident centers of mass, imitating the halo and core. We analyzed six such OC models, whose parameters are summarized in Table 1. The first column of Table 1 (and Table 2 below) gives a sequence of numbers identifying the OC models. The initial parameters R_1/R_2 and N_1/N_2 (columns 2 and 3 of Table 1) for all the OC models satisfy the observed relation $R_1/R_2 \simeq 0.39 \times (N_1/N_2)^{0.35}$ [8]. Here, R_1 and R_2 are the radii of the cluster core and halo, respectively, and N_1 and N_2 are the numbers of stars in the core and halo, respectively (the initial N_1 is given in column 4 of Table 1). The masses of the stars in the models are equal to $1M_\odot$. As in [1–3], we will analyze the motion of the cluster stars in a rotating coordinate system (ξ, η, ζ) fixed to the cluster center of mass. The ξ, η, and ζ axes are directed from the cluster center of mass toward the Galactic anticenter, along the motion of the cluster in the Galactic plane, and perpendicular to the Galactic plane, respectively. We computed our OC models using the stellar equations of motion (5.517)–(5.519) adopted from [9] and written in terms of (ξ, η, ζ). We adopted the Galactic potential in the form suggested by Kutuzov and Osipkov [10] and specified the initial positions and velocities of the stars using a random-number generator, so that the cluster does not rotate relative to external galaxies at $t = 0$, and the initial stellar number densities at various points in the subsystems (halo and core) are approximately constant. The magnitudes of the velocities of the stars of subsystem i are computed using the formula

$$v_i = \sqrt{C_i U(r)}, \quad i = 1, 2, \tag{1}$$

where $r = |\mathbf{r}|$, $\mathbf{r} = (\xi, \eta, \zeta)$ is the radius vector of the star in the cluster, $U(r)$ is the gravitational potential of the cluster, and the subscripts $i = 1, 2$ correspond to the cluster core and halo, respectively. The constants C_i are chosen so that the cluster and its subsystems obey the conditions of virial equilibrium at $t = 0$, neglecting the effect of the gravitational field of the Galaxy [11]. We specified r and the directions of the vectors $\mathbf{r}$ and $\mathbf{v}$ using a random-number generator, in accordance with the technique described in [3] for cluster model 2. In our computations, we used pc, Myr, and $M_\odot$ as units and smoothed the force functions on the right-hand sides of the stellar equations of motion (see [12] for a description of the smoothing technique and smoothing parameter used).

Columns 5 and 6 of Table 1 give the initial values of R_2/R_t and $\langle R\rangle/R_t$ for the cluster models. Here, R_t is the tidal radius for the stability of the cluster in the gravitational field of the Galaxy obtained using the criterion of King [13] and $\langle R\rangle$ is the mean cluster-centric distance of the stars.

The degree of nonstationarity of the OC models in the regular field is determined by the amplitude of the oscillations of the virial coefficient $\delta\alpha$, where $\alpha = 2E_c/W$, $E_c = T + W$, and T and W are the kinetic and potential energy of the cluster, respectively, neglecting the effect of the gravitational field of the Galaxy (as in [1–3]). Using different initial values of R_1/R_2, N_1/N_2, and R_2/R_t in models 1–6 results in different degrees of nonstationarity of the

Table 2. Relaxation times for the open-cluster models

Model number	$t_{r,c}^{(1)}$	$t_{r,c}^{(2)}$	$t_{r,h}$	τ_{st}	τ_ε	τ_l	τ_{ε_ζ}	τ_r	τ_v
1	0.5	1.0–1.1	1.2–1.3	2.6	5.2 ± 0.8	2.2 ± 0.3	1.2 ± 0.1	1.9 ± 0.5	0.8 ± 0.1
								(1.3–3.0)	(0.6–1.0)
2	0.5	1.2–1.4	1.5–1.6	2.6	4.7 ± 0.5	3.1 ± 0.3	1.1 ± 0.1	1.8 ± 0.2	0.7 ± 0.1
								(1.2–2.1)	(0.6–0.8)
3	0.5	1.1–1.2	1.1–1.4	2.1	4.2 ± 0.5	2.8 ± 0.4	0.8 ± 0.1	1.3 ± 0.2	0.60 ± 0.04
								(1.0–1.6)	(0.5–0.7)
4	0.5	1.0–1.2	1.2–1.3	2.6	4.4 ± 0.4	3.2 ± 0.5	0.9 ± 0.1	1.6 ± 0.2	0.7 ± 0.1
								(1.2–2.0)	(0.6–0.9)
5	0.5	1.2–1.4	1.4	1.8	3.5 ± 0.5	2.9 ± 0.4	0.80 ± 0.05	1.0 ± 0.1	0.60 ± 0.05
								(0.6–1.2)	(0.5–0.8)
6	0.6–0.7	1.4–1.5	1.9–2.0	1.9	2.7 ± 0.5	3.2 ± 0.3	1.1 ± 0.1	0.9 ± 0.1	0.7 ± 0.1
								(0.6–1.2)	(0.6–0.8)

models. The mean ratio of the amplitudes $\delta\alpha$ of the oscillations of the virial coefficient α to its mean value $\alpha = \alpha_v$ averaged over the period P_r of the oscillations of the regular field are listed in column 7 of Table 1. Models 1–6 in Table 1 are listed in order of decreasing degree of nonstationarity.

Columns 2–4 of Table 2 give estimates of the local relaxation times $t_{r,c}^{(1)}$ and $t_{r,c}^{(2)}$ for the cluster core and $t_{r,h}$ for the cluster halo in units of $\tau_{vr} = 2.6\overline{t}_{cr}$ [3], based on the instability of the model phase-space density functions relative to small perturbations of the stellar phase-space coordinates. Here, $\overline{t}_{cr}$ is the mean initial cluster crossing time for a star. Column 5 of Table 2 gives estimates of the collisional relaxation times τ_{st} for the models in units of τ_{vr}. We estimated τ_{st} using formula (2.379) of Chandrasekhar [9] for the time $t = 0$ (using the OC parameters at $t = 0$). Columns 6–10 of Table 2 give estimates of the relaxation times in ε, l, ε_ζ, r, and v in units of τ_{vr}; here, $v = |\mathbf{v}|$ is the magnitude of the velocity of a cluster star. These estimates are based on the fluxes of the stars in $\varepsilon, l, \varepsilon_\zeta, r$, and v, in accordance with the technique described in [1].

At $t = 0$, model 1 of the current paper coincides with model 2 of [3] and model 1 of [1]. Here, we refine our estimates of t_r (columns 2–4 of Table 2) and estimate the times τ_r and τ_v (the cluster relaxation times in r and v). Cluster models 4 and 6 here coincide with models 2 and 3 of [1] (here, we obtained estimates of t_r, τ_r , and τ_v for these models). Table 2 gives the times τ_ε, τ_l, and τ_{ε_ζ} for models 1, 4, and 6 adopted from [1].

PRINCIPAL FORMULAS AND COMPUTATIONAL TECHNIQUES

The stellar equations of motion were integrated using eighth- and ninth-order Runge–Kutta schemes, specifying five and six grids in the interval for integration over t. The step in t for each grid was determined by the formula

$$h_k = h_1/2^{k-1}, \quad k = 1, ..., n, \tag{2}$$

where $n = 5$ and $n = 6$ for the cases of five and six grids. The grid points with different k coincide at the time intervals $\Delta t = h_1 = 2h_2 = 4h_3 = 8h_4 = 16h_5$ and $\Delta t = h_1 = 2h_2 = 4h_3 = 8h_4 = 16h_5 = 32h_6$ for five and six grids, respectively. If $u = (\xi, \eta, \zeta, \dot{\xi}, \dot{\eta}$, and $\dot{\zeta})$ are the phase-space coordinates of a cluster star and $\varphi^{(k)}$ is the grid function approximating $u(t)$ and computed on grid number k using a fourth-order Runge–Kutta method, an approximate solution to $u(t)$ at the coincident grid points is given by a linear combination of the $\varphi^{(k)}$:

$$\tilde{\varphi} = \sum_{k=1}^{n} a_k \varphi^{(k)}, \tag{3}$$

where a_k are constant coefficients for the grid functions (3) in the following form, obtained in accordance with [14]. We have for the five-grid function

$$a_1 = \frac{63}{\Delta_1}, \quad a_2 = \frac{-15120}{\Delta_1}, \quad a_3 = \frac{1128960}{\Delta_1}, \quad a_4 = \frac{-30965760}{\Delta_1}, \quad a_5 = \frac{264241152}{\Delta_1}, \tag{4}$$

where $\Delta_1 = 234389295$. We have for the six-grid function

$$a_1 = \frac{-3}{\Delta_2}, \quad a_2 = \frac{1488}{\Delta_2}, \quad a_3 = \frac{-238080}{\Delta_2}, \quad a_4 = \frac{15237120}{\Delta_2}, \quad a_5 = \frac{-390070272}{\Delta_2}, \quad a_6 = \frac{3221225472}{\Delta_2}, \tag{5}$$

where $\Delta_2 = 2846155725$.

Our computations had a precision of 15–16 decimal digits. The maximum relative errors in the computed "energy" E (see (5.522) in [9]) over the time interval t_0 did not exceed 2.8×10^{-13}, 1.6×10^{-13}, 1.1×10^{-13}, 9.0×10^{-14}, 9.0×10^{-14}, and 1.0×10^{-13} in cluster models 1, 2, 3, 4, 5, and 6, respectively. The statistical criterion [7] for the accuracy of the computations of the phase-space density functions remained satisfied for evolutionary time intervals of $t_0/\tau_{vr} = 2.7$, 2.8, 2.7, 2.9, 2.8, and 3.5 for cluster models 1, 2, 3, 4, 5, and 6, respectively. The use of the grid functions (3) made it possible to increase the accuracy of the computations over that attained in [3] using sixth- and seventh-order Runge–Kutta methods and also to increase the time interval t_0 during which the computed evolution of model 1 satisfies the statistical accuracy criterion from $2.2\tau_{vr}$ [3] to $2.7\tau_{vr}$. Here, as in [1, 2], we set the initial violent-relaxation time equal to $\tau_{vr} = 2.6\overline{t}_{cr}$, where $\overline{t}_{cr}$ is the mean initial crossing time for a cluster star. The violent-relaxation time in millions of years is $\tau_{vr} \simeq 50$, 42, 42, 34, 42, and 42 in cluster models 1, 2, 3, 4, 5, and 6, respectively.

As in [6], the estimates of the relaxation times t_r in columns 2–5 of Table 2 were obtained by comparing two versions of each cluster model, **a** and **b**. We computed these versions over the time interval t_0 using a ninth-order difference scheme [formulas (3) and (5)]. The initial phase-space coordinates of the stars in model versions **a** and **b** differ slightly, by amounts specified as described in [7]. For version **a** of each OC model, we partitioned the phase-space domain occupied by the cluster stars into cells. At time t, the 500 cluster stars were subdivided into groups of 50 stars in order of increasing r. Each such group occupies an interval $r \in L_i(t) \equiv (r_{50\times(i-1)+1}, r_{50\times(i-1)+1} + \Delta r_i]$ for $i = 2, ..., 10$, where the r are numbered in increasing order. For $i = 1$, we have $L_i \equiv [r_{50\times(i-1)+1}, r_{50\times(i-1)+1} + \Delta r_i]$. The indices of the stars whose phase-space coordinates are used to compute r do not coincide with the indices of the r values. In the notation adopted here, we have $r_{50\times i} = r_{50\times(i-1)+1} + \Delta r_i$. The domain occupied by the cluster stars in velocity space $(\dot\xi, \dot\eta, \dot\zeta)$ is partitioned into m equal cells [6] ($\dot\xi = \frac{d\xi}{dt}$, with $\dot\eta$ and $\dot\zeta$ defined analogously). Let l_ξ, l_η, and l_ζ be the dimensions of such a cell in the $\dot\xi, \dot\eta$, and $\dot\zeta$ directions. The phase-space volume of the cell containing stars from the interval L_j is $Q(j) = q \times \frac{4}{3}\pi({r^3}_j - {r^3}_{j-1})$, where $q = l_\xi l_\eta l_\zeta$ is the volume of the cell in velocity space; the number m of such cells in velocity space was 1000, $j = 1, ..., 10$, and $r_0 = 0$.

Let $n_{ij}^{(a)}$ be the number of stars from the ith cell in velocity space and L_j be the radius interval in version **a** of the OC model. The phase-space density function of this model version is $f_{ij}^{(a)} = n_{ij}^{(a)}/Q(j)$, where f_{ij} is the coarse-grained phase-space density. The mean relative difference between the phase-space density functions of model versions **a** and **b** in the radius interval $r \in L_j$ is

$$\psi_j = \frac{\sum\limits_{i=1}^{m} |n_{ij}^{(a)} - n_{ij}^{(b)}|}{\frac{1}{2}\sum\limits_{i=1}^{m}(n_{ij}^{(a)} + n_{ij}^{(b)})}, \quad j = 1, ..., 10. \tag{6}$$

In (6), the common factor $Q(j)$ in the numerator and denominator has been canceled out.

To study the fluxes of stars in the space of the energies ε, we subdivided all the cluster stars at time t into groups of 50 stars in order of increasing ε (analogous to partitioning the r space into L_i intervals). The stars of the ith group then occupy an interval of size $\Delta\varepsilon_i$ in ε space, with $j = 1, ..., 10$. Let $n^{(\varepsilon)}(i, j)$ denote the number of stars moving from the ith to the jth interval in ε space during the time Δt. According to [1], the mean number of transitions by j intervals in ε space during a time Δt is

$$\nu^{(\varepsilon)}(j) = \begin{cases} \frac{1}{10+j}\sum\limits_{i=1-j}^{10} n^{(\varepsilon)}(i, i+j), & j = -9, ..., -1 \\ \frac{1}{10-j}\sum\limits_{i=1}^{10-j} n^{(\varepsilon)}(i, i+j), & j = 0, 1, ..., 9. \end{cases} \tag{7}$$

Formulas (7) average the numbers of all possible transitions of stars by j intervals in ε space. Values $j > 0$ (< 0) correspond to an increase (decrease) of the star's energy ε as a result of such a transition. The value $j = 0$ corresponds to transitions of stars in ε space from the ith into the ith interval. Thus, $\nu^{(\varepsilon)} = \nu^{(\varepsilon)}(j)$ is the j distribution of the mean numbers of stellar transitions in ε during the time Δt. If this distribution is symmetric about $j = 0$, there is a balance of stellar transitions in ε space. The dispersion σ_ε^2 of j obtained using this distribution carries information about the characteristic rate of

change of the stellar energies and the relaxation time in ε space [1]. The number of intervals $\Delta\varepsilon$ through which a star moves in the direction of increasing (decreasing) ε is, on average, $v_\varepsilon = 0.5\sigma_\varepsilon/\Delta t$. The greater v_ε, the faster the motion of the stars and the relaxation of the system in ε. Because the cluster occupies ten intervals $\Delta\varepsilon$ in ε space [see discussion of (7)], the relaxation time of the cluster in ε space is $\tau_\varepsilon = 10/v_\varepsilon = 2\tau_{vr}/\sigma_\varepsilon$ (here, we have used the fact that $\Delta t = 0.1\tau_{vr}$). Thus, τ_ε is the mean time it takes a star to change its energy ε by an amount of the order of the size of the cluster in ε space under the action of all forces and mechanisms operating in the cluster. We can similarly determine the cluster relaxation times τ_l and τ_{ε_ζ} in l and ε_ζ.

COMPUTATION RESULTS AND DISCUSSION

By the time $t \simeq (0.30\text{–}0.38)\tau_{vr}$, the contraction of the OC models (primarily perpendicular to the Galactic plane) ceases, and, at $t > 0.3\tau_{vr}$, oscillations in the regular field are established, with periods of $P_r/\tau_{vr} \simeq 0.59, 0.65, 0.67, 0.74$, and 0.64 in models 1, 2, 3, 4, and 5, respectively. In model 6, the period of the oscillations in ζ is $P_\zeta \simeq 0.6\tau_{vr}$, and the periods of the oscillations in ξ and η are $P_{\xi,\eta} \simeq P_\xi \simeq P_\eta \simeq 1.2\tau_{vr}$ (in this model, the phases of the cluster oscillations are approximately the same in ξ and η, and the period of the oscillations in the (ξ, η) plane is twice the period in ζ, as described in [1]). All the OC models exhibit a weak decrease of the amplitude of the oscillations of the virial coefficient α with time.

We computed ψ_i for models 1–6 over time intervals of $(3\text{–}4)\tau_{vr}$. In all the OC models, ψ_i varies appreciably in a random and jumplike fashion as t increases (for small variations of t), and we therefore smoothed these variations using a moving average over three ψ_i values for adjacent times t. On all the smoothed plots, there are intervals of approximately linear time variations of $\psi_i = \psi_i(t)$ (see the dependences $\psi_i = \psi_i(t)$ for cluster models 2, 4, and 6 in Fig. 1). All the OC models pass through a stage of rapid growth of ψ_i with t at the beginning of their evolution (the stage of violent relaxation). This is due to the exponential divergence of the stellar trajectories in versions **a** and **b** of each cluster model, and the instability of the phase-space density function relative to small perturbations of the stellar phase-space coordinates. The stage of rapid growth of ψ_i ends at times $t = t_{r,c}^{(1)}$ and $t = t_{r,h}$ in the cluster core and halo, respectively. Columns 2 and 4 of Table 2 present $t_{r,c}^{(1)}$ and $t_{r,h}$ for models 1–6.

For the cores of cluster models 1–5, $t_{r,c}^{(1)} \simeq 0.5\tau_{vr}$, and only in the densest model (model 6), we find $t_{r,c}^{(1)} \simeq (0.6\text{–}0.7)\tau_{vr}$. The ratios $t_{r,h}/\tau_{vr}$ for the halos of models 1–6 lie in the interval 1.1—2.0. For all the OC models, we determined the tidal cluster radius R_t^- for stars moving in retrograde orbits at time $t = t_{r,h}$ (using the method described in [12]). The tidal radii R_t^- vary only slightly with time when $t > \tau_{vr}$. To estimate $t_{r,h}$, we used the functions $\psi_i(t)$ obtained from the stellar phase-space coordinates for the radius interval $r \in L_i$ containing $r = R_t^-$ and the interval L_{i-1}. The Figure shows plots of the corresponding dependences $\psi_i(t)$ for the halos of cluster models 2, 4, and 6. When $t > t_{r,h}$, the functions ψ_i in the halo slowly decrease (or remain nearly constant in cluster models 3 and 4).

When $t \simeq t_{r,c}^{(1)}$, the rate of growth of ψ_i with time t changes in the cores of the OC models. When $t_{r,c}^{(1)} < t < t_{r,c}^{(2)}$, the cores of models 1–6 are characterized by a slow and approximately linear increase in ψ_i. This stage of the core evolution ends by $t = t_{r,c}^{(2)}$. Column 3 of Table 2 lists $t_{r,c}^{(2)}$ for each cluster model. When $t > t_{r,c}^{(2)}$, the functions ψ_i in the cores of models 1–6 decrease with time until the end of the computations (in the core of model 6, this decrease is most evident for $i = 3, 4$).

The changes in the rates of change of ψ_i in the cluster core and halo at $t \simeq t_{r,c}^{(1,2)}$ and $t \simeq t_{r,h}$ are indicative of changes in the instability of the phase-space density function relative to small initial perturbations of the stellar phase-space coordinates. The decrease in the rate of growth of ψ_i at $t_{r,c}^{(1)} < t < t_{r,c}^{(2)}$ in the cores of cluster models 1–6 reflects a further divergence of the phase-space density functions in model versions **a** and **b**, which is slower than at $t < t_{r,c}^{(1)}$. Note that $t_{r,c}^{(1)}$ agrees well with the first τ_v value in parentheses in column 10 of Table 2, which is reached at time $t \simeq t_{r,c}^{(1)}$.

During violent relaxation, stars with energies ε tend to occupy all domains in (r, v) space accessible to them, first in v and then in r. This behavior results in a decrease in the rates of growth of ψ_i. The violent relaxation in phase space proceeds in the same sequence: it is faster in velocity space $(\dot\xi, \dot\eta, \dot\zeta)$ and slower in coordinate space (ξ, η, ζ). At $t \simeq \tau_v$, the change in the growth rates of ψ_i also becomes appreciable in the halo (especially in model 6), although the ψ values of models 1–5 remain small and are distorted by random fluctuations, making the rates of growth of ψ_i difficult to estimate.

According to Table 2, the values of $t_{r,c}^{(2)} \simeq t_{r,h}$ for OC models 1–5 agree well with the lower estimates τ_r derived from the stellar fluxes in r for models 1–4

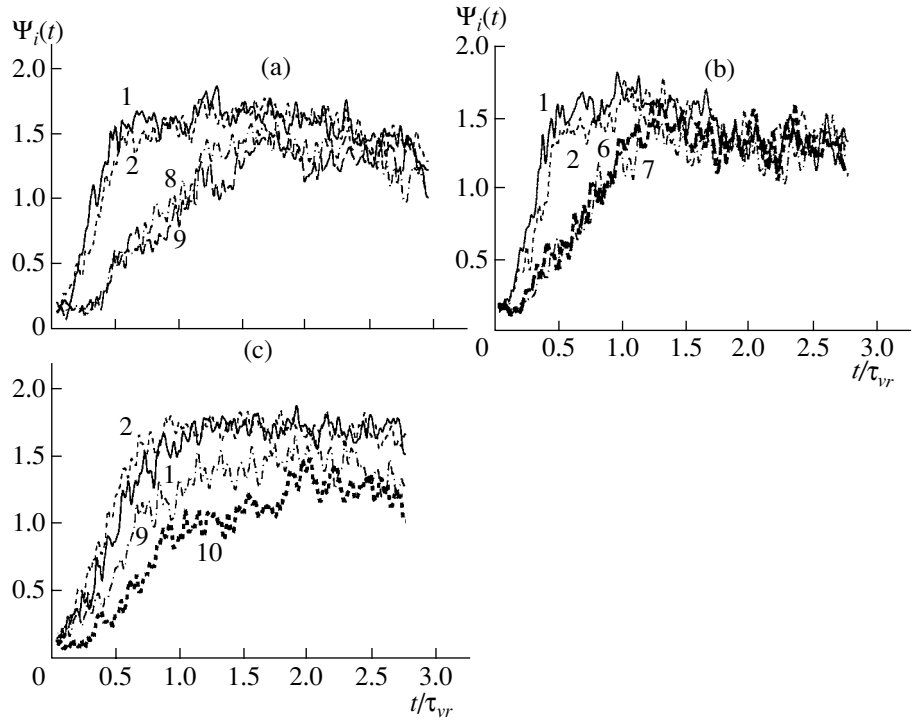

Fig. 1. Time dependences of $\psi_i(t)$ in cluster models (a) 2, (b) 4, and (c) 6. The numbers i are indicated alongside the corresponding dependences $\psi_i(t)$.

at $t < t_{r,h}$ (see the first τ_r value in parentheses in column 9). By times $t \simeq t_{r,h} \simeq \tau_r$, violent relaxation has ended throughout the cluster (in both the core and halo), and the equilibrium oscillatory process in the cluster can be considered to be established [1]. The derived $t_{r,h}$ and τ_r values can probably be viewed as independent estimates of the violent relaxation time for the cluster as a whole. During the subsequent evolution, ψ_i in the cluster halos usually decreases with time. This behavior indicates a convergence of the equilibrium phase-space density functions in model versions **a** and **b** (because ψ_i in the cores of all the OC models also decreases when $t > t^{(2)}_{r,c} \simeq t_{r,h}$; see above). The ψ_i increase when $t > t_{r,h}$ at the periphery of the least dense cluster, since stars at radii $r \in L_i$ have $r > R_t^-$ and move away from the cluster with various velocities and accelerations in the gravitational field of the Galaxy. Note that, in this case, the distances between the stars in the interval L_i in r and v space increase with the difference between the velocities in model versions **a** and **b** (since the running and total numbers of stars in L_i are not the same in these models). As a result, ψ_i increases slowly at the peripheries of such clusters.

According to Table 2, $t_{r,h} < \tau_{st}$ for cluster models 1–5 and $t_{r,h} \simeq \tau_{st}$ for model 6. Note that model 6 is closer to virial equilibrium than the other models. Model 6 satisfies to a greater degree the assumptions made when deriving formula (2.379) in [9]. Therefore, the quantity τ_{st} from Table 2 more accurately characterizes the efficiency of stellar encounters for model 6 than for the other models. Stellar encounters at $t > \tau_{st}$ play a very important role in the evolution of the clusters. On the one hand, stellar encounters give rise to small density oscillations in the cluster, which are easily amplified to the level of large-scale oscillations (since the OC models are close to gravitational instability [1, 2]). On the other hand, the variations of the regular field of the cluster over the oscillation period lead to the development of a flux of stellar energy toward the cluster center (due to "heating" of the cluster by its variable regular field), and the energy ε is transferred from large-scale to small-scale stellar motions [1]. The energy coming into a phase-space element of the cluster due to this flux is probably redistributed in the cluster via the diffusion of stars in phase space due to stellar encounters. This redistribution of the stellar energies should result in a gradual decay of the large-scale oscillations in the cluster (as we can see in the time dependences of the virial coefficient $\alpha = \alpha(t)$ for the models; see Fig. 1 in [1]) and a slow evolution of the equilibrium phase-space density functions of versions **a** and **b** of the models [3]. The relative importance of stellar encounters and "collisional" relaxation in the evolu-

tion of the models should increase with decreasing nonstationarity of the models.

If the ψ_i decrease to zero with increasing t at $t > t_0$, the above mechanisms should lead to a convergence of the phase-space density functions in model versions **a** and **b**, and to the development of identical (in a statistical sense) phase-space density functions in these two versions. In this case, a coarse-grained phase-space density function that is independent of small initial perturbations of the stellar phase-space coordinates should develop at large t as a result of stellar encounters. However, the only way to verify this is to increase the accuracy with which the stellar equations of motion are integrated. If the ψ_i do not decrease to zero at large t, the statistical differences between the phase-space density functions in the two model versions will be preserved.

Thus, the diversity of the conditions for the formation of a cluster brings about an even greater diversity in the forms and structures of OCs during the evolutionary stage when there are substantial periodic variations of the regular field of the cluster. Examples of such forms and structures observed in OCs are discussed in [8, 15]. If the ψ_i tend to zero at large t as a result of stellar encounters, the corresponding distribution of stellar radii r should no longer depend on small initial variations of the stellar phase-space coordinates. We note in this connection that fairly old open clusters develop the often observed simple "core–halo" structure (see the conclusion of Kholopov about the universality of the structure of stellar clusters [16, p. 329]).

The mass density and importance of stellar encounters are higher and the "collisional" relaxation times shorter in the cluster cores than in the halos. This may explain why the ψ_i in the cores of cluster models 1–5 decrease faster at $t_{r,c}^{(2)} < t < t_0$ than they do at the periphery at $t > t_{r,h}$, so that ψ_i in the cores and halos of these OC models approach each other (panels a and b of the Fig. 1). In model 6, the mass of the halo is small compared to that of the core, and the evolution of the entire system over the time $t \in [0, t_0]$ is determined by the evolution of the core. This may explain why the $\psi_i(t)$ dependences in the core and halo of model 6 resemble each other.

As in [1], all the OC models are characterized by a balance of the stellar fluxes in $\varepsilon, l, \varepsilon_\zeta$, and r from the start of the OC evolution until the end of the computations (the properties of the flux balance in r are described in [1], and there is no balance of the stellar fluxes in v). The distributions $\nu(j)$ of the numbers of transitions of stars in $\varepsilon, l, \varepsilon_\zeta$, and r are symmetric with respect to $j = 0$ and have approximately the same form for each such space (for model 1, see Fig. 2 in [1]). The equilibrium distributions of the stars in ε, l, and ε_ζ persist throughout the dynamical evolution of these models, and the equilibrium phase-space density function corresponding to the balance of fluxes in ε determines the structure of these cluster models from the very beginning of their evolution.

Thus, some equilibrium phase-space density function exists at any stage of the dynamical evolution of a gas- and dust-free OC, and this equilibrium function can always be derived from the coordinates and velocities of the stars (in accordance with the technique described in [2]). If no data on the stellar velocities are available, this phase-space density function can be computed using the distribution $f(\varepsilon, l, \varepsilon_\zeta)$; see formula (4) in [2]. Integration of $f(\varepsilon, l, \varepsilon_\zeta)$ over the stellar velocities $\mathbf{v}$ yields the distribution of the coordinates $\mathbf{r}$ of the cluster stars. Comparison with the observed distribution of the radii r of stars in real clusters enables the determination of the parameters of the equilibrium phase-space density function. Once these parameters are known, the stellar-velocity distributions in the observed clusters can be determined by integrating $f(\varepsilon, l, \varepsilon_\zeta)$ over $\mathbf{r}$. The parameters of the equilibrium phase-space density function can also be used to estimate the total masses and other parameters of an OC using the coordinates and velocities of some of the cluster stars.

Let us now consider the estimates of τ_{x_i} obtained using the distributions $\nu^{(x_i)}(j)$, where x_i are the coordinates of the vector $\mathbf{x} = (\varepsilon, l, \varepsilon_\zeta, r, v), i = 1, ..., 5$. The errors in the τ_{x_i} values for $i = 1, ..., 5$ due to the dispersions of the corresponding means $\nu^{(x_i)}(j)$ from (7) are 1.5–4% (the dispersions of $\nu^{(x_i)}(j)$ are usually three to four orders of magnitude lower than the dispersions j computed using the distributions $\nu^{(x_i)}(j)$). The estimates of τ_{x_i} were obtained over the interval $\Delta t = 0.1\tau_{vr}$ and increase slowly with time (by factors of 1.5–1.7 over the time intervals considered). Table 2 lists the means of τ_{x_i} over the time intervals considered for the evolution of the OC models.

The standard deviations of τ_{x_i} about these mean values are usually ~8–15% of the mean, and are listed in Table 2. For τ_r and τ_v, Table 2 also gives the minimum and maximum τ_r and τ_v over the time interval considered (in parentheses in columns 9 and 10).

Thus, the rates of evolution and relaxation, $1/\tau_{x_i}$, $i = 1, ..., 5$, gradually decrease with time. Cluster models 1–5 satisfy the inequalities $\tau_\varepsilon > \tau_l > \tau_{\varepsilon_\zeta}$ and $\tau_r > \tau_v$ (in model 6, τ_ε and τ_l are indistinguishable within their errors). Star clusters with parameters for their core–halo structure that are close to the

corresponding initial parameters of model 6 are encountered fairly rarely among observed OCs (see the (ξ, μ) diagram for 103 OCs in [8]). In view of the results obtained here and in [1], the relations $\tau_\varepsilon > \tau_l > \tau_{\varepsilon_\zeta}$ and $\tau_r > \tau_v$ can be considered to be most characteristic of observed OCs.

The relaxation in the OC models proceeds most violently in ε_ζ and v. According to [1], the small values of τ_{ε_ζ} may be due to the fact that the initial compression in these cluster models is primarily along the ζ axis, and the frequency of the subsequent cluster oscillations is higher in the ζ direction than along the ξ and η directions. The small τ_v values are due to the broad wings of the $\nu^{(v)}(j)$ distribution.

Table 2 shows that $\tau_\varepsilon - \tau_{\varepsilon_\zeta}$ and $\tau_r - \tau_v$ decrease with the degree of nonstationarity of the OC. It is possible that the OC models develop barriers in their phase spaces [4, 5] that slow the diffusion of stars and that this has different effects on the rates of change of ε, l, ε_ζ, r, and v for these stars. It is likely that the number and impact of stochastic trajectories of the stellar motions increase in denser OC models with lower degrees of nonstationarity in their regular fields, decreasing the role of barriers in the phase spaces of such systems and ultimately leading to their disappearance [5]. In this case, the increase of $\tau_\varepsilon - \tau_{\varepsilon_\zeta}$ and $\tau_r - \tau_v$ with the degree of nonstationarity of the cluster models can be considered a manifestation of self-organization in such systems.

CONCLUSIONS

(1) Using a larger set of models, we have confirmed the conclusions of [1] that there is a balance of stellar fluxes in the spaces of $\varepsilon, l, \varepsilon_\zeta$, and r and that there exist equilibrium distributions of the stars in ε, l, and ε_ζ throughout the dynamical evolution of the clusters. The equilibrium phase-space density function corresponding to the balance of stellar fluxes in ε determines the structure of an open cluster during both violent relaxation and the subsequent "equilibrium" oscillations of the density. The parameters of the equilibrium phase-space density function of a gas- and dust-free cluster can be determined at any stage of its dynamical evolution. These parameters can be used to analyze the stellar-velocity distributions in such clusters and estimate the total masses and other dynamical parameters of open clusters.

(2) The stellar fluxes were used to estimate the relaxation times of the OC models in $\varepsilon, l, \varepsilon_\zeta, r$, and v. The estimated relaxation times usually satisfy the inequalities $\tau_\varepsilon > \tau_l > \tau_{\varepsilon_\zeta} > \tau_v$ and $\tau_r > \tau_v$. The relaxation times increase during the evolution of the clusters in all the parameter spaces considered. This behavior reflects a decrease in the rates of evolution in the $\varepsilon, l, \varepsilon_\zeta, r$, and v spaces after violent relaxation. The values of $\tau_\varepsilon - \tau_{\varepsilon_\zeta}$ and $\tau_r - \tau_v$ increase with the degree of nonstationarity of the models in the regular cluster field.

(3) We have estimated the local violent-relaxation times based on the instability of the phase-space density functions relative to small initial perturbations of the stellar phase-space coordinates and have found a relation between variations of the instability of the phase-space density function and differences between the relaxation rates of the cluster models in v and r. Our estimates of the violent-relaxation times $t_{r,c}^{(1)}$ for the cluster cores agree well with estimates of τ_v derived from the stellar fluxes in the cluster models. During violent relaxation, stars with energies ε occupy all domains of the cluster accessible to them, first in v and then in r.

(4) The OC models show a tendency for the ψ_i to decrease and the dependence of the coarse-grained phase-space density function on small initial perturbations of the stellar phase-space coordinates to weaken at $t > t_{r,c}^{(2)}$. We also found a similar trend in the halos of cluster models 1, 2, 5, and 6 at $t > t_{r,h}$.

(5) We have computed the coefficients of the grid functions (3) enabling integration of the stellar equations of motions using eighth- and ninth-order methods when using a fourth-order Runge–Kutta method in five- and six-grid computations.

ACKNOWLEDGMENTS

This work was partially supported by the Russian Foundation for Basic Research (project no. 00-02-16217).

REFERENCES

1. V. M. Danilov, Astron. Zh. **79**, 986 (2002) [Astron. Rep. **46**, 887 (2002)].
2. V. M. Danilov, Astron. Zh. **79**, 492 (2002) [Astron. Rep. **46**, 443 (2002)].
3. V. M. Danilov, Astron. Zh. **77**, 345 (2000) [Astron. Rep. **44**, 298 (2000)].
4. A. A. El-Zant, Astron. Astrophys. **326**, 113 (1997).
5. G. M. Zaslavskiĭ and R. Z. Sagdeev, *Introduction to Nonlinear Fhysics: From the Pendulum to Turbulence and Chaos* [in Russian] (Nauka, Moscow, 1988).
6. V. M. Danilov, Astron. Zh. **76**, 93 (1999) [Astron. Rep. **43**, 74 (1999)].
7. V. M. Danilov, Pis'ma Astron. Zh. **23**, 365 (1997) [Astron. Lett. **23**, 322 (1997)].

8. V. M. Danilov and A. F. Seleznev, Astron. Astrophys. Trans. **6**, 85 (1994).
9. S. Chandrasekhar, *Principles of Stellar Dynamics* (Chicago, 1942; Inostr. Lit., Moscow, 1948).
10. S. A. Kutuzov and L. P. Osipkov, Astron. Zh. **57**, 28 (1980) [Sov. Astron. **24**, 17 (1980)].
11. V. M. Danilov, Astron. Zh. **65**, 716 (1988) [Sov. Astron. **32**, 374 (1988)].
12. V. M. Danilov, Astron. Zh. **74**, 188 (1997) [Astron. Rep. **41**, 163 (1997)].
13. I. R. King, Astrophys. J. **67**, 471 (1962).
14. A. A. Samarskiĭ, *Introduction to Numerical Methods* [in Russian] (Nauka, Moscow, 1982).
15. A. F. Seleznev, Astron. Astrophys. Trans. **4**, 167 (1994).
16. P. N. Kholopov, *Star Clusters* [in Russian] (Nauka, Moscow, 1981).

Translated by A. Dambis

Astronomy Reports, Vol. 47, No. 6, 2003, pp. 492–497. Translated from Astronomicheskiĭ Zhurnal, Vol. 80, No. 6, 2003, pp. 535–541.

Observations and Optical Light-Curve Analysis for the Precataclysmic Variable BE Ursae Majoris

N. V. Raguzova[1], S. Yu. Shugarov[1], and N. A. Ketsaris[2]

[1]*Sternberg Astronomical Institute, Moscow State University, Universitetskiĭ pr. 13, Moscow, 119992 Russia*

[2]*Moscow State University, Vorob'evy Gory, Moscow, Russia*

Received November 10, 2002; in final form, November 27, 2002

Abstract—We have acquired three-color observations of BE UMa, a precataclysmic eclipsing variable with a strong reflection effect. Using new photoelectric UBV data and archival photographic observations, we have refined the orbital period and demonstrated that the eclipse depth changes with wavelength. The photometric data are used to compute a model for the system. Computations show that the nuclear evolution time for the secondary is only slightly less than the time for the separation of the components to change due to the loss of orbital angular momentum. Therefore, the red dwarf in the BE UMa system will later fill its Roche lobe because of (1) the decrease in component separation due to the loss of energy and angular momentum via gravitational-wave radiation or the outflow of a magnetic stellar wind and (2) the increase in the red dwarf's radius due to its nuclear evolution. © *2003 MAIK "Nauka/Interperiodica"*.

1. INTRODUCTION

Detached close binaries consisting of a white dwarf or its precursor and a low-mass, late-type main-sequence star are usually considered to be the immediate progenitors of cataclysmic variables. They are called precataclysmic binaries, and are believed to originate from very wide pairs with orbital periods of several years that have lost most of their initial angular momentum during the first mass transfer and a considerable part of their mass [1] during the common-envelope stage.

BE UMa is a star of this subtype. Since this object had not yet been studied in detail, we initiated new photometric observations of the star.

The variability of BE UMa was discovered by Kurochkin [2] in 1964 in photographic observations, which showed [3] sinusoidal brightness variations between $14\overset{m}{.}1$ and $15\overset{m}{.}6$ with a period of $\sim 2\overset{d}{.}29$. Initially, Kurochkin considered BE UMa to be a Cepheid variable. However, Green *et al.* [4] found that the star possessed a considerable ultraviolet excess and thus could not be a Cepheid.

Later studies demonstrated that BE UMa was a detached binary that had comparatively recently undergone a common-envelope stage. This is supported by the presence of a planetary nebula in the system, whose discovery is discussed in [5]. The primary is a very hot O subdwarf with a surface temperature of $\sim 100\,000$ K, whereas the secondary is a low-mass star of late spectral type (*M* or K).

Since the primary is extremely hot, its ultraviolet flux heats one side of the secondary, creating a hot spot on its surface [6]. This can give rise to a strong reflection effect in the system. It is the changing conditions for visibility of the spot that causes the sinusoidal brightness variations discovered by Kurochkin. In addition to the features of BE UMa described above, Ando *et al.* [6] observed a deep minimum with a duration of 72 min.

Since BE UMa is an eclipsing binary, its orbital plane is close to the observer's line of sight, enabling accurate determination of the component masses, as well as of other principal characteristics of the system, from the radial-velocity curve. Ando *et al.* [6] suggest a model for the system in which the very hot O subdwarf is eclipsed in the primary minimum by the cool *M* (or K) companion. Kurochkin and Shugarov [7] reduced all available photographic observations obtained in 1949–1982 and derived the refined orbital period $P_{\rm orb} = 2\overset{d}{.}291168$.

The common-envelope stage of this system was over $\sim 10^4$ years ago, so the secondary has not had time to return to thermal equilibrium. The recent results of Ferguson *et al.* [8] are of particular interest: they show that the radius of the secondary is $0.72R_\odot$, almost twice the radius of a main-sequence star with similar mass, $0.36M_\odot$. This means that, during the common-envelope stage, the lower-mass component was taken out of thermal equilibrium, significantly increasing its radius. The orbital period and semimajor axis of the BE UMa binary system are large

1063-7729/03/4706-0492$24.00

enough that the secondary does not fill its Roche lobe, and its shape can be taken to be spherical.

We acquired new three-color photoelectric observations of BE UMa and also reduced photographic observations obtained by us and at the Harvard Observatory [9] in order to

(1) refine the orbital period;

(2) perform an independent determination of the components' parameters.

2. REDUCTION OF OBSERVATIONS

We measured the star's brightness on 544 plates taken at the Crimean Laboratory of the Sternberg Astronomical Institute (SAI) with the 40 cm astrograph and the 50 cm Maksutov telescope. In addition, we carried out 121 measurements of the UBV brightness of BE UMa using the photoelectric photometer designed by I.M. Volkov, installed at the Cassegrain focus of the 60 cm or 125 cm reflector of the SAI Crimean Laboratory. The comparison star was star No. 1 (GSC 3454.00668; $11^{\rm h}58^{\rm m}13.960^{\rm s}$, $+48^\circ54'40''.03$, J2000; $V = 11^m.93$, $B - V = 0^m.49$, $U - B = -0^m.01$ [7]). All our photoelectric measurements are presented in the table.

We added our B-band observations to the new photoelectric data, the SAI photographic observations, and the Harvard photographic data of [9], which we reduced together with our observations. This yielded a series of observations spanning 100 years, enabling significant refinement of the orbital period. Our analysis gave the following light-curve elements:

$$HJD_{\rm min} = 47628.5381 + 2^{\rm d}.2911667E.$$

Our frequency analysis of the available data revealed no significant variations of the orbital period. The mean light curves plotted with our new elements are presented in Fig. 1.

The total amplitude of the light curve depends on the photometric band. For example, the total amplitude in the V and B bands is $\sim 3^m$, whereas the amplitude in the U band exceeds 4^m, as would be expected for eclipses of the very hot component, whose spectral maximum is in the far UV. This dependence proved to be helpful for improving estimates of the temperatures of the two components of the binary.

3. MODEL LIGHT CURVES

BE UMa displays a classic case of the reflection effect is an eclipsing binary. The super-hot star, which is the nucleus of the planetary nebula, heats the surface of the cool component facing it. The compact object, with a temperature of $1{-}2 \times 10^5$ K and its spectral maximum in the far ultraviolet, contributes insignificantly to the system's optical brightness. However, the spot it heats on the surface of the cool component has a central temperature of the order of 1.5×10^4 K, so that its maximum radiation is emitted at near ultraviolet and visible wavelengths. As is noted above, the changing visible area of the spot during the orbital motion of the normal star gives rise to the sinusoidal brightness variations observed for the system as a whole.

Since the system is detached, we neglected ellipsoidality effects and took both stars to be spherical. This enabled us to compute the mutual eclipses of the components analytically.

We synthesized the theoretical light curve using the following scheme.

(1) The surfaces of both stars were subdivided into $n \times n$ area elements, each radiating a Planck blackbody spectrum. The positions of the area elements on the stellar surface were described using the spherical coordinates of their centers η_j, ϑ_j relative to the star's center, which undergoes orbital motion with the period $P_{\rm orb}$. We assume that the centers of the stars move in circular orbits about their common center of mass.

(2) Let γ_j be the angle between the normal to a selected (jth) area and the line of sight. The area radiates the flux

$$F_j = B_\lambda(T_j)\,[1 - x(\lambda, T_j)\,(1 - \cos\gamma_j)]\cos\gamma_j dS_j, \quad (1)$$

in the direction of the observer at the wavelength λ, where $x(\lambda, T_j)$ is the linear darkening coefficient, T_j the area's temperature, and $B_\lambda(T_j) - 1$ the Planck function. We adopted the limb darkening coefficient for the optical component in accordance with [10].

(3) We take into account the reflection effect in the standard way [11]. Since the hot star's radius R_u is considerably smaller than the distance between the components, we can assume that the hard UV light is produced by a point source radiating isotropically. The temperatures of the areas on the normal star perturbed by the UV light from the hot companion are described by the formula

$$T(\eta_j, \vartheta_j) = \left[T_o^4 + T_u^4 \kappa \cos\gamma_u \left(\frac{R_u}{\rho_u}\right)^2\right]^{1/4}, \quad (2)$$

where γ_u is the angle between the normal to the area element with coordinates η_j, ϑ_j and the direction to the source, ρ_u is the distance from the area to the source (the center of the planetary nebula's nucleus), κ is the coefficient for reprocessing of the hard UV radiation by the optical star, T_o is the temperature of the normal star, and T_u is the temperature of the hot subdwarf.

Photoelectric observations of BE UMa

JD 2400000.0+	V	B	U	JD 2400000.0+	V	B	U
44989.622	15.66	15.45	14.20	47628.5381	17.30	17.94	
44989.648	15.45	15.44	14.21	47628.5385	17.21	17.71	16.04
44995.613	15.82	15.69	14.58	47628.5388	17.27	17.72	17.00
44995.629	15.91	15.72	14.50	47628.5398	17.06	17.51	
44995.649	16.09	15.71	14.70	47628.5402	17.43	17.77	16.82
45489.346	14.92	15.12	14.49	47628.5413	17.57	17.86	
45489.356	14.92	15.12	13.93	47628.5417	17.46	17.74	
45494.295	14.67	14.88	13.67	47628.5421	17.86	17.62	17.46
45494.304	14.66	14.82	13.62	47628.5429	17.18	17.34	18.10
45494.318	14.67	14.83	13.71	47628.5433	17.51	17.45	17.42
45494.326	14.67	14.82	13.68	47628.5437	17.59	17.62	18.27
45494.334	14.67	14.87	13.74	47628.5448	17.19	17.34	17.29
45494.344	14.65	14.85	13.83	47628.5466	17.33	17.17	16.71
45494.353	14.62	14.88	13.75	47628.5469	17.17	17.10	16.63
45494.362	14.67	14.85	13.65	47628.5473	16.62	17.50	16.16
45494.37	14.66	14.80	13.67	47628.5477	16.94	16.99	16.34
45494.377	14.65	14.79	13.69	47628.5483	17.03	17.38	16.29
45844.318	15.34	15.35	14.25	47628.5487	16.69	17.01	17.18
45847.331	14.65	14.93	13.70	47628.5492	16.96	16.96	16.35
45852.338	15.20	15.37	14.23	47628.5496	16.59	17.34	15.91
45854.313	14.87	14.90	13.74	47628.5508	16.65	16.84	15.57
45854.347	14.66	14.98	13.81	47628.5512	16.80	16.92	15.44
47628.5094	15.99	15.90	14.68	47628.5516	16.99	16.97	15.63
47628.5163	15.89			47628.552	16.89	16.65	15.71
47628.5165	15.87			47628.5524	16.72	16.80	15.79
47628.5166	16.10			47628.5527	16.62	16.59	15.56
47628.5168	15.96			47628.5531	16.57	16.43	15.71
47628.517	16.02	15.93	14.64	47628.5544	16.50	16.67	15.36
47628.5174	15.98	16.07	14.79	47628.5547	16.34	16.30	15.55
47628.5178	16.01	16.06	14.69	47628.5551	16.24	16.33	15.49
47628.5184	16.48	16.05	15.03	47628.5555	16.35	16.41	15.07
47628.5188	16.20	16.18	14.90	47628.5559	16.46	16.32	15.25
47628.519	16.09	16.09	14.75	47628.5563	16.18	16.29	15.22
47628.5201	16.23	16.16	14.97	47628.5565	16.26	16.15	15.12
47628.5209	16.07	16.26	15.25	47628.5569	16.16	16.06	15.12
47628.5213	16.16	16.29	14.97	47628.5573	16.15	16.24	15.03
47628.5228	16.22			47628.5577	16.19	16.05	14.85
47628.5237	16.33	16.58	15.39	47628.5584	16.04	16.04	15.15
47628.5241	16.31	16.70	15.48	47628.5588	16.14	16.08	14.87
47628.5245	16.12	16.82	15.83	47628.5592	15.96	16.01	14.84
47628.5249	16.33	16.92	15.24	47628.5596	15.98	15.94	14.99
47628.5256	16.37	16.88	15.48	47628.5603	16.13	15.91	14.90
47628.5261	16.41	16.93	15.74	47628.562	16.01		
47628.5265	16.51	16.91	15.52	47628.5623	15.99	15.92	14.72
47628.5269	16.65	17.22	16.00	47628.5627	15.89	15.80	14.71
47628.5273	16.49	17.03	16.30	47628.5631	16.04	15.98	14.81
47628.5279	16.65	17.12	16.29	47628.5638	16.08	15.96	14.97
47628.5286	16.54	17.24	15.75	49393.335	15.28	15.32	13.88
47628.529	16.69	17.44	15.72	49393.355	15.26	15.35	14.04
47628.5294	16.75	17.57	16.80	49393.428	15.02	15.16	13.96
47628.5298	16.73	17.37	15.97	49393.442	15.09	15.11	13.97
47628.5302	16.99	17.48	16.34	49393.468	14.97	15.07	13.94
47628.5306	16.90	17.45	16.19	49394.411	15.21	15.28	14.12
47628.5314	17.00	17.46	17.64	49394.424	15.20	15.30	14.15
47628.5318	17.06	17.56	16.34	49394.574	15.49	15.52	14.39
47628.5322	16.86	17.74	17.00	49394.586	15.52	15.54	14.37
47628.5331	16.96	17.80	16.34	49399.432	15.95	15.75	14.64
47628.5334	17.26	17.61	16.17	49400.451	14.87	14.95	13.77
47628.5352	17.13	17.87	17.32	49401.546	15.66	15.63	14.49
47628.5356	17.16	17.88		49403.573	15.22	15.28	14.19
47628.536	16.99	17.77	18.26				

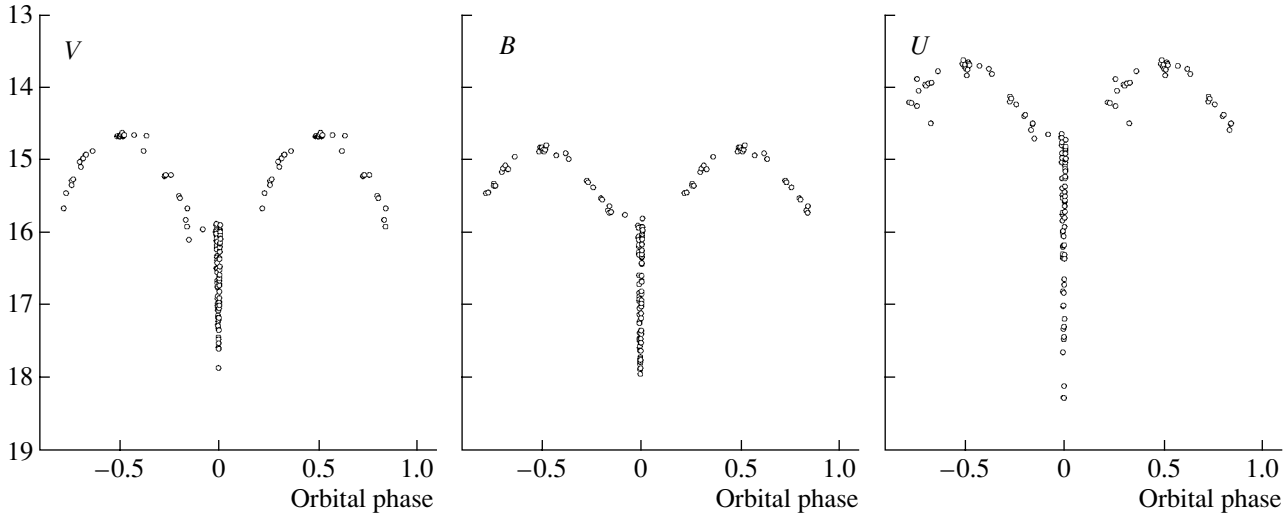

Fig. 1. UBV phase light curves of BE UMa plotted using the refined orbital period ($2^{d}.2911667$) and our photoelectric observations.

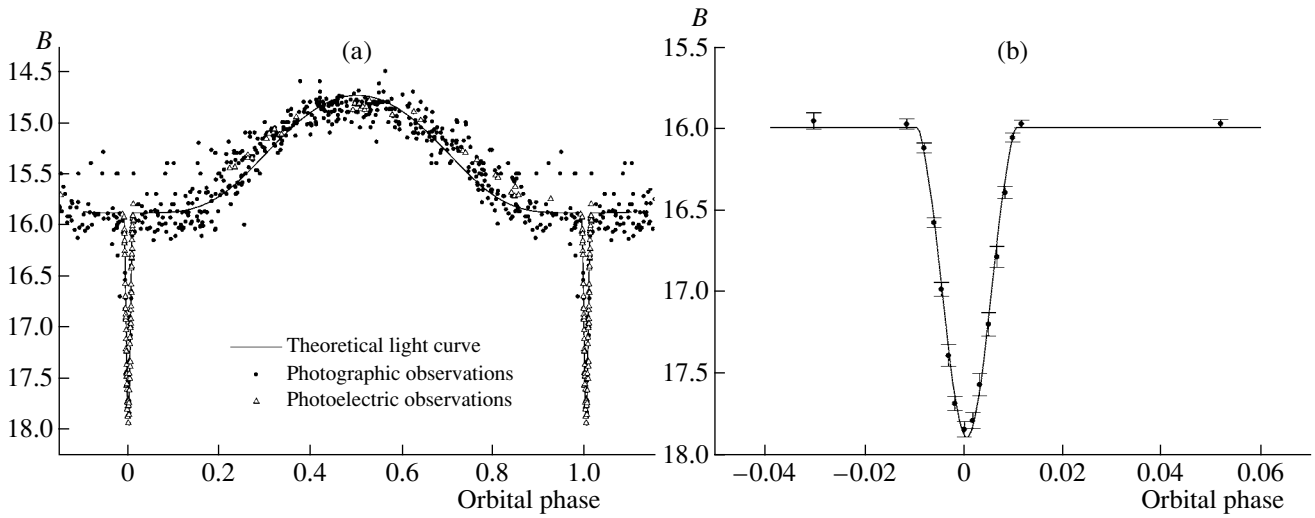

Fig. 2. Phase light curves of BE UMa plotted using the B photoelectric and photographic observations (a) for the entire orbital period and (b) data near the primary minimum. The solid curve is the light curve computed using the algorithm described in the text (cf. Section 3). The agreement between the observed and computed light curves is good.

(4) We use the sum of the fluxes emitted by all visible area elements on both stars to obtain their contribution to the total brightness:

$$F_{\rm sum} = \sum_{i=1}^{2} \sum_{\substack{j=1 \\ {\rm vis}_j={\rm true}}}^{nm} (F_j)_i, \qquad (3)$$

$$m = -2.5 \log \left(\frac{F_{sum}}{F_0} \right), \qquad (4)$$

where F_0 is the adopted normalization for the system's total light.

We used the χ^2 criterion

$$\chi^2 = \sum_{i=1}^{N_{obs}} \left(\frac{m_i^{synt} - m_i^{obs}}{\sigma_i} \right)^2 \qquad (5)$$

to estimate a model's significance, where m^{synt} and m^{obs} are the theoretical and observed magnitudes. When light curves were modeled simultaneously in several spectral bands, we summed the individual χ^2 values.

The minimization of χ^2 was carried out over five free parameters: i (orbital inclination), R_o, T_o, R_u, and T_u.

This yielded the following parameters for the BE UMa system:

$$i = 82\overset{\circ}{.}9 \pm 0\overset{\circ}{.}8,$$
$$R_u = 0.090 \pm 0.007 R_\odot,$$
$$T_u = (1.25 \pm 0.13) \times 10^5 \text{ K},$$
$$R_o = 1.18 \pm 0.10 R_\odot,$$
$$T_o = (5.40 \pm 0.45) \times 10^3 \text{ K},$$
$$T_\mathrm{s} = (1.5 \pm 0.1) \times 10^4 \text{ K},$$

where T_s is the central temperature of the spot on the surface of the normal component. In our computations, we took the distance between the components to be $7.5 \pm 0.5 R_\odot$ [8].

Plots of the computed and observed B light curves are shown in Fig. 2.

4. DISCUSSION AND CONCLUSIONS

We have refined the orbital period of BE UMa and constructed detailed UBV light curves of this system. We have also used numerical models to derive physical and geometrical characteristics of the components in the system.

The most interesting result of the modeling of the optical light curves is the very high ($\approx 1.25 \times 10^5$ K) temperature of the compact object. Several other similar binary systems are known; however, as a rule, their compact objects have significantly lower temperatures. For example, the central star of the planetary nebula in the binary V477 Lyr has a temperature of 4×10^4 K, and the temperature of the compact object in UU Sge is 5×10^4 K. Only the hot-dwarf planetary-nebula nucleus V664 Cas has a temperature as high as $(1.3\text{–}1.5) \times 10^5$ K.

Though no changes in the orbital period of the system have been detected, it is possible that such variations will be revealed by more precise observations. The system is detached, but the very high temperature of the primary may enable mass transfer via its stellar wind, leading to mass exchange in the system accompanied by changes in the period. This question can be answered by further, more detailed studies.

It is of considerable interest to consider the further evolution of BE UMa-type binaries. There are two possible paths for the evolution of a precataclysmic system from the detached to the semidetached stage, with one of the components reaching its Roche limit:

(1) the secondary's radius increases due to the star's nuclear evolution;

(2) the secondary's Roche lobe shrinks due to the loss of orbital angular momentum.

The secondaries of the vast majority of cataclysmic variables are main-sequence stars [12], so that the semidetached stage is achieved due to Roche lobe shrinking, i.e., via the second path. The mechanisms that can remove angular momentum from precataclysmic binaries are the same as those acting in cataclysmic variables: the emission of gravitational waves and the outflow of a magnetic stellar wind from the red dwarf [13, 14]. The first mechanism can operate in virtually any binary, independent of the internal structure of the components. The second mechanism is effective only under certain conditions [15], namely, that the secondary be magnetically active, have a high rate of (differential) rotation, possess a convective envelope, and have a mass exceeding $\sim 0.3 M_\odot$ (if the mass is lower, the whole star will be convective). The system must form a sufficiently close binary that the tidal interaction forces lead to almost synchronous rotation of the secondary.

The mass of the secondary in BE UMa is $0.36 \pm 0.07 M_\odot$, so that both mechanisms for the loss of orbital angular momentum can operate. To identify the correct scenario for the binary's further evolution, we must compare the time scale for changes in the separation of the components due to gravitational-wave radiation (and/or the outflow of magnetic stellar wind from the red dwarf) to the nuclear-evolution time scale for the secondary (t_{ev}). The time after which a BE UMa-like binary reaches the semidetached stage due to the loss of angular momentum via gravitational radiation can be computed using the formula [15]

$$t_{sd}^{GR} = 4.73 \times 10^{10} \left(\frac{M_1 + M_2}{M_\odot}\right)^{1/3} \left(\frac{M_1}{M_\odot}\right)^{-1} \times \left(\frac{M_2}{M_\odot}\right)^{-1} P_\mathrm{orb}^{8/3} (1 - (P_{sd}/P_\mathrm{orb})^{8/3}) \text{ years}, \quad (6)$$

where

$$P_{sd} = 9\pi \left(\frac{R_2^3}{2GM_2}\right)^{1/2} \quad (7)$$

is the orbital period of a semidetached system whose components have analogous parameters (all the periods are expressed in days). The time needed to reach the semidetached stage via the outflow of a magnetic stellar wind is given by the formula [15]

$$t_{sd}^{MW} = 1.6 \times 10^7 f \left(\frac{r_{g2}^2}{0.1}\right)^{-1} \frac{q}{(1+q)1/3} \times \left(\frac{R_2}{R_\odot}\right) \left(\frac{M_2}{M_\odot}\right) \left(\left(\frac{P_\mathrm{orb}}{P_{sd}}\right)^{10/3} - 1\right) \text{ years}, \quad (8)$$

where R_2 is the secondary's radius, r_{g2} its radius of gyration, and f a parameter of the order of unity. For

a BE UMa-type system, we obtain

$$t_{sd}^{GR} = 1.7 \times 10^{12} \text{ years},$$
$$t_{sd}^{MW} = 3.5 \times 10^{12} \text{ years},$$
$$t_{ev} = 6.1 \times 10^{11} \text{ years}.$$

According to the recent results of Ferguson *et al.* [8], the radius of the secondary in BE UMa is almost twice the radius of a main-sequence star with the same mass, $0.36M_\odot$. The age of the planetary nebula in the system is estimated to be $\sim 10^4$ years [5]. It is obvious that this time is insufficient for the secondary to have reached thermal equilibrium and shrink to its normal radius (corresponding to a main-sequence star). When computing time scales, we considered the equilibrium radius of the secondary, $0.37R_\odot$, since it is reached on a time scale $t_{KH} \sim 10^7$, where t_{KH} is the thermal Kelvin–Helmholtz time scale for the red dwarf to reach thermal equilibrium, which is much shorter than the above values for t_{sd}^{GR}, t_{sd}^{MW}, and t_{ev}.

These calculations indicate that the time scale for nuclear evolution of the secondary exceeds the time scale for changes in the separation of the components due to the loss of orbital angular momentum by less than an order of magnitude. Given the uncertainty in the mass of the secondary, these time scales could be comparable. We conclude that the future Roche lobe filling by the red dwarf in the BE UMa system will be the result of two factors: (1) the decrease in the component separation (decrease in the absolute dimensions of the Roche lobe) due to the loss of energy and angular momentum via the radiation of gravitational waves and/or the outflow of a magnetic stellar wind and (2) the increase in the radius of the red dwarf due to its nuclear evolution. Note that the time required for this system to become semidetached exceeds the Hubble time; thus, systems similar to BE UMa whose secondaries fill their Roche lobes should not be observed, since they have not had time to evolve to this stage.

ACKNOWLEDGMENTS

The authors are grateful to N.I. Shakura, A.V. Tutukov, and S.V. Antipin for helpful discussions and comments. This work was partially supported by the Russian Foundation for Basic Research (project nos. 00-02-17164, 00-15-96533, and 02-02-17524) and by the "Universities of Russia" program (grant no. 5558).

REFERENCES

1. H. Ritter, Mon. Not. R. Astron. Soc. **175**, 279 (1976).
2. N. E. Kurochkin, Perem. Zvezdy **15**, 77 (1964).
3. N. E. Kurochkin, Perem. Zvezdy **18**, 85 (1971).
4. R. F. Green, M. Schmidt, and J. Liebert, Astrophys. J., Suppl. Ser. **61**, 305 (1986).
5. J. Liebert, R. Tweedy, R. Napiwotzki, *et al.*, Astrophys. J. **441**, 424 (1995).
6. H. Ando, A. Okazaki, and Sh. Nishimura, Publ. Astron. Soc. Pac. **34**, 141 (1982).
7. N. E. Kurochkin and S. Yu. Shugarov, Astron. Tsirk. **1216**, 3 (1982).
8. D. H. Ferguson, J. Liebert, S. Haas, *et al.*, Astrophys. J. **518**, 866 (1999).
9. D. H. Ferguson, J. Liebert, R. Cutri, *et al.*, Astrophys. J. **316**, 399 (1987).
10. H. M. Al-Naimiy, Astrophys. Space Sci. **53**, 181 (1978).
11. E. A. Antokhina, Astron. Zh. **65**, 1164 (1988) [Sov. Astron. **32**, 608 (1988)].
12. A. M. Cherepashchuk, N. A. Katysheva, T. S. Khruzina, and S. Yu. Shugarov, *Highly Evolved Close Binary Stars* (Gordon and Breach, Amsterdam, 1996).
13. I. Iben, Jr. and A. V. Tutukov, Astrophys. J. **284**, 719 (1984).
14. I. Iben, Jr. and A. V. Tutukov, Astrophys. J., Suppl. Ser. **54**, 335 (1984).
15. H. Ritter, Astron. Astrophys. **169**, 139 (1986).

Translated by N. Samus'

Astronomy Reports, Vol. 47, No. 6, 2003, pp. 498–510. Translated from Astronomicheskiĭ Zhurnal, Vol. 80, No. 6, 2003, pp. 542–555.

Calculation of Profiles of CIV, NV, OVI, and SiIV Resonance Lines Formed in Accretion Shocks in T Tauri Stars: A Plane Layer

S. A. Lamzin

Sternberg Astronomical Institute, Universitetskiĭ pr. 13, Moscow, 119992 Russia

Received November 15, 2002; in final form, January 10, 2003

Abstract—We have calculated profiles of the CIV 1550, NV 1240, OVI 1035, and SiIV 1400 resonance doublets for a plane-parallel shock viewed at various angles. Calculations were performed for the range of preshock gas velocities V_0 and gas densities ρ_0 appropriate for classical T Tauri stars. The parameters of accretion shocks in young stars can be determined by comparing the calculated and observed profiles of the studied lines and their relative intensities. It is not possible to derive the parameters of the accreting gas from the line profiles without knowing the geometry of the accretion zone. The relation $I_\nu(\mu, V_0, \rho_0)$ for a plane shock, where I_ν is the intensity $\mu = \cos\theta$, can be used to determine the accretion parameters by either choosing a geometry for the radiating region or using a technique similar to Doppler tomography. The results obtained for DR Tau, T Tau, and RY Tau indicate that, in contrast to current concepts, the inner regions of the accretion disk are not disrupted by the magnetic field of the star, and the disk reaches the stellar surface. As a result, only a small fraction of the accreted matter passes through the shock and falls onto the star. © *2003 MAIK "Nauka/Interperiodica"*.

1. INTRODUCTION

Since the beginning of the 1990s, there has been a consensus that the line and continuum emission observed in the spectra of classical T Tauri stars results from the magnetospheric accretion of circumstellar material. More precisely, the magnetic field of the star is believed to stop the accretion disk from reaching the stellar surface. In one way or another, the disk material becomes frozen in the magnetic field and slides along the field lines toward the stellar surface, eventually being accelerated to velocities ~ 300 km/s. The gas is decelerated in an accretion shock, whose radiation gives rise to the observed line and continuum emission.

According to [1], the radiating region of the accretion shock should be much smaller than the radius of the young star, making it possible to calculate the structure and spectrum of the accretion shock in a one-dimensional approximation [2, 3]. The calculations indicated that the structure of the flow can be specified nearly unambiguously by two parameters: the velocity V_0 and density ρ_0 of the gas far in front of the shock. Following [2], along with the density (in g/cm^3), we will use the number of nuclei of all elements per unit volume located far in front of the shock, N_0 (in cm^{-3}). Since we assume standard abundances for the elements, $\rho_0 = 2.17 \times 10^{-24} N_0$.

The results of the calculations [3] were used to derive the parameters of the accretion shock via modeling of the continuum spectral energy distributions of classical T Tauri stars: V_0, ρ_0, the accretion rate, and the area occupied by the shock. However, agreement between the calculated and observed spectra of the veiling continuum cannot be considered as a decisive support for the magnetospheric model, since boundary-layer models provide equally good agreement (see, for example, [4]). The line spectrum is far more informative, and comparisons of the calculated and observed intensities and profiles of emission lines enable detailed studies of the accretion processes.

Optically thin lines are best suited for this purpose: their intensity ratios can be used to derive physical conditions independent of the geometry of the region where they are formed, and the line profiles provide information about both the velocity field and geometry of this region. The calculations of [2] show that the OIII 1663, SiIII 1892, and CIII 1909 intercombination lines should display the highest intensities among the optically thin lines, and precisely these lines were used to determine the accretion-shock parameters for several young stars [5, 6]. However, Gómez de Castro and Verdugo [7] questioned whether these lines form in the accretion shock, while Kravtsova and Lamzin [8] showed that, in the case of DR Tau, most of the flux in these lines is formed in the inner regions of the accretion disk. In addition, there are reasons to believe that the helium lines observed in the optical spectra of classical T Tauri stars are also formed largely outside the accretion shock [9] and thus likewise cannot be used for diagnostics of the shock parameters.

1063-7729/03/4706-0498$24.00

In this connection, the resonance lines of the CIV, NV, and OVI lithium-like doublets and the sodium-like SiIV ion are the most promising lines for studies of the accretion-shock parameters. These lines have high intensities in the spectra of classical T Tauri stars, and their profiles are consistent with the hypothesis that they are formed in the accretion shock. This is also in agreement with the results of [2], which, in particular, predict that the luminosity in the CIV 1550 lines should be several percent of the bolometric luminosity of the accretion shock.

These lithium- and sodium-like ions display the following term structure. Two levels of the $^2P^0$ term are situated directly above the $^2S_{1/2}$ ground level; the $J = 1/2$ level lies below the $J = 3/2$ level. The excitation potential of the ^2P term is appreciably lower than the excitation potentials of both the ion and the nearest higher level. In the problem at hand, this means that these ions can be treated as three-level systems, with the levels numbered in order of increasing excitation energy: level 1 is $^2S_{1/2}$, level 2 is $^2P^0_{1/2}$, and level 3 is $^2P^0_{3/2}$. The statistical weights $g = 2J + 1$ for these levels are $g_1 = 2$, $g_2 = 2$, and $g_3 = 4$. The transitions $2 \to 1$ and $3 \to 1$ generate the line doublets that we will study, while transitions between fine-structure levels of the $^2P^0$ term, i.e., $3 \to 2$, are strongly forbidden by the selection rules.

Table 1 presents the wavelengths, excitation potentials for the upper level E_k ($k = 2, 3$), spontaneous-transition probabilities A_{k1}, and oscillator strengths f_{1k} for these lines from the database *http://physics.nist.gov*. The two last columns contain parameters characterizing the collisional broadening of the lines. These are the same for both lines of the doublet and were taken from [10–13]; see below for details. For completeness, we note also the atomic weights A for carbon, nitrogen, oxygen, and silicon: 12, 14, 16, and 28, respectively.

According to [2], these resonance lines should display substantial optical depths. Therefore, their profiles and relative intensities in the case of a plane-parallel shock should depend on the inclination of the plane of the shock front to the line of sight θ, and, in the case of an accretion shock, on the geometry of the accretion zone and its orientation relative to the observer, which, in particular, can vary in the course of the axial rotation of the star.

It means that, in order to diagnose the accretion shocks in young stars using the CIV 1550, NV 1240, OVI 1035, and SiIV 1400 doublet lines, it is not sufficient to know the intensities radiated in these lines from a unit area of the shock front normal to the front, which were found in [2]. We must also calculate the dependence of the intensities and line profiles on the angle θ for the case of a one-dimensional shock,

Table 1. Parameters of the studied lines

Ion	λ, Å	E_k, eV	A_{k1}, $10^8\ s^{-1}$	f_{1k}	T_P, 10^4 K	W_P, 10^{-3} Å
CIV	1548.19	8.008	2.65	0.190	2	11.5
	1550.77	7.995	2.64	0.095		
NV	1238.82	10.008	3.40	0.156	5	3.58
	1242.80	9.976	3.37	0.078		
OVI	1031.91	12.015	4.16	0.133	10	1.46
	1037.61	11.949	4.09	0.066		
SiIV	1393.76	8.896	7.73	0.450	2	17.6
	1402.77	8.839	7.58	0.224		

and then use this information to calculate these corresponding values for various accretion-zone geometries. Here, we solve the first part of this problem: calculation of the line profiles for the case of a plane-parallel shock. Our analysis will be based on the calculations of [2], where we derived the distributions of the density and temperature of the gas and of the abundances of the corresponding ions perpendicular to the front of a one-dimensional shock for various values of V_0 and ρ_0.

2. FORMULATION OF THE PROBLEM

Let us write equations describing the radiative transfer in a plane-parallel layer of gas in the situation considered, following [14–16]. Let z be the current coordinate measured from the upper boundary of the layer perpendicular to this layer and $\tau_{1k}(z)$ be the characteristic optical depth in the $1 \leftrightarrow k$ ($k = 2, 3$) transition, also measured from the upper boundary. We can write

$$\frac{\mathrm{d}\tau_{1k}}{\mathrm{d}z} = \frac{\pi e^2 f_{1k}}{m_e c \Delta\nu_D}\left(N_1 - \frac{g_1}{g_k}N_k\right). \qquad (1)$$

Here, N_1 and N_k are the numbers of ions per unit volume in the ground and excited states and $\Delta\nu_D$ is the Doppler half-width of the line, which is related to the thermal velocity of the ions V_t by the expression

$$\Delta\nu_D = \frac{\nu_0}{c}V_t, \qquad V_t = \sqrt{\frac{2\Re T_i}{A}},$$

where $\Re = 8.31 \times 10^7$ erg g^{-1}K^{-1} is the universal gas constant and T_i is the temperature of the ion component of the gas. If the gradient of the velocity associated with the macroscopic motion in the layer is zero, τ_{1k} is $\sqrt{\pi}$ times the optical depth at the line center.

In [2], the structure of the shock was considered in a two-temperature approximation in which it was

Table 2

V_0, km/s	$\log N_0$ (cm^{-3})	Z_{pst}, cm	τ_{pst}			
			CIV	NV	OVI	SiIV
200	11	$1.6336+7$	4.34	0.99	13.1	1.10
	12	$1.7787+6$	4.36	1.00	13.6	1.10
300	11	$7.1064+7$	4.10	0.70	8.80	1.06
	12	$7.1920+6$	4.10	0.71	9.05	1.06
400	11	$1.2980+8$	5.19	0.70	6.99	1.47
	12	$1.3018+7$	5.23	0.71	7.16	1.49

assumed that the atoms and ions have the same temperature T_i, which, in general, differs from the temperature of the electron gas T_e. It turned out, however, that T_i and T_e differ appreciably only in a relatively thin layer behind the accretion shock. It can be shown that, in this region, the rates of ionization and excitation by electron collisions depend on $T_e^{eff} = T_e + m_e/m_i T_i$, where m_e and m_i are the masses of the electron and ion, rather than on the electron temperature. In the case considered here, however, the difference between T_e^{eff} and T_e does not exceed a few percent, and we will assume that the rates of these processes are specified by T_e.

In our case, the lines corresponding to the $2 \leftrightarrow 1$ and $3 \leftrightarrow 1$ transitions do not overlap; therefore, neglecting absorption in the continuum and assuming total frequency redistribution, the radiative-transfer equation for each line can be written

$$\mu \frac{\mathrm{d}I_{1k}}{\mathrm{d}\tau_{1k}} = \phi_{1k}\left(S_k - I_{1k}\right), \qquad (2)$$

where $\mu = \cos\theta$, $I_{1k}(\nu, \tau_{1k}, \mu)$ is the intensity of the line radiation at frequency ν at an angle θ to the normal at the optical depth τ_{1k}, and $\phi_{1k}(\nu, \tau_{1k})$ is the Voigt profile for the absorption (and radiation) coefficient normalized to the variable $x = (\nu - \nu_0)/\Delta\nu_D$, i.e.,

$$\phi(a,x) = \frac{a}{\pi^{3/2}} \int\limits_{-\infty}^{\infty} \frac{\exp(-y^2)}{(x-y)^2 + a^2}\mathrm{d}y,$$

$$\int\limits_{-\infty}^{\infty} \phi(a,x)\mathrm{d}x = 1.$$

In addition to the variable x, we will use the values

$$\Delta\lambda_D = \frac{\lambda_0}{\nu_0}\Delta\nu_D, \qquad a = \frac{W_P}{2\Delta\lambda_D},$$

where $W_P = W_P(T_e, N_e)$ is the full width at half maximum (FWHM) of the profile $\phi(\nu_*)$ due to collisions of the radiating atoms with the surrounding particles. The values of W_P presented in Table 1 are for the case when $N_e = 10^{17}$ cm^{-3} and $T_e = T_P$; T_P is also given in Table 1. According to [17], if, as in our case, $\log N_e < 17$,

$$W_P(T, N_e) = W_P^0 \sqrt{\frac{T_P}{T_e}}\frac{N_e}{10^{17}},$$

where W_P^0 is taken from Table 1.

We denote the source function $S_k(\tau_{1k})$ in (2):

$$S_k = \frac{2h\nu_{1k}^3}{c^2}\frac{N_k g_1}{N_1 g_k - N_k g_1}. \qquad (3)$$

Let us assume that the population of the excited levels is small, i.e., $N_k/N_1 \ll 1$. Equations (1) and (3) will then take the form

$$\frac{\mathrm{d}\tau_{1k}}{\mathrm{d}z} = \frac{\pi e^2 f_{1k}}{m_e c \Delta\nu_D} N_1, \qquad (4)$$

$$S_k = \frac{2h\nu_{1k}^3}{c^2}\frac{g_1 N_k}{g_k N_1}. \qquad (5)$$

Let q_{ik} and q_{ki} be the coefficients of electron collisional excitation and deexcitation for the $i \leftrightarrow k$ transitions. They are related by the expression

$$q_{ik} = q_{ki}\frac{g_k}{g_i}\exp\left(-\frac{h\nu_{ik}}{kT_e}\right),$$

with

$$q_{ki} = \frac{8.63 \times 10^{-6}}{g_k\sqrt{T_e}}\Upsilon_{ik},$$

where Υ_{ik} is the collisional strength, which depends only weakly on T_e. The Υ_{1k} values for the studied lines were taken from the CHIANTI database [18].

Let us also denote the intensity of the line radiation for the $1 \leftrightarrow 3$ transition averaged in angle $J_{13}(\nu, \tau_{13})$:

$$J_{13} = \frac{1}{4\pi}\int\limits_0^{4\pi} I_{13}\mathrm{d}\Omega = \frac{1}{2}\int\limits_{-1}^{1} I_{13}\mathrm{d}\mu.$$

Since radiative transitions between levels 2 and 3 are strongly forbidden, the condition of stationarity for the third level can be written

$$N_3\left[A_{31} + N_e\left(q_{31} + q_{32}\right)\right] \qquad (6a)$$
$$= N_1\left(B_{13}\bar{J}_{13} + N_e q_{13}\right) + N_2 N_e q_{23},$$

where N_e is the electron density, A_{31} and B_{13} are the Einstein coefficients, and

$$\bar{J}_{13}(\tau_{13}) = \int\limits_0^{\infty} J_{13}\phi_{13}(\nu)\mathrm{d}\nu.$$

By neglecting radiative transitions between the fine structure levels of the ^{2}P term in (6a), we are assuming that the relative populations of the excited levels are specified by collisions; i.e., $N_e N_2 q_{23} = N_e N_3 q_{32}$. Then

$$\frac{N_3}{N_2} = \frac{g_3}{g_2} \exp\left(-\frac{h\nu_{23}}{kT_e}\right) \simeq \frac{g_3}{g_2} = 2, \qquad (7)$$

since $h\nu_{23} < 0.04$ eV and $kT_e > 1.5$ eV for all ions in the regions of interest to us. Further, this makes it possible to eliminate N_2 from (6a), so that

$$\frac{N_3}{N_1} = \frac{B_{13}\bar{J}_{13} + N_e q_{13}}{A_{31} + N_e q_{31}}. \qquad (6b)$$

If we introduce the critical density $N_e^c = A_{31}/q_{31}$, then, using the relation between B_{13} and A_{31}, the source function for the $1 \leftrightarrow 3$ transition can be written

$$S_3 = (1-\varepsilon)\bar{J}_{13} + \varepsilon B_{13}, \qquad (8)$$

where $\varepsilon = N_e/(N_e + N_e^c)$, and

$$B_{13} = \frac{2h\nu_{13}^3}{s^2} \exp\left(-\frac{h\nu_{13}}{kT_e}\right)$$

is the Planck function in the Wien approximation.

The z distributions of the density, temperature, and abundances of all the ions are known from the solution for the structure of the one-dimension shock; the dependences of these values on τ_{13} can be found using (4). According to (8), the source function S_3 does not depend on the population of the second level. This makes it possible to solve for the radiative transfer in the line corresponding to the $1 \leftrightarrow 3$ transition independently, without considering the radiative transfer in the line corresponding to the $1 \leftrightarrow 2$ transition. The problem can then also be solved for the second line of the doublet, since

$$S_2(\tau_{12}) = S_3(\tau_{13})\left(\frac{\nu_{12}}{\nu_{13}}\right)^3, \quad \tau_{13} = 2\tau_{12}. \qquad (9)$$

These relations follow from (4), (5) and (7), taking into account the fact that $f_{13}/f_{12} \simeq 2$.

In this way, we are able to reduce the calculation of the profiles of the CIV, NV, OVI, and SiIV doublets to the solution of the problem for the $1 \leftrightarrow 3$ transition, for example. Further, we will consider only this transition; therefore, we will omit the index "1k," denote ν_0 to be the frequency at the line center, and write B_0 in place of $B_{13}(\nu_0)$. Although the initial problem has been reduced to the case of radiative transfer in a two-level atom, the expression for the source function (8) differs somewhat from the corresponding general expressions; see, for example, (11.6)–(11.8) in [16]. This is due to our *a priori* hypothesis that the ratio N_3/N_1 is small. Jumping ahead, we can say that, in the calculated models, the ratio N_k/N_1 turned out to be smaller than 0.01, which *a posteriori* justifies the initial assumption.

Below, we will show that we must first determine the intensity of the radiation from regions behind the accretion-shock front. We can then use the results as a boundary condition for the region in front of the shock.

3. THE REGION BEHIND THE ACCRETION-SHOCK FRONT

Table 2 presents the extent of the region behind the shock front (the post-shock region) and the optical depth of the studied lines $\tau_{pst} \equiv \tau_{13}$ perpendicular to the front for various V_0 and N_0. The value of τ_{pst} was obtained via numerical integration of (1), and takes into account, in particular, variations in the thermal velocity of the ions in the layer, associated with variations in the gas temperature. Due to the factor $\phi(x)$, which should also take into account the velocity gradient in the cooling gas [see (10) below], the real optical depth of the lines in this direction should be substantially smaller than the value in Table 2: calculations indicate that, in all cases, it is either smaller than or only slightly greater than unity. For example, in the case of the OVI ion lines for $V = 300$ km/s, the effective optical depth at the line center is $\simeq 2$, a factor of four smaller than the corresponding value from Table 2.

This suggests that photoexcitation does not play a significant role behind the shock front. Of course, as $\theta \to \pi/2$, the optical depth of the layer τ_{pst}/μ ceases to be significant. However, the contribution from one section of the accretion zone to the total radiation flux is proportional to the cosine of the angle at which it is viewed [see (17) below]; therefore, the contribution to the accretion-shock radiation from regions with $\mu \simeq 0$ is small. Based on this, we will not take photoexcitation into account for all μ values; however, the effect of the flux decrease due to self-absorption will be included. This approach simplifies the problem dramatically, making it possible to calculate line profiles in the region behind the shock front while neglecting the radiation from regions in front of the shock.

Behind the shock front, the gas velocity V becomes smaller than the sound speed, and decreases from $V_0/4$ to nearly zero as the gas cools. Therefore, due to the Doppler effect, the frequency of a photon ν measured by an external observer is related to the frequency ν_* in the rest frame of the moving gas by the expression

$$\nu_* = \nu\left(1 + \frac{V\mu}{c}\right).$$

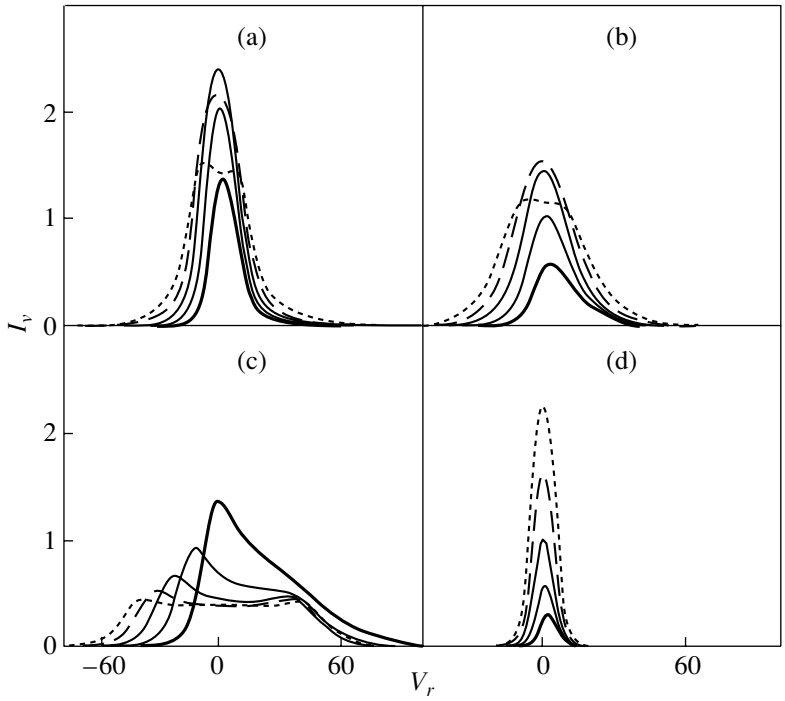

Fig. 1. (a) CIV 1548, (b) NV 1239, (c) OVI 1032, and (d) SiIV 1394 line profiles at the outer boundary of the region behind the accretion-shock front for $V_0 = 250$ km/s and $\log N_0 = 12$. The vertical axis shows the intensities in units of 10^{-4} erg s^{-1}cm^{-2}sr^{-1} Hz^{-1} and the horizontal axis plots the radial velocity in km/s. The various curves represent profiles for different values of μ: the solid curves of decreasing thickness correspond to the values 1.0, 0.5, and 0.25, the dashed curve to 0.125, and the dot–dash curve to 0.0625.

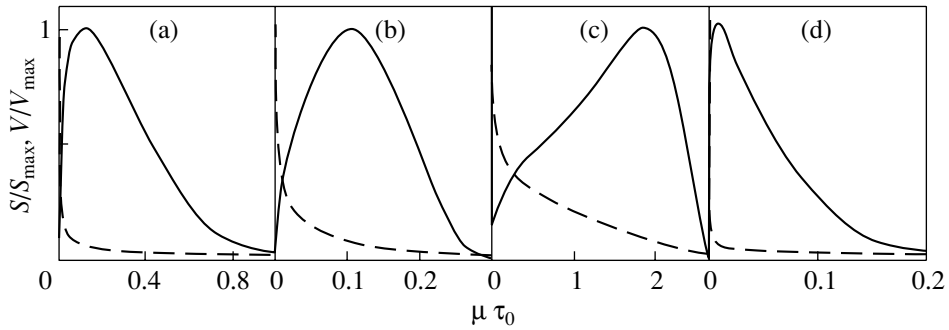

Fig. 2. Source functions for the (a) CIV 1548, (b) NV 1239, (c) OVI 1032, and (d) SiIV 1394 lines normalized to the maximum (solid curves) and the gas velocity (dashed curves) in the region behind the accretion-shock front for $V_0 = 250$ km/s and $\log N_0 = 12$.

For convenience in comparing the calculated and observed profiles, we will use $v = c(\nu_0 - \nu)/\nu_0$ rather than the frequency as the independent variable. Neglecting terms of order V/c, we obtain

$$|x| = \frac{|v - V\mu|}{V_t}, \qquad (10)$$

$$\phi_v \equiv \phi(x) = \phi\left(\frac{|v - V\mu|}{V_t}\right).$$

We know the z dependence of V_t and V from the calculations of the shock structure, so that we can find the $V_t(\tau)$ and $V(\tau)$ dependences using (1). Thus, ϕ_v is a known function of τ.

From the mathematical point of view, the possibility of neglecting photoexcitation means that the first term in (8) is equal to zero, i.e., $S_3 = \varepsilon B_0$. It then follows from (2) that the intensity of the outgoing

$(0 < \mu \leq 1)$ radiation is

$$I_v(0,\mu) = \int_0^{\tau_{pst}} \phi_v(\tau)\varepsilon(\tau)B_0(\tau) \times \exp\left(-\int_0^{\tau} \phi_v(t)\frac{\mathrm{d}t}{\mu}\right)\frac{\mathrm{d}\tau}{\mu}. \quad (11)$$

Figure 1 presents the results of the calculation of the line profiles for the $3 \leftrightarrow 1$ transitions of the C^{+3}, N^{+4}, O^{+5}, and Si^{+3} ions with $V_0 = 250$ km/s, $\log N_0 = 12$, and various μ values. Let us clarify why the profiles and their variations with μ display this behavior.

Figure 2 presents the source functions of the lines as functions of the optical depth τ_0 at the central frequency—i.e., for $v = 0$—for the given values of V_0 and N_0. When calculating τ_0, we took into account the velocity gradient in the layer using (10). The plots are given for $\mu = 1$; however, since S does not depend on the angle, the corresponding curves will only be stretched along the x axis by a factor of $1/\mu$ for other values of the angular variable. In Fig. 2, we have plotted $\mu\tau_0$ along the horizontal axis, so that the shape of the curves is independent of μ. The dashed curve shows the variations of the gas velocity behind the accretion-shock front from its maximum value $V_{\max} \simeq V_0/4 \simeq 63$ km/s to essentially zero. We can see that the line optical depths build up away from the front, more precisely, in the zone where the corresponding ionization stage of the given element dominates, where the gas velocity is relatively small.

The value of τ_0^{pst} for the CIV, NV, and SiIV ion lines for $\mu = 1$ is appreciably smaller than unity; i.e., these lines are optically thin. As μ becomes smaller, the optical depth of these lines along the line of sight grows, so that their central intensity also increases as μ decreases. This continues as long as τ_0/μ remains smaller than unity. With further decrease in μ, the gas becomes optically thick, and the largest contribution at the central intensity is made by regions of the accretion shock for which $\tau_0/\mu \sim 1$. As long as these regions lie to the right of the source function's maximum (Fig. 2), as before, decreases in μ will be accompanied by increases in the central intensity: as θ increases, the observer sees regions of more intense radiation. However, starting from some μ_c, as θ increases further, regions with $\tau_0/\mu \sim 1$ will correspond to smaller and smaller values of the source function, so that, when $\mu < \mu_c$, the central intensity of the line will begin to decrease.

The different behavior for the central intensities of the CIV, NV, and SiIV ion lines is due to differences in the values of τ_0^{pst} and μ_c. The OVI 1032 line is already optically thick when $\mu = 1$; in addition, as follows from Fig. 2, the region with $\tau_0/\mu \sim 1$ for this line lies to the left of the maximum of $S(\tau_0/\mu)$ for all μ. In accordance with the above discussion, this results in a monotonic decrease in the central line intensity with decreasing μ in Fig. 1.

All the above arguments remain qualitatively valid if we consider any other point of the profile with $v \neq 0$ instead of the central frequency. When performing quantitative analyses, we must take into account the fact that, for the same μ values, the optical depth of a layer will differ from τ_0^{pst}/μ due to the factor ϕ_v. If the gas behind the accretion-shock front was stationary, the line profiles would be symmetrical ($I_v = I_{-v}$), and the optical depth of a layer for a given μ would decrease with increasing $|v|$. Because of this, the FWHM of the lines would increase as μ decreases, and, at some time, their profiles would display two peaks.

The motion of the gas behind the accretion-shock front preserves this behavior, but the lines become asymmetrical, since, in accordance with (10), the absorption coefficient reaches its maximum when $v = V\mu$ rather than at the line center. For this reason, at small (large) optical depths, the line intensity displays the most rapid increase (decrease) at the point in the profile where $v = V\mu$, rather than at $v = 0$. Finally, since the velocity gradient in the region of line formation is not very high, the line center shifts monotonically toward $v = 0$ as μ decreases, and the lines become increasingly symmetrical.

For other velocities and densities of the falling gas in the intervals 200 km/s $\leq V_0 \leq$ 400 km/s and $11 \leq \log N_0 < 13$, the profiles of the lines originating behind the accretion-shock front vary only quantitatively: for example, for $V_0 = 400$ km/s and $\log N_0 = 12$, the lines look broader and have intensities that are about twice as high.

4. THE REGION IN FRONT OF THE ACCRETION SHOCK

According to [2], the gas velocity varies little in front of the shock, by only 2–3%. The drop in the velocity at a distance of Δz is on the order of the mean free path for the photons of the lines considered, appreciably smaller than the thermal velocity of the corresponding ions, so that the "clearing" of the medium due to the velocity gradient is small. We will accordingly assume that the gas in front of the shock moves at constant velocity,[1] $V(z) = \text{const} = V_0$. This enables us to consider the radiative transfer

[1] It also follows from the mass conservation law that $N(z) = \text{const} = N_0$.

Table 3

V_0, km/s	$\log N_0\,(\mathrm{cm}^{-3})$	Z_{pre}, cm	$T_{\max}$, 10^4 K	τ^0_{pre}			
				CIV	NV	OVI	SiIV
200	11.0	$7.7+8$	1.67	$1.26+2$	1.46	$2.26-2$	$2.64+2$
	12.0	$7.0+7$	1.69	$1.31+2$	1.70	$2.29-2$	$2.57+2$
300	11.0	$6.4+9$	1.88	$3.84+3$	$4.45+2$	$3.12+2$	$2.46+3$
	12.0	$6.4+8$	1.91	$3.84+3$	$4.63+2$	$3.34+2$	$2.41+3$
400	11.0	$1.6+10$	2.02	$1.14+4$	$2.32+3$	$3.46+3$	$1.65+3$
	12.0	$1.6+9$	2.06	$1.13+4$	$2.34+3$	$3.55+3$	$1.61+3$

in the rest frame of the gas, which is moving from the observer with the velocity $V_0\mu$, where $0 \le \mu \le 1$. In other words, for the region in front of the shock, we will calculate the line profiles in a stationary layer of gas, denoting the frequency in this frame as ν. If the final results are represented using $v = c(\nu_0 - \nu)/\nu_0$ instead of the frequency, the line profiles in the observer's rest frame are obtained by shifting the calculated profiles a distance $V_0\mu$ along the horizontal axis.

Table 3 presents the variations of the optical depths in the region in front of the shock $\tau_{pre}(\mu = 1)$ (the preshock region) at the center of the $1 \leftrightarrow 3$ transition lines for the studied ions as functions of the velocity and density of the gas. Table 3 also gives the characteristic size of the layer in which the lines are formed, Z_{pre}, and the maximum temperature of the gas reached immediately in front of the shock, $T_{\max}$. We can see that τ^0_{pre} can be $\gg 1$, so that, generally speaking, photoexcitation cannot be neglected in this region. Therefore, we must solve a system consisting of Eqs. (2) and (8), which we write in the form

$$\mu \frac{\mathrm{d}I_\nu}{\mathrm{d}\tau} = \phi_\nu (S - I_\nu), \qquad (12a)$$

$$S = \frac{1-\varepsilon}{2} \int_0^\infty \phi_\nu \mathrm{d}\nu \int_{-1}^{1} I_\nu \mathrm{d}\mu + \varepsilon B_0. \qquad (12b)$$

The boundary conditions for this system is

$$I_\nu = 0 \quad \text{for} \quad \tau = 0 \ \text{and} \ \mu \le 0, \qquad (13a)$$

$$I_\nu = I^{pst}_\nu \quad \text{for} \quad \tau = \tau_{pre} \ \text{and} \ \mu \ge 0, \qquad (13b)$$

where I^{pst}_ν is the line radiation intensity from the region behind the accretion-shock front [see (11)] taking into account the shift by $-V_0\mu$ in v.

In the region of line formation, the gas temperature varies by roughly a factor of 1.5 [2]. For this reason, ε varies by approximately the same factor inside the layer considered; however, the profile of the absorption coefficient ϕ_ν and the Planck function B_0 vary rather strongly. Consequently, in our case, $\varepsilon = \varepsilon(\tau)$, $\phi_\nu = \phi_\nu(\tau)$, $B_0 = B_0(\tau)$, so that no analytical solution of the type [15] exists for this problem, which we therefore solved numerically.

Before describing our solution technique, we will present characteristic values of the optical parameters of the layer, based on the results for the CIV 1548 line and the shock model with $V_0 = 300$ km/s and $\log N_0 = 11$. In this case, $\varepsilon \simeq 3 \times 10^{-5}$ and $a \simeq 2 \times 10^{-7}$. This corresponds to a characteristic optical depth for which thermalization of the radiation in this line will be substantial $\Lambda \sim 3 \times 10^4$; see formula (11.26a) in [16]. [2] The optical depth of the layer τ^0_{pre} is a factor of a few lower than this value (Table 3); i.e., the layer is effectively thin. It turns out that, for all lines considered with $200 < V_0$, km/s < 400, and $\log N_0 < 12.5$, the thermalization of the radiation is not very large.

Returning to our specific numerical example, it turns out that the mean free path of CIV 1548 photons is $\sim 2 \times 10^6$ cm in the middle of the layer considered. Having estimated the average number of scatterings in the layer $\mathcal{N}$ from the relation $\mathcal{N} \sim \tau^0_{pre}(\ln \tau_{pre})^{1/2}$ [14, 16], we see that the mean free path of the photons until they leave the layer is comparable to the size of the layer, Z_{pre}. However, the gas velocity V_0 is three orders of magnitude lower than the velocity of light; therefore, no more than 0.1% of all the matter in the layer will have time to pass through the front during the time a photon is inside the layer. This enables us to consider the radiative

[2] Relation (11.26b) in [16], given for the estimated thermalization optical depth in the case of a Voigt profile, yields an incorrect result for $a \ll 1$; it was derived assuming that $H(a, x) \propto a$, and therefore it does not transform into (11.26a), which corresponds to purely Doppler profile, as $a \to 0$.

transfer in the rest frame of the falling gas, and at the same time to use the boundary condition (13b).

We solved the system (12) numerically following the procedure described in § 6.3 of [16]. We briefly present the essence of the technique here. We introduced the variable $u_{\nu\mu} = [I_\nu(\tau, +\mu) + I_\nu(\tau, -\mu)]$, where, from now on, we will consider only positive values for μ: $\mu \in [0, 1]$. In the equation for $u_{\nu\mu}$, the derivatives

$$\mu^2 \frac{\mathrm{d}^2 u_{\nu\mu}}{\mathrm{d}\tau_\nu^2} = u_{\nu\mu} - S$$

were replaced by finite differences for τ_ν, with the interval $[0, \tau_{pre}]$ being partitioned into 30–70 subintervals. In the expression for the source function

$$S = (1-\varepsilon) \int_{-\infty}^{\infty} \phi(x)\mathrm{d}x \int_0^1 u_{\nu\mu}\mathrm{d}\mu + \varepsilon B_0,$$

the integrals over μ and ν were replaced by 6-point and 64-point quadrature sums, respectively. Adding the boundary conditions (see (6.33) and (6.35) in [16]), we obtained a closed system of algebraic equations, which was solved using the method of Rybicky [19].

Our computer program was tested by calculating line profiles for the case of a homogeneous layer with the zero boundary condition (13b) for various τ_{pre}, ε, and a. Our profiles are virtually identical to those presented in Fig. 6 in [20] for the same parameters. When calculating the profiles in the case of a shock, we also investigated the dependence of the results on the number of points in the partitions over τ, μ, and ν, which demonstrated the reliability of the calculation results.

5. DISCUSSION

The line profiles were calculated for V_0 values from 200 to 400 km/s in steps of 50 km/s and $\log N_0$ values from 11.0 to 13.0 in steps of 0.5, since precisely this range of V_0 and N_0 is of interest in the case of classical T Tauri stars [2]. For $V_0 = 200$, 250, and 300 km/s, we also calculated profiles for $\log N_0 = 10.5$. For larger velocities, the extent of the region in front of the shock becomes comparable to the radius of a classical T Tauri star, and the application of the plane shock approximation becomes problematic.

Figure 3 presents the results of the CIV 1548 line profile calculations for $\log N_0 = 12.0$ and $V_0 = 200$ km/s, 300 km/s, and 400 km/s for $\mu = 0.034$, 0.619, and 0.966. For comparison, Fig. 4 presents the analogous results for the OVI 1032 line.

The gas velocity at the shock front displays a jump-like variation by approximately a factor of four. For this reason, the profiles of lines originating in regions in front of and behind the accretion-shock front are observed at very different frequencies and do not overlap when viewed from a direction nearly perpendicular to the front. As a result, the observed line profile has two components: one near $v = 0$, corresponding to the region behind the shock front, and the other dramatically shifted toward the red, formed in the preshock zone. Physically, this means that the region in front of the shock is transparent to the radiation from lower-lying regions, so that the profile of the "zero" component is identical to that obtained without taking into account the region in front of the shock. The "red" profile displays a two-peaked structure, which is similar to the shape of profiles originating in an effectively thin isothermal layer (see Fig. 6 in [20] or Fig. 11.4 in [16]).

As the angle between the line of sight and the normal to the front increases (and μ decreases), the distance between the components decreases, and when $V_0\mu$ becomes comparable to the width of the components, the profiles begin to overlap (Fig. 4). When μ is small, the optical depth of the region in front of the shock is high, so that the radiation from behind the front is strongly absorbed in the region where the profiles overlap. To illustrate this, Fig. 4 displays the line profiles originating behind and in front of the shock front for the zero boundary condition (13b) together with the combined profile for the case $V_0 = 300$ km/s and $\mu = 0.034$. The absorbed radiation is partially thermalized and partially re-emitted in other directions; therefore, the intensity of the "red" component integrated over all μ is slightly higher compared to its value in the case $I_\nu^{pst} = 0$.

The known relation for the intensities of the doublet components in the case of a homogeneous isothermal layer follows from (9) and (11) and the condition $\nu_{12} \simeq \nu_{13}$:

$$R_{32} \equiv \frac{I_{13}(\nu)}{I_{12}(\nu)} = 1 + \exp\left[-\frac{\tau_{12}(\nu)}{\mu}\right], \qquad (14)$$

where $\tau_{12}(\nu)$ is the optical depth of the layer in the $1 \leftrightarrow 2$ transition. It follows from (14) that, in a homogeneous layer, R_{32} lies in the interval from one to two, depending on whether the layer is optically thick or thin.

Figure 5 presents the ratio of the integrated intensities of the doublet components for all the ions considered. In the case of the CIV, NV, and SiIV ions, R_{32} lies in the interval from one to two and decreases as the angle between the normal to the shock front and the line of sight increases, probably due to the increase of the optical depth of the layer along the line

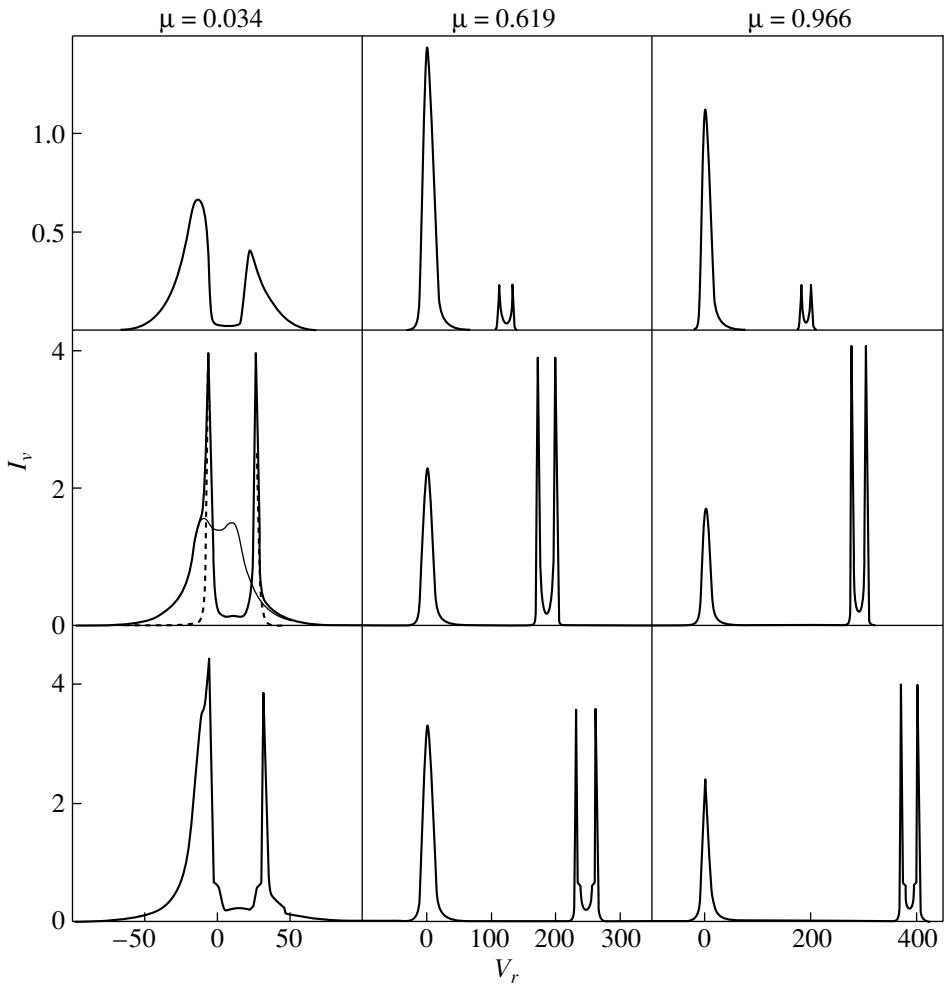

Fig. 3. Profile of the CIV 1548 line for an accretion shock with $\log N_0 = 12$ observed at various angles (thick solid curves). The upper, middle, and lower profiles are calculated for $V_0 = 200$, 300, and 400 km/s, respectively. For comparison, the contributions from the zone behind the accretion-shock front (thin solid curves) and in front of the accretion shock (dotted curves) are shown for $V_0 = 300$ km/s, $\log N_0 = 12$, and $\mu = 0.034$; see text for details. The plotted intensity is in units of 10^{-4} erg s^{-1}cm^{-2}sr^{-1} Hz^{-1}, and the radial velocity is in km/s.

of sight. However, in the case of the OVI ion, R_{32} is smaller than unity for some μ, due to the variation of the source function with depth and the overlapping of the profile components.

The dependence of the ratio R_{32} on V_0 is fairly complicated for all the ions. Its dependence on N_0 is simpler: R_{32} increases as N_0 decreases. To more clearly illustrate this, we present the results of the calculations for the CIV ion for $V_0 = 300$ km/s and $\log N_0 = 12.0$ and $\log N_0 = 11.0$, as for the other ions, and also for $\log N_0 = 10.5$.

The vast majority of UV spectra of T Tauri stars have been obtained by the IUE satellite with low resolution ($\Delta\lambda \simeq 6$ Å). These spectra do not contain any information about the line profiles, and the CIV 1550 doublet lines merge into a single emission feature. Therefore, it is of interest to see whether the ratio of the total intensities of the doublets $I_\Sigma = I_{12} + I_{13}$ for different ions can be used to determine the parameters of the accretion shock. To this end, we calculated the ratios of the intensities of the NV 1240, OVI 1035, and SiIV 1400 doublets to the intensity of the CIV 1550 doublet. Figure 6 displays the variations of this ratio as a function of μ for $V_0 = 200$, 300, and 400 km/s for $\log N_0 = 11.0$ and 12.0.

The dependence of the total intensity I_Σ on μ, i.e., "the limb darkening law," is of particular interest for the CIV 1550 doublet. We can see in Fig. 7 that the calculated dependence $I_\Sigma(\mu)$ is not monotonic, and a limb "lightening" rather than darkening is observed for angles θ from 0° to ~75°; a similar effect is seen for the CIV 1550 doublet for the case of the Sun [16]. For reasons that will become clear below, we present

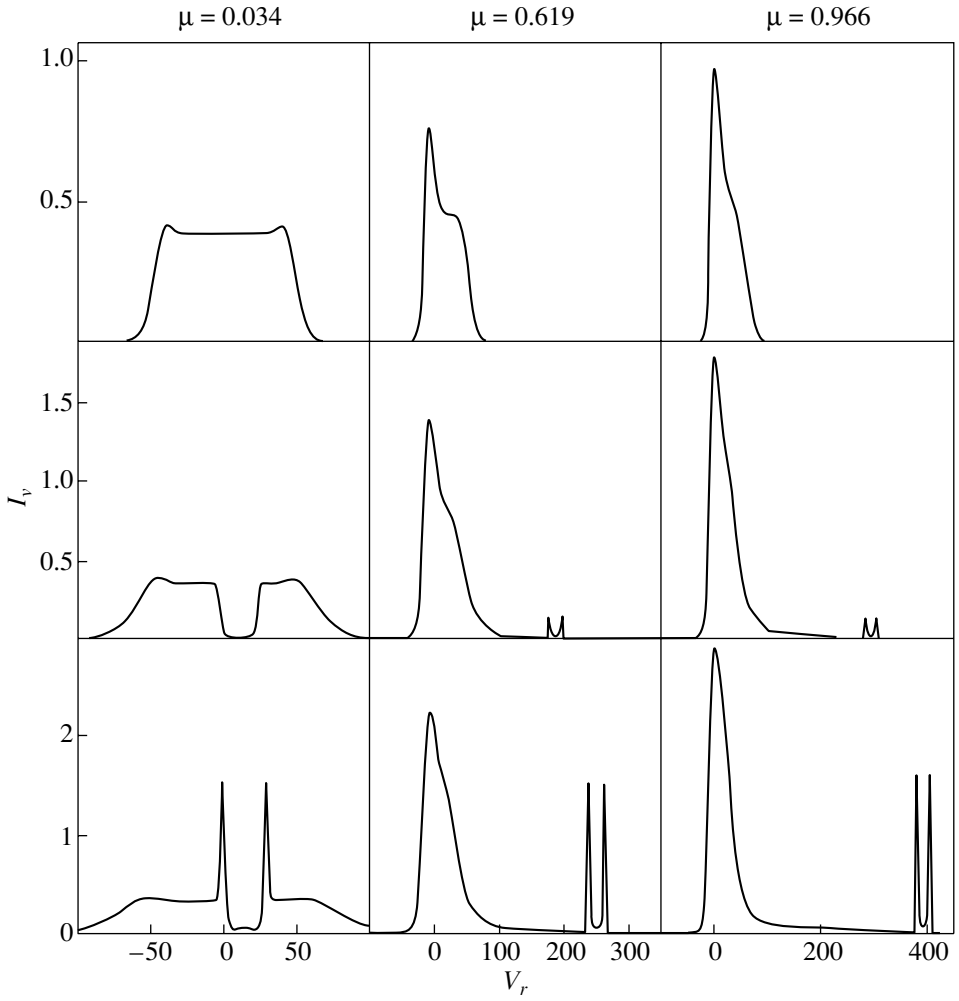

Fig. 4. Same as Fig. 3 for the OVI 1032 line.

δ_{CIV} in Fig. 7 instead of I_Σ, specified by the relation

$$I_\Sigma = \delta_{\mathrm{CIV}} \frac{\rho_0 V_0^3}{4}. \qquad (15)$$

It follows from Figs. 3–7 that the shapes of the profiles, as well as the absolute and relative intensities of the studied lines, can vary dramatically with variations in the velocity V_0 and density N_0 of the accreted gas in front of the shock, making it possible to use these lines for diagnostics. In addition, the profiles and intensities are also strongly dependent on the angle at which the plane-parallel shock is viewed. This confirms the conclusion made in [2] that, without information about the geometry of the accretion zone, the lines studied here cannot be used to determine V_0, N_0, the accretion rate $\dot{M}_{ac}$, or the area S_{ac} occupied by the accretion shock on the surface of the star facing the observer.

However, even based on the results for a plane-parallel shock, we can draw a number of conclusions about the character of the accretion in classical T Tauri stars. First and foremost, Figs. 3 and 4 indicate that the width of the "red" component of the profile does not exceed $\sim 0.1V_0$. This enables us to estimate V_0 fairly accurately from the extent of the red wings of the studied lines—naturally, if we are confident that at least some of the falling gas moves nearly along the line of sight. This confirms that $V_0 < 400$ km/s in the classical T Tauri case [21–25]. These same studies indicate that the lower boundary of V_0 is 250 km/s.

The CIV 1550-doublet profiles observed in classical T Tauri stars do not display the two-component structure that is characteristic of a plane shock; compare the corresponding figures in [8, 21–25] with Fig. 3. This suggests that the flow lines in the accretion zone are oriented in a wide range of angles relative to the line of sight. This rules out accretion in the form of a cylindrical jet [26].

According to [3], the observed veiling continuum in classical T Tauri stars forms in the transition layer

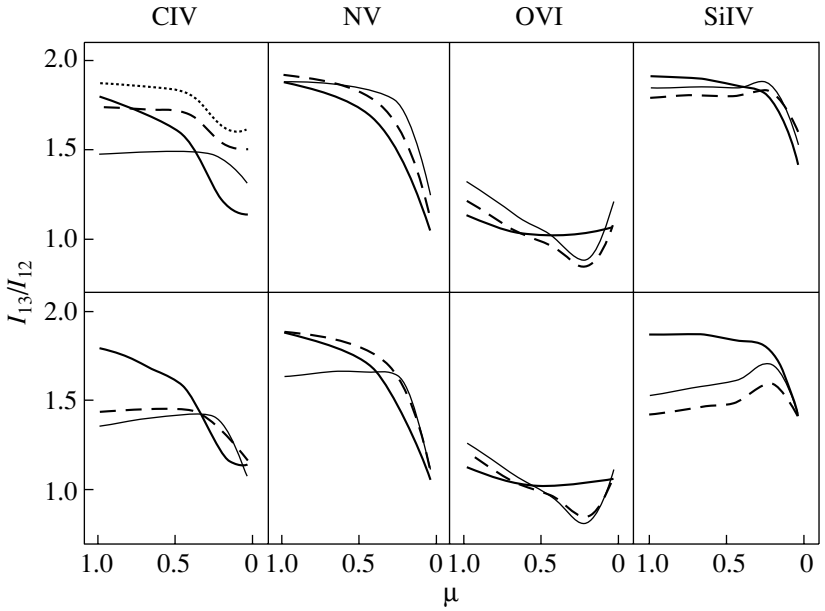

Fig. 5. I_{31}/I_{21} intensity ratio for the CIV, NV, OVI, and SiIV doublets as a function of μ for $V_0 = 200$ km/s (thick solid curves), 300 km/s (dashed curves), and 400 km/s (thin solid curves). The upper row corresponds to $\log N_0 = 11$ and the lower row to $\log N_0 = 12$. The dotted curve presents the dependence for the CIV doublet for $V_0 = 300$ km/s and $\log N_0 = 10.5$.

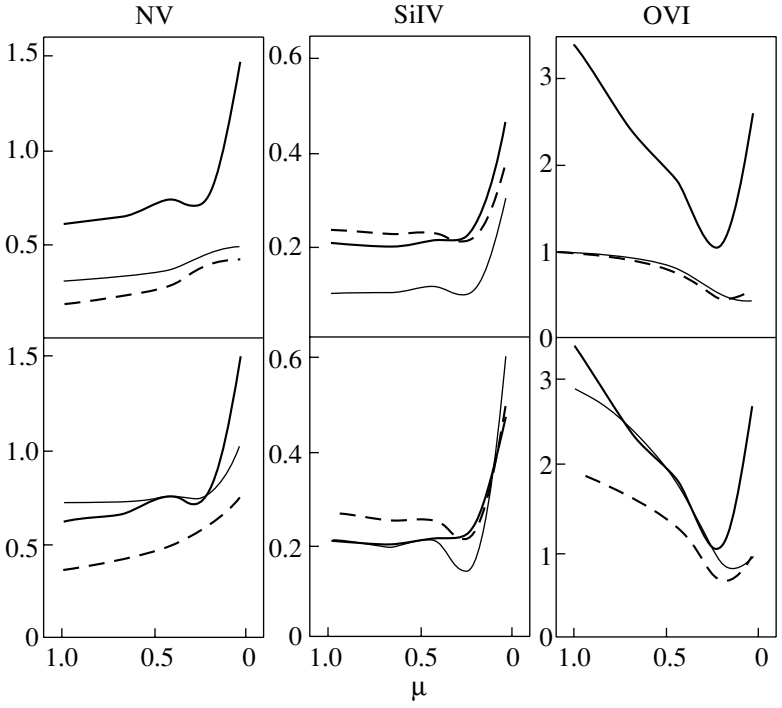

Fig. 6. The ratio of the total intensities $I_{12} + I_{13}$ of the NV, OVI, and SiIV doublets and the CIV 1550 doublet as a function of μ for $V_0 = 200$ km/s (thick solid curves), 300 km/s (dashed curves) and 400 km/s (thin solid curves). The upper row corresponds to $\log N_0 = 11$ and the lower row to $\log N_0 = 12$.

between the shock and the star: in this region, the shock radiation directed toward the star is absorbed. Due to the high density of the gas, the absorbed energy is re-emitted, primarily in the continuum (see [2] for more detail). Therefore, we can assume that a unit area of the accretion-shock surface radiates half of the energy of the accreted gas; i.e., $0.5 \times \rho_0 V_0 \times V_0^2/2$. Let us assume that $\rho_0 V_0^3$ varies little within the ac-

cretion zone (the accretion is homogeneous). Then, without taking interstellar absorption into account, the bolometric continuum flux near the Earth will be

$$F_c^{\oplus} = \frac{\rho_0 V_0^3}{4}\frac{S_{ac}}{2\pi d^2}, \qquad (16)$$

where d is the distance to the star.

On the other hand, the total observed flux in the CIV 1550 doublet lines, also corrected for interstellar absorption, is equal to [16]

$$F_{\rm CIV}^{\oplus} = \frac{1}{d^2}\int_{S_{ac}} \mu I_\Sigma \mathrm{d}S. \qquad (17)$$

Here, the integration is carried out over the surface of the accretion zone, located on the stellar hemisphere facing the observer. From (15) and (17), we obtain for the case of homogeneous accretion

$$F_{\rm CIV}^{\oplus} = \frac{\rho_0 V_0^3}{4}\frac{S_{ac}}{\pi d^2}\langle \mu\delta_{\rm CIV}\rangle,$$

where $\langle \mu\delta_{\rm CIV}\rangle$ is averaged over the integration region. According to Fig. 7, $\delta_{\rm CIV}$ differs from 0.7% by no more than a factor of 2.5, for any V_0, N_0, and μ. The large extent of the red wings of the CIV 1550 lines in classical T Tauri spectra indicates that the contribution from regions with $\mu \sim 1$ cannot be very small; therefore, we will adopt the average value $\mu \sim 0.5$. Using (16), we find that, if the veiling continuum and the CIV 1550 doublet lines are formed in the accretion shock, then

$$\frac{F_{\rm CIV}^{\oplus}}{F_c^{\oplus}} = 2\pi\langle \mu\delta_{\rm CIV}\rangle \sim 2\%. \qquad (18)$$

At the same time, the ratios $F_{\rm CIV}^{\oplus}/F_c^{\oplus}$ observed for DR Tau [8], T Tau, and RY Tau [27] are two orders of magnitude smaller. Since there is no doubt that the CIV 1550 lines form in the accretion shock, the discrepancy between the theory and observations provides evidence that the emission continuum is formed beyond the accretion shock, at least in the case of the mentioned stars. Since there is also no doubt that the veiling continuum is due to disk accretion, we conclude that this continuum forms in the inner regions of the disk. However, the ratio of the luminosities of the accretion disk and disk should be of the order of the ratio of the inner radius of the disk and the radius of the star [28], so that this ratio cannot exceed unity, even if the disk reaches the surface of the star.

It means that, in the case of DR Tau, T Tau, and RY Tau, the stellar magnetic field does not stop the accretion disk at some distance from the stellar surface, as is commonly believed (see the Introduction). In fact, the disks reach the surfaces of these stars, so that the bulk of the accreted matter falls onto the stars in the equatorial plane, and only ~1% of the gas becomes frozen in the magnetic field; the gas falls onto the star at higher latitudes, forming an accretion shock. Note that, according to [31], the temperature of the gas in the inner regions of the disk and/or in the boundary layer of classical T Tauri stars cannot exceed 10 000–15 000 K; therefore, the energy released by the accretion will be radiated here, primarily in the continuum and hydrogen lines, and the CIV, NV, OVI, and SiIV lines cannot be formed in this region.

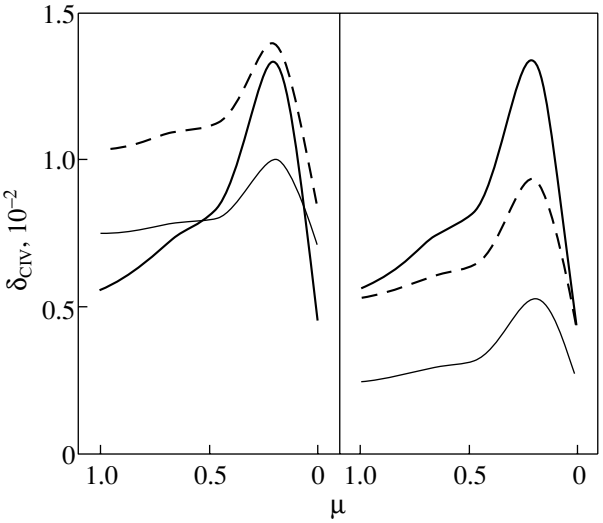

Fig. 7. Intensity of the CIV 1550 doublet lines as a function of μ for $V_0 = 200$ km/s (thick solid curves), 300 km/s (dashed curves), and 400 km/s (thin solid curve). The intensity is normalized to $\rho_0 V_0^3/4$; see text for detail. The left panel corresponds to $\log N_0 = 11$ and the right panel to $\log N_0 = 12$.

In subsequent studies, we plan to compare the calculated and observed profiles and intensity ratios of the components of doublets of various ions under various assumptions about the accretion-shock geometry. We note here that the OVI 1035 doublet has been observed only in TW Hya [29] and T Tau [30] (by the FUSE satellite). Unfortunately, in both stars, the doublet lines are strongly blended with absorption lines of molecular hydrogen and cannot be used for comparison with our calculations.

6. CONCLUSIONS

We have calculated the CIV 1550, NV 1240, OVI 1035, and SiIV 1400 resonance doublet profiles for a plane-parallel shock viewed at various angles and for various velocities and densities of the gas in front of the shock. Comparison of the calculated and observed profiles and relative intensities of these lines has proved to be an effective method for estimating the parameters of accretion shocks in classical T Tauri stars. At the same time, these lines cannot be

used to determine the parameters of the accreted gas without knowledge of the geometry of the accretion zone.

If V_0 and N_0 are the same at all points in the accretion shock, it seems reasonable to assume that the accretion zone is an axisymmetric surface similar to an extended spot or a spherical belt [6]. In this case, the size of the region and the orientation of its axis of symmetry relative to the line of sight will become parameters of the problem, along with V_0 and N_0. We plan to investigate this problem in subsequent studies.

A much more complicated situation for accretion-shock diagnostics will arise when V_0 and N_0 vary appreciably within the accretion zone, as is natural if the magnetic axis of the star is significantly inclined to its rotational axis. There is a hope that a technique similar to Doppler tomography can be applied to determine the parameters of accretion shocks in the case of inhomogeneous accretion. We are referring to the possibility of analyzing the variability of the line profiles due to variations in the accretion shock's orientation relative to the observer in the course of the axial rotation of the star. In this case, we can use the relations $I_\nu(\mu, V_0, N_0)$ in the same way that the relations $I_\nu(\mu)$ obtained from stellar atmosphere models are used in classical Doppler tomography. The idea seems very promising, although it is not clear if it will always be possible to separate the periodic and stochastic (due to the nonstationary accretion) components of the observed line-profile variations for classical T Tauri stars.

7. ACKNOWLEDGMENTS

The author thanks D.I. Nagirner for discussions on the formulation of the problem and methods for its solution, M.S. Dimitrijevic for information about the shock-broadening parameters for the considered lines, and the referee, V.P. Grinin, for comments that led to the correction of a number of shortcomings in the original version of the paper. This work was supported by the Russian Foundation for Basic Research (project no. 02-02-16070). All the calculation results are available upon request.

REFERENCES

1. S. A. Lamzin, Astron. Astrophys. **295**, L20 (1995).
2. S. A. Lamzin, Astron. Zh. **75**, 367 (1998) [Astron. Rep. **42**, 322 (1998)].
3. N. Calvet and E. Gullbring, Astrophys. J. **509**, 802 (1998).
4. G. Basri and C. Bertout, Astrophys. J. **341**, 340 (1989).
5. A. I. Gómez de Castro and S. A. Lamzin, Mon. Not. R. Astron. Soc. **304**, 41 (1999).
6. S. A. Lamzin, Astron. Zh. **77**, 373 (2000) [Astron. Rep. **44**, 323 (2000)].
7. A. I. Gómez de Castro and E. Verdugo, Astrophys. J. **548**, 976 (2001).
8. A. S. Kravtsova and S. A. Lamzin, Pis'ma Astron. Zh. **28**, 748 (2002) [Astron. Lett. **28**, 676 (2002)].
9. G. Beristain, S. Edwards, and J. Kwan, Astrophys. J. **551**, 1037 (2001).
10. M. S. Dimitrijevic, S. Sahal-Brechot, and M. Bommier, Astron. Astrophys., Suppl. Ser. **89**, 581 (1991).
11. M. S. Dimitrijevic and S. Sahal-Brechot, Astron. Astrophys., Suppl. Ser. **95**, 109 (1992).
12. M. S. Dimitrijevic and S. Sahal-Brechot, Astron. Astrophys., Suppl. Ser. **93**, 359 (1992).
13. M. S. Dimitrijevic, S. Sahal-Brechot, and M. Bommier, Astron. Astrophys., Suppl. Ser. **89**, 591 (1991).
14. V. V. Ivanov, *Radiative Transport and the Spectra of Astronomical Bodies* [in Russian] (Nauka, Moscow, 1969).
15. D. I. Nagirner and A. B. Shnevais, Astron. Zh. **54**, 162 (1977) [Sov. Astron. **21**, 91 (1977)].
16. D. Mihalas, *Stellar Atmospheres* (Freeman, San Francisco, 1978; Mir, Moscow, 1982).
17. M. S. Dimitrijevic, private communication (2001).
18. E. Landi, M. Landini, K. P. Dere, *et al.*, Astron. Astrophys., Suppl. Ser. **135**, 339 (1999).
19. G. Rybicky, J. Quant. Spectrosc. Radiat. Transf. **11**, 589 (1971).
20. E. H. Avrett and D. G. Hummer, Mon. Not. R. Astron. Soc. **130**, 295 (1965).
21. S. A. Lamzin, Pis'ma Astron. Zh. **26**, 273 (2000) [Astron. Lett. **26**, 225 (2000)].
22. S. A. Lamzin, Pis'ma Astron. Zh. **26**, 683 (2000) [Astron. Lett. **26**, 589 (2000)].
23. L. Errico, S. A. Lamzin, and A. A. Vittone, Astron. Astrophys. **357**, 951 (2000).
24. S. A. Lamzin, A. A. Vittone, and L. Errico, Pis'ma Astron. Zh. **27**, 363 (2001) [Astron. Lett. **27**, 313 (2001)].
25. L. Errico, S. A. Lamzin, and A. A. Vittone, Astron. Astrophys. **377**, 577 (2001).
26. P. F. C. Blondel, A. Talavera, and H. R. E. T. A. Tjie, Astron. Astrophys. **268**, 624 (1993).
27. A. S. Kravtsova and S. A. Lamzin, Pis'ma Astron. Zh. **28**, 928 (2002) [Astron. Lett. **28**, 835 (2002)].
28. N. I. Shakura and R. A. Syunyaev, Astron. Astrophys. **24**, 337 (1973).
29. G. J. Herczeg, J. L. Linsky, J. A. Valenti, *et al.*, Astrophys. J. **572**, 310 (2002).
30. E. Wilkinson, G. M. Harper, A. Brown, and G. J. Herczeg, Astron. J. **124**, 1077 (2002).
31. C. Bertout, Ann. Rev. Astron. Astrophys. **27**, 351 (1989).

Translated by K. Maslennikov

Astronomy Reports, Vol. 47, No. 6, 2003, pp. 511–516. Translated from Astronomicheskiĭ Zhurnal, Vol. 80, No. 6, 2003, pp. 556–562.

Model of a Multiscaled MHD Dynamo

D. D. Sokoloff and P. G. Frick

Moscow State University, Moscow, 119992 Russia
Institute of Continuum Mechanics, Ural Division, Russian Academy of Sciences, ul. Akademika Koroleva 1, Perm, 614061 Russia
Received August 15, 2002; in final form, November 27, 2002

Abstract—A simple model for a multiscaled MHD dynamo is suggested. The uppermost tier of the model controls the evolution of the large-scale magnetic field, while the lower tiers are responsible for the evolution of the small-scale velocity and magnetic fields. This approach makes it possible to reproduce, e.g., the evolution of the Galactic magnetic field for realistic magnetic Reynolds numbers, which cannot be done using direct, detailed simulations. © *2003 MAIK "Nauka/Interperiodica"*.

1. INTRODUCTION

The origin and evolution of the magnetic fields of astronomical bodies are attributed to the action of the hydromagnetic-dynamo mechanism (see, e.g., [1, 2]). The large-scale and small-scale components of the magnetic field produced by this mechanism behave quite differently. While various investigators have reached a high level of agreement concerning the behavior of the large-scale fields, the evolution of the small-scale fields remains a point of controversy (see, e.g., [3]). It is in part these disagreements that have prompted the most recent attempts to revise the foundations of dynamo theory in the early 1990s by Vainshtein and Cattaneo [4] and Gruzinov and Diamond [5].

Studies of small-scale magnetic fields are complicated by the fact that the parameters governing the dynamo process typically assume enormous values in astronomical bodies. For example, the magnetic Reynolds numbers in galaxies are as high as 10^6, even if the magnetic diffusion is assumed to be ambipolar, and these numbers become much higher for estimates based on Coulomb collisions. Therefore, in spite of the tremendous progress in computational physics achieved in recent years, which has yielded some confirmation of the principal concepts of dynamo theory, direct and complete descriptions of the dynamos operating in real astronomical objects remain far beyond the ability of computational studies.

However, a new approach that seems to promise substantial improvements in this situation has recently appeared [6]. Of course, we are not speaking of a complete description of the phenomenon. However, note that, of the huge number of degrees of freedom that are formally necessary to describe the small-scale magnetic field, only a relatively small number characterizing the behavior of the mean properties of the small-scale fields are of real interest. These properties can be described using so-called cascade turbulence models, which replace complex partial differential equations with a relatively simple system of ordinary differential equations that lends itself to numerical treatment for realistic values of the characteristic parameters.

The cascade-model technique is essentially a direct development of the ideas of A.N. Kolmogorov, whose school pioneered studies in this field [7, 8]. These techniques have proved their worth in various problems in the theory of turbulence. We suggest a joint description of large-scale variables based on the mean-field equations and of small-scale variables in the framework of cascade models.

It is obvious that a crucial aspect of this approach is matching the equations responsible for the large-scale and small-scale variables. This procedure is difficult to formalize and must be elaborated separately for each particular case. This is precisely the aim of the present study. We choose a very simple problem in dynamo theory—the so-called α^2-dynamo—as the large-scale component of our study. In this problem, as usual, the toroidal component of the large-scale magnetic field gives rise to a poloidal component via the mean helicity; however, the feedback loop is closed by the same helicity, rather than by differential rotation (which is normally more efficient in this respect). Our choice is dictated by the fact that the structure of the generated magnetic field is very simple in this dynamo problem; if we are interested in the magnetic-field distribution in the vicinity of the point of most intense dynamo generation (in our case, the point of maximum helicity), this structure can be described using only one spatial mode [9]. In other words, the behavior of the large-scale component

1063-7729/03/4706-0511$24.00

can also be described using an ordinary differential equation.

Such α^2 dynamos are not very typical of astrophysical situations, although they can operate in close binaries, where differential rotation is inhibited by tidal interactions. However, the positive experience acquired in matching the systems for the microscopic and macroscopic variables described below also seems promising for future studies of more realistic (and more complex) situations.

2. CASCADE MODEL OF MHD TURBULENCE

To describe the generation and transfer of the small-scale magnetic field by small-scale turbulence, we use the cascade model of MHD turbulence proposed by Frick and Sokoloff [10]. The basic idea underlying cascade turbulence models is the construction of a chain of ordinary differential equations that describe the spectral energy transfer in highly developed turbulence. In the case of MHD turbulence, the problem is to retain, for any wavenumber octave $k_n < |\mathbf{k}| < k_{n+1}$, $k_n = 2^n$, only one pair of complex variables U_n and B_n that characterize the velocity and magnetic-field pulsations on the corresponding scales, and to write a system of equations for these variables that preserves certain "basis properties" of the original MHD equations. By "basis properties", we mean the type of nonlinearity and conservation laws obeyed by the original equations in the limit of large Reynolds numbers (both hydrodynamic and magnetic). Without dwelling on the properties of cascade models (to which hundreds of papers have already been devoted), we write the equations of the cascade model used here in the form

$$(d_t + \mathrm{Re}^{-1}k_n^2)U_n \tag{1}$$
$$= ik_n\Big\{(U^*_{n+1}U^*_{n+2} - B^*_{n+1}B^*_{n+2}) - \frac{1}{4}(U^*_{n-1}U^*_{n+1} - B^*_{n-1}B^*_{n+1}) + \frac{1}{8}(U^*_{n-2}U^*_{n-1} - B^*_{n-2}B^*_{n-1})\Big\} + f_n,$$

$$(d_t + Rm^{-1}k_n^2)B_n \tag{2}$$
$$= \frac{ik_n}{6}\Big\{(U^*_{n+1}B^*_{n+2} - B^*_{n+1}U^*_{n+2}) + (U^*_{n-1}B^*_{n+1} - B^*_{n-1}U^*_{n+1}) + (U^*_{n-2}B^*_{n-1} - B^*_{n-2}U^*_{n-1})\Big\}.$$

These equations are written in a dimensionless form, where Re is the hydrodynamic Reynolds number, Rm is the magnetic Reynolds number, d_t is the derivative with respect to time, and the characteristic turnover time of an eddy on the maximum scale, $T = L_0/U_0$, is used as the unit of time. The structure of the nonlinear terms in (1), (2) is such that only local interactions are taken into account (energy exchange takes place only between neighboring scales); in the limit of $\mathrm{Re}, \mathrm{Rm} \to \infty$, the equations retain only three quadratic terms corresponding to the three integrals of motion known in magnetohydrodynamics—the total energy $E = E_U + E_B$ (where $E_U = \sum |U_n|^2/2$, $E_B = \sum |B_n|^2/2$), the cross helicity $H_c = \sum(U_n B^*_n + B_n U^*_N)$, and the magnetic helicity $H_b = \sum(-1)^n |B_n|^2/k_n)$. The f_n terms in (1) describe the action of the forces giving rise to the turbulent flow.

We should emphasize that, along with positively defined integrals of motion such as the energy or the enstrophy (an integral in two-dimensional fluid motion; cascade models of two-dimensional turbulence conserve its analog), cascade models can also conserve quantities whose sign is not known in advance. Such integrals in fluid mechanics are usually called helicities (a term that was brought into use by the discovery of the fact that, in addition to the energy, the incompressible motion of an ideal fluid also conserves the mean dot product of the velocity and its curl, which reflects the predominance of helical structures of one particular sign). In cascade models, the sign of the helicity reflects the predominant contribution of either odd or even tiers to the corresponding quantity. Helicity can be introduced into real cosmic turbulence either by an external force, such as the Coriolis force, or as an initial condition for the formation of turbulence. In our case, we specified some helicity at the initial time for the evolution and did not specially sustain it.

Our cascade model of MHD turbulence not only was able to reproduce the basis properties of the small-scale turbulence but also enabled us to study the effect of the magnetic Prandtl number on the generation threshold for small-scale magnetic fields [11] and to simulate the behavior of forced MHD turbulence for very long time intervals [12] and the characteristic features of this behavior in the case of free degeneration [13].

3. COMBINED MODEL FOR AN α^2 DYNAMO

Let the evolution of the large-scale magnetic field be determined by the behavior of its poloidal, B_P, and toroidal, B_T, components, for which the following equations are valid:

$$d_t B_P = ik_L \alpha B_T - \beta B_P, \tag{3}$$

$$d_t B_T = -ik_L \alpha B_P - \beta B_T, \tag{4}$$

where α describes the ability of non-reflection-invariant, small-scale turbulence to generate the mean, large-scale magnetic field; β is the effective

diffusion coefficient of the turbulent medium; and k_L is the wavenumber determining the macroscopic scale L. In other words, the poloidal magnetic field is produced from the toroidal field by the helicity, and vice versa, and both are affected by turbulent diffusion. It is this process that is called the α^2 dynamo.

The idea behind the combined model is to supplement equations (3), (4) with the cascade equations (1), (2). The coefficients α and β are obtained from the solutions to the cascade equations, and energy exchange between the turbulent flow and the generated large-scale magnetic field is taken into account. The coefficient α is related to the helicity of the turbulent flow,

$$\alpha \approx \frac{1}{3}\tau\langle v\,\mathrm{curl}v\rangle,$$

to within the factor τ, which has the dimensions of time. Assuming that τ is associated with the turnover time for eddies with the corresponding scale, we can relate α to the parameters of the small-scale turbulence:

$$\alpha = C_\alpha \sum_n \tau_n (-1)^n k_n |U_n|^2 = C_\alpha \sum_n (-1)^n |U_n|. \tag{5}$$

The diffusion of the large-scale magnetic field is determined by the coefficient β, for which we adopt the estimate

$$\beta \approx \frac{1}{3}\tau\langle v^2\rangle;$$

the following formula in terms of the variables of the cascade equations corresponds to this estimate:

$$\beta = \frac{1}{3}\sum_n k_n^{-1}|U_n|. \tag{6}$$

Taking into account the outflow of kinetic energy from the turbulent flow generating the large-scale magnetic field is an important issue (the cascade equations themselves exactly obey the conservation laws and correctly describe the redistribution of the kinetic energy and the energy of the small-scale magnetic field). Obviously, the energy supplied to the large-scale magnetic field should be extracted from the turbulent kinetic energy via an appropriate correction of the variables U_n. We tried various corrections and ultimately adopted the following one for our model. Assuming that only structures carrying the dominant sign of the helicity are responsible for the generation of the magnetic field via the α effect, we subtract the energy supplied to the large-scale magnetic field that is associated with precisely those variables U_n that contribute to the helicity with the sign coinciding with the current sign of the coefficient α. For the cascade model, this means that coefficients U_n with either odd n or even n are recalculated. A coefficient introducing the necessary change in the kinetic energy when multiplied by all the corresponding U_n is computed.

Another important physical process that must be taken into account when combining the models for large-scale and small-scale processes is the generation of Alfvén waves due to the interaction of the large-scale magnetic field with small-scale MHD perturbations. This means that, in addition to local interactions, nonlinear interactions with the large-scale magnetic field must be taken into account in the cascade equations; these interactions have the form

$$d_t U_n = \ldots + \frac{1}{2} i k_L B_n^* (B_P^* + B_T^*),$$

$$d_t B_n = \ldots + \frac{1}{2} i k_L U_n^* (B_P^* + B_T^*).$$

Accordingly, the equations for the large-scale magnetic field become

$$d_t B_P = i k_L \alpha B_T - i k_L \sum_n U_n^* B_n^* - \beta B_P, \tag{7}$$

$$d_t B_T = -i k_L \alpha B_P - i k_L \sum_n U_n^* B_n^* - \beta B_T. \tag{8}$$

Equations (7) and (8) contain two types of dissipation terms associated with the large-scale magnetic field. The terms proportional to β represent the regular turbulent diffusion, which can, in our approximation, be determined from the system describing the small-scale variables. The other terms contain sums over small-scale variables and describe the transformation of the large-scale magnetic field into Alfvén waves.

4. NUMERICAL SIMULATIONS

We numerically integrated equations (7), (8) combined with the system (1), (2) for 26 variables U_n, B_n ($0 \le n \le 25$). The wavenumber range described by this system ($k_{\max}/k_{\min} \approx 10^8$) enables the consideration of $\mathrm{ReRm} = 10^{10}$. The boundary conditions in the region of small wavenumbers have the form $U_n = B_n = 0$ for any $n < 0$ and $n > 25$. The first condition (for negative n) corresponds to the presence of a maximum possible scale in the system, while the second condition (for large wavenumbers) is only formal, since dissipation actually becomes important several octaves before the boundary of the scale range considered, and energy does not reach the farthest tiers of the system. We adopt the value $k_L = 1/8$ (which corresponds approximately to the ratio of the small and large scales in the Galactic disk); in the energy spectra presented below, the large-scale field is

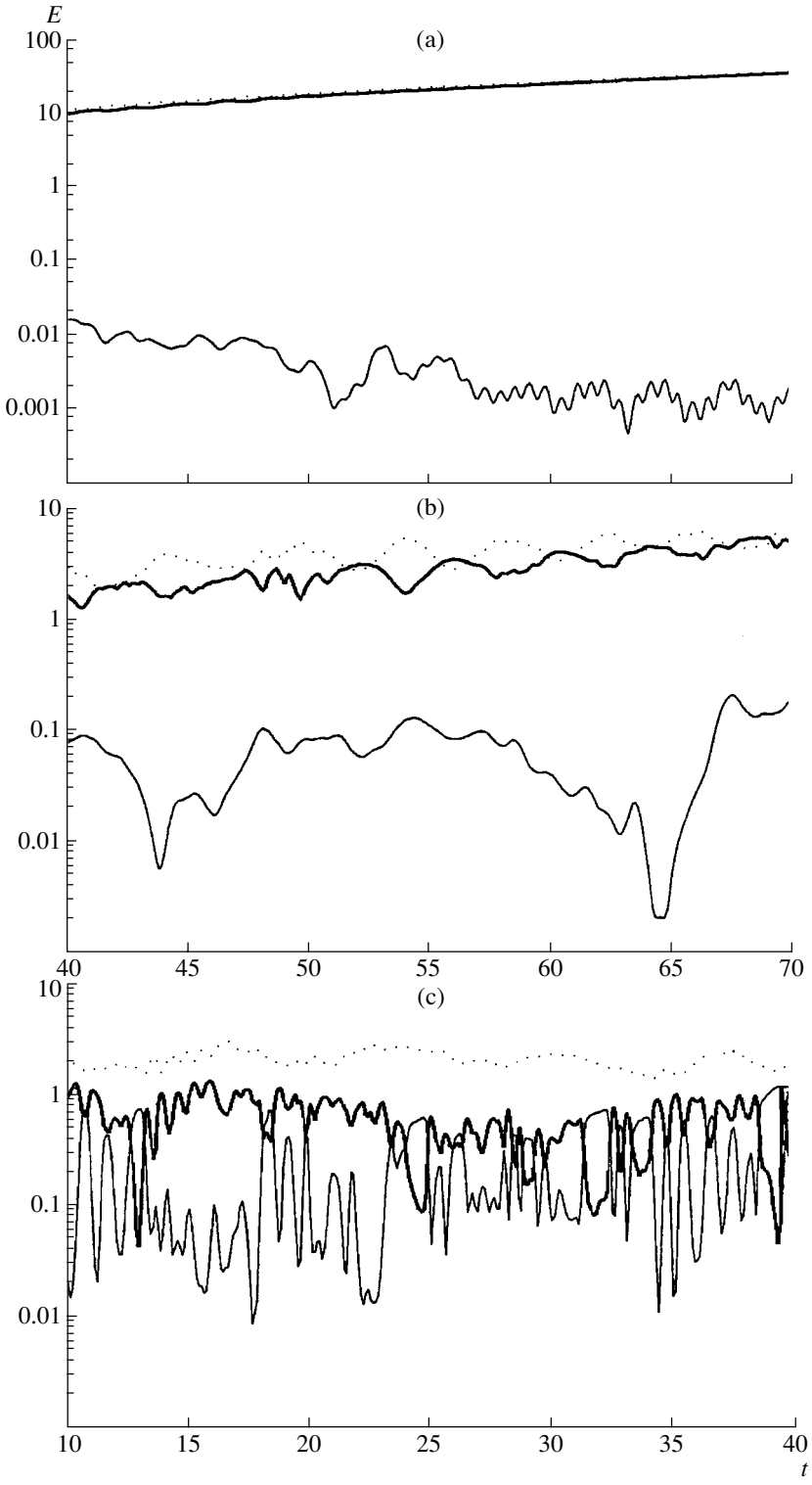

Fig. 1. Time evolution of the model for $C_\alpha =$ (a) 1, (b) 3, and (c) 100. See text for details.

represented by the leftmost point on the wavenumber axis.

Kinetic energy was pumped into the system by a force of the form $f_n = \delta_{0n}(1+i)$ in Eq. (1), which operates only on the zeroth tier, so that only the largest scale pulsations are fed. We adopted $\mathrm{Rm} = 10^6$, $\mathrm{Re} = 10^{10}$; i.e., the magnetic Prandtl number was set equal to 0.0001. This affects the behavior of the large-scale

magnetic field only slightly, and the particular value of the magnetic field was chosen in order to demonstrate that the velocity-pulsation spectrum on small scales, where no magnetic-field pulsations are present for the specified ratio of the kinematic and magnetic viscosities, behaves quite differently compared to most of the spectrum. Moreover, the adopted value of Rm is fairly close to the actual value of this parameter for the Galactic disk.

Figure 1 presents solutions to the system for several values of the parameter C_α determining the intensity of the dynamo effect; for an $\alpha\omega$ dynamo, the same role is played by the dynamo number. The time evolution is shown by the thick curves for the kinetic energy of the entire system, the dotted curves for the energy of the magnetic-field pulsations, and the thin curves for the energy of the large-scale magnetic field, which is the sum of the energies of the poloidal and toroidal components.

When $C_\alpha = 1$ (Fig. 1a), the large-scale magnetic field decays (a logarithmic scale is chosen for the energy axis). This C_α is close to the critical value $C_\alpha = 3$ (Fig. 1b) at which the large-scale magnetic field can survive. This field varies substantially in amplitude but remains so weak that it does not considerably affect the behavior of the small-scale turbulence. When $C_\alpha \approx 10$, the energy of the macroscopic field reaches values comparable to the kinetic energy of the velocity pulsations, and this field begins influencing not only the variations of the total pulsation energy but also the spectral distribution of this energy. Figure 1c illustrates the case of $C_\alpha = 100$. With such a high C_α, the magnetic-field variations become very intense, although irregular. The possibility of nonlinear dynamo regimes with chaotic time behavior has been noted in various mean-field dynamo models and was probably first identified in the Rikitake dynamo. Such regimes are of interest in the context of explaining the chaotic sequence of geomagnetic-field inversions. Our result confirms that chaotic regimes are not an artifact of the mean-field description of the dynamo, and are compatible with the inclusion of small-scale variables.

Note that, in this last case, the energy of the magnetic-field pulsations is much higher than the energy of the velocity pulsations, although the energy of the *large-scale* magnetic field remains somewhat lower than the kinetic energy. This suggests another possible resolution of the problem of the ratio of the energies of the large-scale and small-scale magnetic fields generated by the dynamo process, as raised by Vainstein and Cattaneo [4]. The possibility that a hydrodynamical force that sustains random motions in a nonlinear dynamo could, in principle, give rise to a very strong small-scale magnetic field is of interest for the solar-neutrino problem [14].

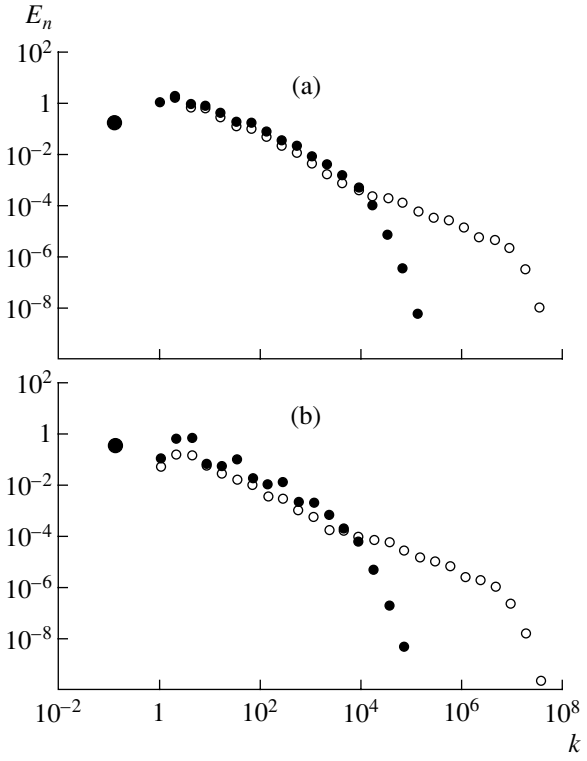

Fig. 2. Equilibrium spectra of the turbulence and magnetic field for $C_\alpha =$ (a) 3 and (b) 100. Shown are the turbulence spectrum (open circles), spectrum of the small-scale magnetic field (small solid circles), and the energy of the large-scale magnetic field (large solid circles). In some cases, a solid and open circle coincide, and only the solid circle is visible. See text for details.

Figure 2 presents the spectra of the velocity and magnetic-field pulsations for $C_\alpha = 3$ and $C_\alpha = 100$. In the former case, when the large-scale field is weak, there is equipartition of energy over all scales. The spectral slope exceeds the Kolmogorov value (and even more so the Kraichnan–Iroshnikov value), and is close to the slope of the spectrum $E(k) \sim k^{-2}$. The magnetic-field spectrum terminates before the turbulence spectrum, in accordance with the chosen Prandtl number. We can see that, in the small-scale region, where hydrodynamic turbulence is present, the spectral slope decreases, and reaches the Kolmogorov value. In the $C_\alpha = 100$ case, the spectral distribution in the MHD range is substantially less well ordered, and the corresponding values for the magnetic-field pulsations systematically exceed the kinetic energy on the corresponding scale.

5. CONCLUSIONS

We have already made some specific remarks that may be of interest in connection with special issues in dynamo theory. In general, we believe our dynamo model describing both large-scale and small-scale

magnetic fields confirms the possibility of using cascade models to describe the behavior of small-scale variables in dynamo theory. Further, a more sophisticated description of the large-scale variables could be developed, to include the more realistic $\alpha\omega$ dynamo, and also to use a more realistic (but not catastrophically high) number of large-scale variables when implementing either a spectral (as here) or a finite-difference [6] approach.

Our model directly answers the standard description of the growth of the large-scale magnetic field in dynamo theory. In particular, the gap between the k_L and k_0 scales in our model can, in principle, be as large as desired and is not filled with any auxiliary variables. Therefore, the concept of an inverse cascade (which implies the formation of the k_L-scale magnetic field directly from the preceding scale) is not necessary for the mean-field dynamo theory (cf. [15]).

Direct interactions between the large-scale field and small-scale magnetic-field and velocity pulsations (an analog of the Alfvén mechanism) play an important role in our model. As they are switched off, the generation threshold becomes much higher ($C_\alpha \approx 100$), and, as it is reached, strong instability appears in the behavior of the large-scale field (sharp bursts with subsequent drops by five or six orders of magnitude).

ACKNOWLEDGMENTS

This work was supported by the Russian Foundation for Basic Research under the RFBR–Ural program (project no. 01-01-96482).

REFERENCES

1. E. Parker, *Cosmic Magnetic Fields* (Oxford Univ. Press, Oxford, 1979; Mir, Moscow, 1982).
2. Ya. B. Zeldovich, A. A. Ruzmaikin, and D. D. Sokoloff, *Magnetic Fields in Astrophysics* (Gordon and Breach, New York, 1983).
3. R. Beck, A. Brandenburg, D. Moss, *et al.*, Ann. Rev. Astron. Astrophys. **34**, 155 (1996).
4. S. I. Vainstein and F. Cattaneo, Astrophys. J. **393**, 165 (1992).
5. A. V. Gruzinov and P. H. Diamond, Phys. Rev. Lett. **72**, 1651 (1994).
6. P. Frick, M. Reshetnyak, and D. Sokoloff, Europhys. Lett. **59**, 212 (2002).
7. E. B. Gledzer, Dokl. Akad. Nauk SSSR **193**, 1046 (1973).
8. V. R. Desnyanskii and E. A. Novikov, Prikl. Mekh. Mat. **38**, 507 (1974).
9. D. D. Sokoloff, A. A. Ruzmaikin, and A. M. Shukurov, Geophys. Astrophys. Fluid Dyn. **25**, 293 (1983).
10. P. Frick and D. Sokoloff, Phys. Rev. E **57**, 4155 (1998).
11. S. A. Lozhkin, D. D. Sokolov, and P. G. Frick, Astron. Zh. **76**, 853 (1999) [Astron. Rep. **43**, 753 (1999)].
12. P. Frick, G. Boffetta, P. Giuliani, *et al.*, Europhys. Lett. **52**, 539 (2000).
13. T. Yu. Antonov, P. G. Frick, and D. D. Sokolov, Dokl. Akad. Nauk **337**, 170 (2001).
14. A. A. Bykov, V. Yu. Popov, A. I. Rez, *et al.*, Phys. Rev. D **59**, 063001 (1999).
15. A. Brandenburg, K. Enquist, and P. Olesen, Phys. Rev. D **54**, 1291 (1996).

Translated by A. Getling

Astronomy Reports, Vol. 47, No. 6, 2003, pp. 517–524. Translated from Astronomicheskiĭ Zhurnal, Vol. 80, No. 6, 2003, pp. 563–570.

Solar Cyclicity during the Maunder Minimum

M. G. Ogurtsov[1], G. E. Kocharov[1], and Yu. A. Nagovitsyn[2]

[1] *Ioffe Physicotechnical Institute, Russian Academy of Sciences, Politekhnicheskaya ul. 26, St. Petersburg, 194021 Russia*

[2] *Main Astronomy Observatory, St. Petersburg, Russia*

Received September 21, 2002; in final form, November 27, 2002

Abstract—A multifaceted statistical study of all available data on solar activity during the Maunder minimum (1645–1715) is presented. The data include European telescope observations, Asian sunspot observations using the unaided eye, concentrations of cosmogeneous isotopes, and catalogues of polar aurorae. Joint analyses of data on the cosmogeneous isotopes ^{10}Be and ^{14}C are a promising source of information on solar activity in the past. The dates of relative sunspot maxima during the Maunder minimum are consistent with the idea that there were chaotic bursts of solar activity randomly distributed in time during this interval. The available evidence that the 11-year cyclicity was preserved in 1645–1715 are worthy of attention but require additional deep study and verification. No convincing evidence for a 22-year periodicity of the occurrence of sunspots during the Maunder minimum has been found.

1. INTRODUCTION

Since the well-known work of Eddy [1], the period 1645–1715 when sunspots were nearly absent, known as the Maunder minimum (MM), has attracted the attention of numerous researchers. The existence of such anomalous epochs in solar activity shows that the physical nature of this activity remains incompletely understood. It is obvious that deep and multifaceted studies of such periods can help elucidate the origin of solar cyclicity and mechanisms for the formation of sunspots. The question of whether any short-timescale (11–22 year) periodicity was present during the MM is very important. Since such short-period cycles in the occurrence of sunspots are associated with the dynamo mechanism, we can establish whether the dynamo mechanism continued to operate during the MM. In turn, this is extremely important for our understanding of global solar-activity minima.

There is no consensus about the behavior of the solar activity during the MM, and the various views on this question can be divided into three groups.

(1) Eddy [1] believed that the 11-year variation in the solar activity was absent during the MM. This conclusion was supported by the results of [2], which showed that the number of sunspot groups (NSG) recovered by Hoyt and Schatten [3] was not periodic.

(2) However, a number of other works argue that the 11-year cycle (the Schwabe cycle) was present during the MM. For example, this conclusion is supported by studies of catalogs of polar aurorae [4] and data on the concentrations of the cosmogeneous isotope ^{10}Be detected in Greenland ice cores [5]. Data on the concentrations of radioactive carbon ^{14}C in tree rings [6] are also consistent with the presence of 11-year periodicity in the solar activity during the MM. The time behavior of the solar activity starting from 1576 was recovered in [7] via a joint analysis of data on ^{10}Be, ^{14}C, and nitrates in layers of the Earth, and a clear 11-year cyclicity during the MM was revealed.

(3) A new approach to studying the solar activity in 1645–1715 was presented in [8, 9]. Analysis of NSG data [3] using a new original technique demonstrated that a 22-year periodicity (the Hale cycle) was present during the entire MM period. Usoskin, Mursula, and Kovaltsov [8, 9] found support for their conclusion in data on polar aurorae and the ^{14}C concentration in tree rings, and especially in the data of [10–12], which detected such 22-year variations twenty years ago. The analysis of radiocarbon series presented in [6] also shows evidence for 22-year periodicity during the MM [13].

Our work continues studies of solar activity during the MM using various direct and indirect solar-activity indicators. European telescope observations and observations using the unaided eye carried out by Asian (mainly Chinese) astronomers are considered direct indicators. We use the series of Hoyt and Schatten [3] for the European data and the catalog of Wittmann and Xu [14] for the Asian data. We use data on the cosmogeneous isotopes (^{10}Be and ^{14}C) and polar aurorae [5, 6, 15, 16] as indirect data.

1063-7729/03/4706-0517$24.00

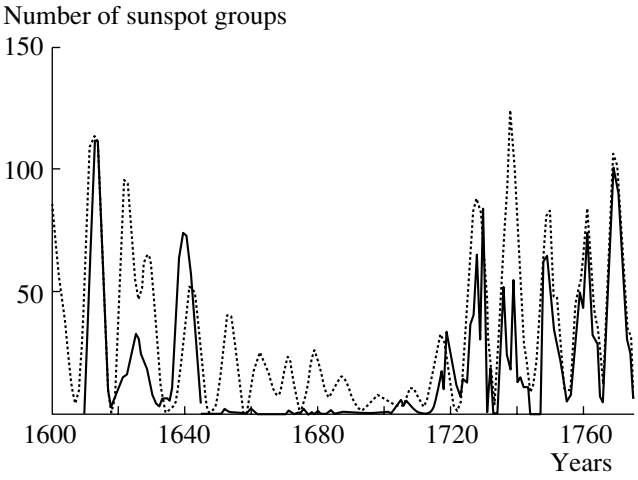

Fig. 1. The solid curve shows the number of sunspot groups according to Hoyt and Schatten [3]. The NSG reconstruction [8] is used before 1645. The dashed curve shows the Wolf numbers recovered in [7] using concentrations of cosmogeneous isotopes and nitrates.

2. THE MAUNDER MINIMUM AND 11-YEAR VARIATIONS IN SOLAR ACTIVITY

The 11-year variations in the MM are most clearly manifest by the concentrations of cosmogeneous isotopes. This periodicity is expressed by radioactive carbon comparatively weakly [6] and much more strongly by beryllium [5]. Nagovitsyn and Ogurtsov [7] reconstructed the Wolf numbers beginning from 1576 based on data on the concentrations of ^{14}C, ^{10}Be, and nitrates (NO_3^- ions) in various layers of the Earth using a specially developed complex, joint wavelet analysis of these data. This analysis assumes that two components are present in each temporal series: a component that is common to all series, associated with the solar modulation (the useful signal) and a noise component that is specific to each series. In this case, averaging several series can suppress the noise and strengthen the useful signal. This reconstruction is presented in Fig. 1 together with the NSG series of [3].

There are numerous gaps in the series of Hoyt and Schatten [3] before 1645. Therefore, for 1610–1645, we have used the NSG reconstruction presented in [9] instead of the original series [3]. Here, two facts are striking.

(1) The Wolf numbers recovered using the cosmogeneous isotope and nitrate data agree well with the actual NSG data during periods of normal solar activity. For example, the correlation coefficient for 1610–1645 is 0.4. For comparison, dendroclimatological correlation coefficients between reconstructed tree-ring temperatures and experimentally measured temperatures reach 0.3–0.5 [17]. The agreement obtained testifies that the competent use of all available indirect data can be useful in studies of solar activity in the past, at least during epochs of normal activity.

(2) The solar activity reconstructed for the MM [7] differs qualitatively from the Hoyt–Schatten series [3]. In fact, the Wolf numbers reconstructed for 1645–1687 reveal a strong cycle with a period of 8–10 yrs (Fig. 1), with the maximum Wolf number reaching 25–40. At the same time, European telescope observations [3] suggest the nearly complete absence of solar activity.

Given the extensive work on identifying and studying historical sources carried out by Hoyt and Schatten [3], it is difficult to imagine that the real NSG during the MM could reach 25–40. Therefore, the results concerning solar activity during the MM presented in [7] appear to be overestimated. The strong 12–15 year variation in one of the sources used in [7] (^{10}Be) is the most probable reason for this. Indeed, according to [5], the amplitude of the quasi-11-year variation of the beryllium concentration during the MM was as high as during periods of normal solar activity. This peculiarity of the ^{10}Be concentration was studied in [9], taking into account the fact that the beryllium record can be strongly distorted by climatic effects, especially during deep solar minima. Therefore, the 8–10 year periodicity clearly established for the recovered Wolf numbers during the MM may reflect not so much the corresponding solar cycle, as climatic effects in the concentration of ^{10}Be, and possibly ^{14}C. As regards the Schwabe cycle in the polar-aurora data [4, 15], it was shown in [9] that, during the MM, these temporal series display a 22-year rather than 11-year periodicity. Thus, the suggestion that the the 11-year variation in sunspot occurrence was preserved during 1645–1715 can be considered a hypothesis requiring additional verification.

3. THE MAUNDER MINIMUM AND 22-YEAR VARIATIONS IN SOLAR ACTIVITY

It was quite reasonably concluded in [8, 9] that the telescope observations of sunspots made in the seventeenth century were not sufficiently reliable. Therefore, instead of the original NSG series, Usoskin, Mursula, and Kovaltsov [8, 9] used the number of days when sunspots were observed—i.e., the NSG series for 1645–1715—transformed into the binary form

$$\begin{cases} S(t) = 1, \text{if at least one spot was observed on day } t, \\ S(t) = 0, \text{if no spots were observed on day } t. \end{cases} \quad (1)$$

This binary series was then processed using a specialized original technique, and the frequency of days with observed sunspots was analyzed. This enabled Usoskin, Mursula, and Kovaltsov [8, 9] to do the following:

(1) Clearly determine time intervals in which sunspots were observed (1652–1662, 1672–1689) and totally absent (1645–1651, 1663–1671, 1690–1695).

(2) Determine the dates of absolute maxima of solar activity during the MM, i.e., 1658 and 1679/1680. The first solar-activity maximum before the MM (1639/1640) and the last maximum at the very end of the MM (1705) were dated in [8] using original NSG data.

According to [8, 9], the alteration of relatively active periods (sunspots appear, though rarely) and periods of zero solar activity (sunspots are totally absent), and especially the sequence of the solar-activity maxima 1639/1640, 1658, 1679/1680, and 1705 convincingly confirm the presence of a 22-year variation in the occurrence of sunspots during the MM.

Note that the Hoyt–Schatten data [3] are not a unique source of information on sunspots during 1645–1715. Observations using the unaided eye carried out by Chinese and Korean astronomers provide another important source that should not be neglected, since telescope observations of the Sun were irregular in the seventeenth century. According to [18], European solar observations before the middle 1680's were probably no more frequent than 200–250 days per year. The number of days with solar observations [18] (the so-called "best estimate") is presented in Fig. 2a. Figure 2b compares the MM solar-activity data obtained by European and Asian astronomers.

Figure 2 shows that, in 1645–1651 and 1663–1671, when European astronomers did not report any sunspots at all, Asian astronomers reported observing sunspots ten times (five in 1645–1651 and five in 1663–1671). For example, Asian astronomers observed sunspots four times in 1665, while European astronomers observed the Sun on fewer than 180 days that year (Fig. 2a). The only European astronomer to observe the Sun during most of the period from 1645–1651 was Jan Hevelius [19]. Although there is no doubt of Hevelius' competence, it is known that he missed 4 of 24 sunspot groups that were present during his observations [19]. Taking these factors into account, Hoyt and Schatten [3] questioned the trustworthiness of sunspot data acquired in 1642–1653. It is evident that the European observations of sunspots in 1663–1671 and 1645–1653, used in [8, 9] to conclude that there was a complete absence of sunspots during these periods, are fragmentary and not fully reliable. Therefore, the record of five sunspot observations with the unaided eye (SOUE) in 1663–1671 and five in 1645–1651 can be considered a serious argument against the conclusion that there was zero

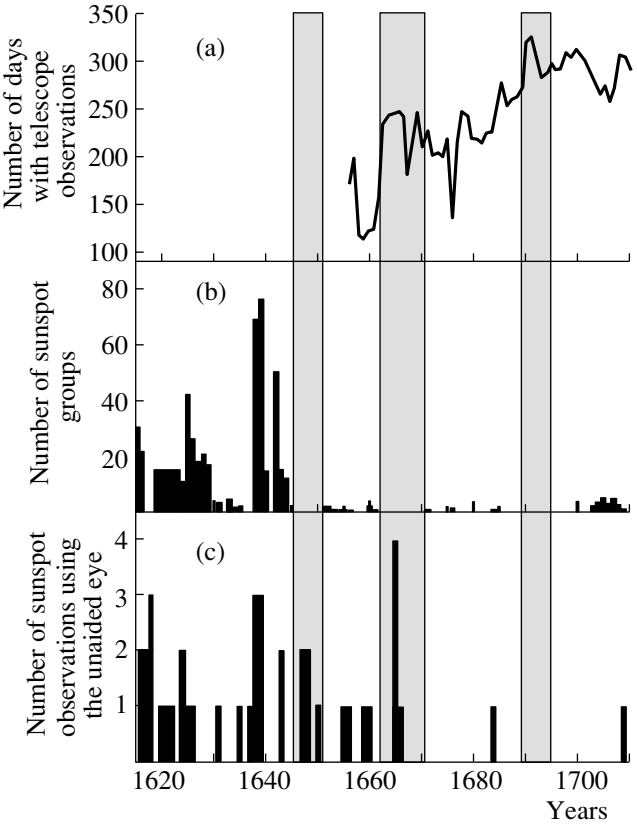

Fig. 2. (a) Number of days per year when the Sun was observed by European astronomers using telescopes [17]. (b) Annual mean number of sunspot groups [3]. (c) Annual number of sunspot observations using the unaided eye [13]. The gray color indicates the time intervals when there were no spots on the Sun, as follows from the data of European observers.

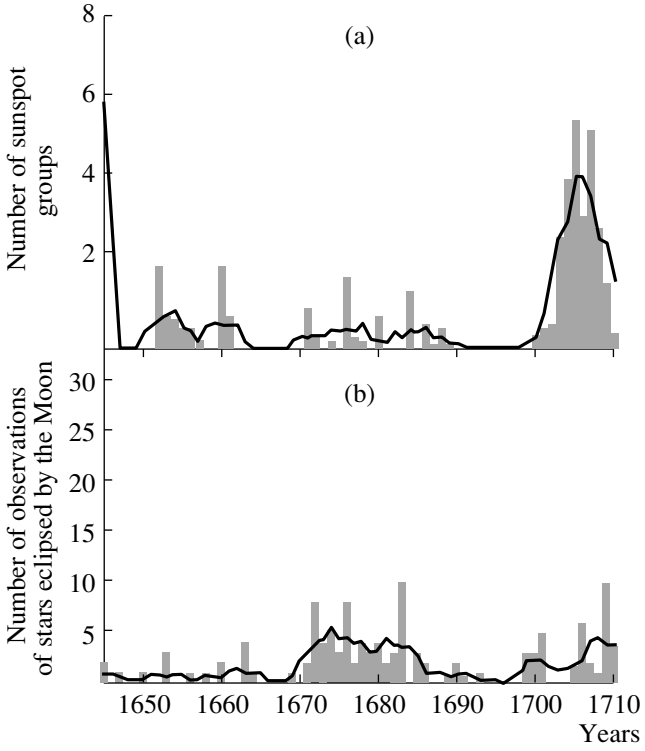

Fig. 3. (a) Annual mean number of sunspot groups [3]. (b) Annual mean number of observations of stars eclipsed by the Moon [23]. The histograms show the original data, and the solid curves the data smoothed over five points.

solar activity during these intervals. It was shown in [20] that the SOUE data contain information about global minima and maxima of the solar activity, as well as on the secular and 11-year solar cycles. On the other hand, we know that Asian astronomers could potentially confuse real sunspots with clouds, flocks of birds, etc. [14]. A comparison of Asian SOUE data with European telescope observations for the period 1848–1918 shows that only one-third of the Asian observations are confirmed by the European data [14]. The probability that at least one of the five SOUE of 1645–1651 or 1663–1671 corresponds to a real sunspot can be easily estimated:

$$P(5) = 1 - 0.66^5 = 0.88. \qquad (2)$$

The probability that at least one of these ten SOUE corresponds to a real sunspot becomes 0.985. If there were sunspots visible to the unaided eye in 1645–1651 and 1663–1671, this means that solar activity was comparatively high during these periods. According to the estimates of [21], in order for a sunspot to be visible to the unaided eye, the spot must have a large area exceeding 1900 μ h. As a rule, such large sunspots appear during periods of high solar activity. According to [22], the daily-average Wolf number must be no lower than 50 in order for such a sunspot to arise. Therefore, if there was at least one sunspot visible to the unaided eye in 1645–1651 and 1663–1671, the daily-average Wolf number reached 50 or more at least once during these intervals. According to [23], the maximum daily-average NSGs recorded in the entire interval 1645–1715 were 59 (April 1, 1652) and 47 (September 19, 1654). This means that, during 1645–1651 and 1663–1671, the solar activity at least occasionally reached a level comparable to the maximum level over the entire MM. Therefore, we can argue that the conclusion of [8, 9] that there was zero solar activity during 1645–1651 and 1663–1671 is in contradiction with the observations of Asian astronomers and requires additional verification.

Usoskin, Mursula, and Kovaltsov [8, 9] believed that the solar activity of 1652–1662 and 1672–1689 was comparatively high. This opinion is not undoubted, at least for the interval 1672–1689. Although detections of sunspots by European astronomers were more frequent during that period, there are no convincing arguments for a real growth in the solar activity. Let us consider the European observations of stars eclipsed by the Moon collected by Stephenson [24] (Fig. 3b).

Of course, the eclipsing of stars by the Moon is by no means related to sunspots. On the other hand, these events were frequently reported by the same astronomers who observed sunspots. Their reports on stars eclipsed by the Moon and on sunspots were also frequently published together [24]. It is therefore important that the interval 1672–1689 is a period of more frequent reports of occurrences of both sunspots and of stars eclipsed by the moon, with the latter phenomenon being reported more often (Fig. 3b). This indicates a growth in the activities of astronomers in 1672–1689. This increase in activity could reflect both an increase in the number of observations carried out and improvement in their quality, i.e., in the care with which observations were conducted and in the targetedness and accuracy of the observations themselves. Therefore, an increase in the number of reports of sunspots during this period may reflect a growth in the activities of European astronomers rather than any real increase in the number of sunspots. It is worth noting that the Asian sources indicate no increase in the number of sunspots in 1672–1689 (Fig. 2c).

Among the main arguments proposed in [8, 9] in favor of the idea that the Hale cycle was maintained during the MM is a sequence of absolute solar-activity maxima in [8, 9] 1640, 1658, 1680, and 1705. However, when comparing their data with those of other researchers [3, 25, 26], Usoskin, Mursula, and

Kovaltsov [9] use a quite different sequence of SA maxima obtained for another order of their statistical technique: 1640, 1654, 1660, 1677, 1684, 1695, and 1705. Thus, in [8, 9], one sequence of solar-activity maxima (1640, 1658, 1680, and 1705) is used to verify the 22-year variations, while another sequence (1640, 1654, 1660, 1677, 1684, 1695, and 1705) is used to compare their results with those of other authors. This approach seems questionable and requires additional justification. Note that the sequence 1640, 1658, 1680, and 1705 does, indeed, appear to indicate a 22-year variation, but the dates 1658 and 1680 do not well agree with the data of [3, 25, 26]. On the contrary, the sequence 1640, 1654, 1660, 1677, 1684, and 1705 agree well with the data of [3, 25, 26] but do not give any hint of a 22-year periodicity.

Usoskin, Mursula, and Kovaltsov [9] cite the radiocarbon series obtained by American [6] and Soviet [10, 12] researchers as support for their hypothesis that the 22-year variation was present. However, their conclusion that the behavior of the ^{14}C concentration and the solar activity are in agreement in 1645–1715 is based on an analysis of data covering only three to four Hale cycles [9]. It was shown in [34] that the consistency between the individual solar-activity and radiocarbon cycles is fairly crude, due to the relatively large uncertainties in $\Delta^{14}C$ and distortions introduced by a 15–30 year variation of nonsolar origin (attributed in [28] to regional climatic changes). We expect that the relative contribution of this latter variation increases during periods when the 11-year solar-activity cycle is suppressed. Therefore, applying data on the ^{14}C concentration to studies of the occurrence of sunspots is less promising for the MM. In any case, it is clear that any conclusions about a solar modulation of $\Delta^{14}C$ would be justified only by a joint analysis carried out for many solar and radiocarbon cycles. It remains unclear whether three cycles are sufficient for this purpose. Nevertheless, we will continue with our consideration of the study of [9]; the radiocarbon series [6, 10–12] are presented in Figs. 4b and 4c.

Figure 4 shows that these two series are not in good agreement. The most prominent disagreement is in the variation amplitudes. The amplitude of the short-period ($T < 30$ yrs) variations in the series of [6] does not exceed 4–5‰, while the amplitude of the variations in [10–12] reaches 20‰, or a factor of four greater. This striking difference requires some explanation before proceeding to any joint analysis of these experimental series. Some ideas concerning this question can be found in [27, 29], although the problem remains unsolved.

It is well known that some properties of the carbon recirculation system result in a time delay between

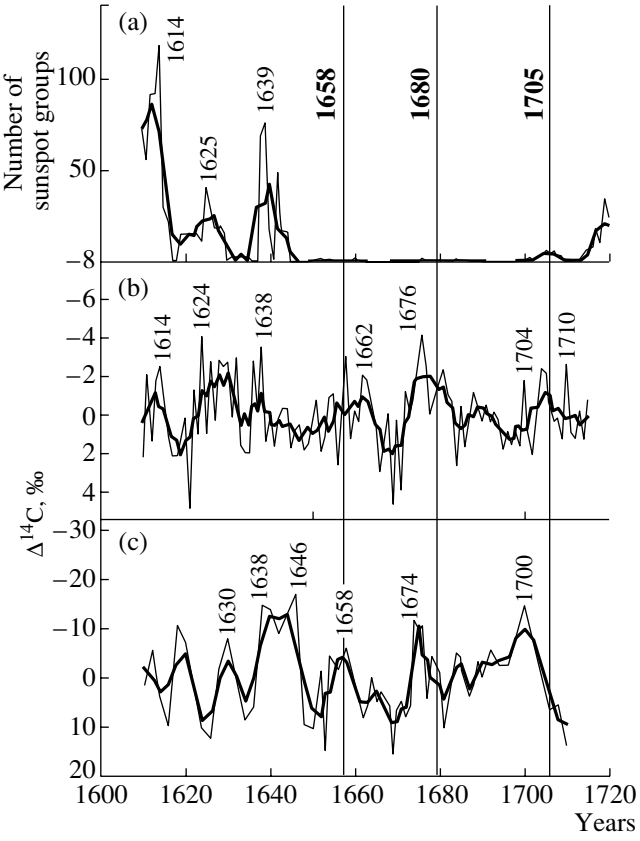

Fig. 4. (a) Annual mean number of sunspot groups. The radiocarbon concentration in tree rings (b) of [6] and (c) of [10–12], with the third order trend eliminated. The thin curves show the original data. The thick curves show the data smoothed by five (a, b) and three (c) points. The thin vertical lines mark dates of relative solar-activity maxima [8, 9].

variations of the cosmic-ray intensity and the tropospheric ^{14}C concentration. In the case of the 11-year variations, this phase shift is about two to four years, according to the theoretical estimates [30, 31] and the experimental measurements of [6, 32]. The delay should be longer for the 22-year variations. However, Fig. 4 shows that most of the $\Delta^{14}C$ minima in both radiocarbon series lead the solar-activity maxima determined in [8, 9] (1658, 1680, and 1705) by one to four years, instead of lagging them by two to four years. Thus, the phase shift between the solar-activity maxima determined in [8, 9] and the ^{14}C minima derived in [6, 10, 12] does not reveal any cause–effect relationship between these two phenomena.

This is also true of the $\Delta^{14}C$ amplitude for 1645–1715. Figure 4b shows that the amplitude of the 18-year fluctuation in 1660–1678 [6] reaches 4‰. It is well known that the carbon recirculation suppresses high-frequency fluctuations in the ^{14}C concentration.

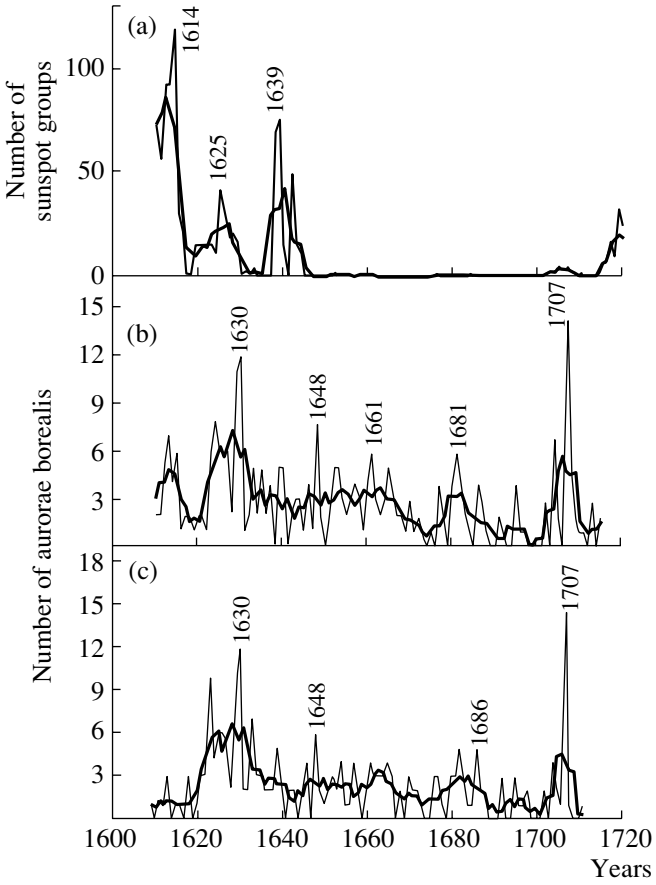

Fig. 5. (a) Annual mean number of sunspot groups [3]. Annual number of polar aurorae according to (b) [14] and (c) [15]. The thin curves show the original data, and the thick curves the data smoothed over five points.

The attenuation coefficient for the 22-year variations is about 50 [30, 31]. This means that the 4‰ oscillation in the tropospheric radiocarbon Q is due to a 20% fluctuation of the carbon production in the atmosphere. The change in the intensity of Galactic cosmic rays required for this fluctuation of Q can easily be estimated using the formula [11]

$$\Delta I = -4.2 \times \Delta Q^{0.78}, \qquad (3)$$

where ΔI is expressed in percents of 3854 m^{-2} s^{-1} steradian^{-1} and ΔQ is expressed in 2.54 atoms cm^{-2} s^{-1} (the average I and Q for 1890).

For $\Delta Q = 20\%$, formula (1) yields a peak-to-peak ΔI variation of 40%. This is a strong variation, comparable to the variation of the Galactic cosmic-ray intensity during the usual Schwabe cycle. Let us estimate the Wolf-number variation that can give rise to a 20% fluctuation in Q in the framework of the diffusion-modulation mechanism. According to [33], the Wolf numbers of the current epoch are related to the ^{14}C production rate via the formula

$$Q = 2.091 - 0.0041W, \qquad (4)$$

where Q is in atoms cm^{-2} s^{-1}.

Formula (2) shows that a Q variation of 20% corresponds to a Wolf-number fluctuation with an amplitude of 100. The parametrization [34] yields the even higher amplitude of 150 for the Wolf-number variation. Consequently, the variations of the ^{14}C concentration during 1660–1678 presented in [6] could result from a Wolf-number variation with an amplitude of 100–150. However, the fluctuations of the mean annual NSG during the MM did not exceed two to four, which is almost two orders of magnitude lower. It is difficult to imagine that such weak oscillations in the sunspot occurrence could be associated with the 4‰ variation of the radiocarbon concentration. Note that the $\Delta^{14}C$ amplitudes are even higher in the Soviet data. This led the Soviet researchers [10–12] to invoke the drift mechanism for the modulation of $\Delta^{14}C$ by solar activity to explain the 22-year radiocarbon variations. The drift mechanism, which is associated with the repolarization of the interplanetary magnetic field every 22 yrs, can give rise to Galactic cosmic-ray variations of 20–30% [12] during periods of extremely low solar activity. However, it is difficult to attribute the 22-year $\Delta^{14}C$ variations with repolarization of the total solar magnetic field, i.e., to argue that the 22-year magnetic cycle was preserved during the MM, since the 15–30 year variations in the ^{14}C concentration noted above, which are not associated with the solar modulation, can strongly distort radiocarbon variation of solar origin.

Usoskin, Mursula, and Kovaltsov [9] used catalogs of polar aurorae [4, 15] as additional evidence supporting the presence of 22-year variations of the solar and heliospheric activity during the MM. These data are presented in Fig. 5 (we use the augmented data of [16] instead of those in [4]). Figure 5 shows that the agreement between the Hoyt–Schatten series [3] and the auroral data is poor for the seventeenth century. The strong solar-activity cycle of 1610–1618 was only weakly manifest in the auroral activity and the moderate cycle of 1635–1648 was not manifest at all, while the weak cycle of 1619–1634 was responsible a significant growth in the number of polar aurorae. The feeble solar cycle of 1700–1713 likewise gave rise to an appreciable growth in auroral activity. This provides evidence that the number of polar aurorae in the seventeenth century was only weakly dependent on the number of sunspots. Note also that the maximum auroral activity was reached in 1648, when the Sun, according to [8, 9], was in an absolute minimum and sunspots were totally absent. Thus, the catalogs of polar aurorae [4, 15, 16] likewise do not

support the hypothesis of [8, 9]. Consequently, the general conclusion of [9] that there were similar 22-year variations of the solar activity, auroral activity, and Galactic cosmic-ray intensity during the MM does not appear to represent the real situation.

In our opinion, the most conclusive finding of [8, 9] is the sequence of solar-activity maxima in 1640, 1654, 1660, 1677, 1684, 1695, and 1705. As was noted in [9], these dates agree with the data of [3, 25, 26] obtained independently by other researchers using other methods. Therefore, this sequence seems to be the most reliable estimate available of the dates of maximum solar activity during the MM. This sequence of maxima was analyzed for the presence of hidden periodicity [36] using the statistic of Sherman [37, 38]. The average time interval between the solar-activity maxima is 10.8 yrs, and the corresponding value of the Sherman statistic is 0.83. The significance of the effect was estimated using the diagram in Fig. A3 of [39]. The value of 0.83 corresponds to a probability of the null hypothesis (no periodicity) being correct exceeding 0.9. This means that, although the sequence of maxima in 1640, 1654, 1660, 1677, 1684, 1695, and 1705 contain a hint of the 11-year periodicity, it should be viewed simply as reflecting fluctuations in solar activity randomly distributed in time.

4. CONCLUSIONS

We have shown that analyses of the concentrations of cosmogeneous isotopes are promising as a source of information on solar activity during normal intervals. However, reconstruction of solar activity using cosmogeneous isotopes becomes difficult during global minima. Our analysis of solar activity using all direct and indirect data available for the Maunder minimum shows that it remains difficult to answer the question of whether or not the solar-activity cyclicity was maintained in this period. It is most probable that the dates of solar-activity maxima during 1645–1715 correspond to weak peaks in solar activity that are randomly distributed in time. The numerous indications that the 11-year periodicity was maintained during 1645–1715 require additional careful, multifaceted studies. We have found no convincing evidence for the presence of 22-year variations in the occurrence of sunspots during the Maunder minimum.

5. ACKNOWLEDGMENTS

This work was carried out in the framework of a program of scientific exchange between the Russian and Finnish Academies of Sciences (project no. 16) and supported by INTAS (2001-0550) and the Program of the Presidium of the Russian Academy of Sciences "Astronomy: Nonstationary Processes in Astronomy."

REFERENCES

1. J. A. Eddy, Science **192**, 189 (1976).
2. P. Frick, D. Galyadin, D. Hoyt, *et al.*, Astron. Astrophys. **338**, 670 (1997).
3. D. V. Hoyt and K. Schatten, Sol. Phys. **179**, 189 (1998).
4. W. Schröder, J. Geomagn. Geoelectr. **44**, 119 (1992).
5. J. Beer, S. Tobias, and N. Weiss, Sol. Phys. **181**, 237 (1998).
6. M. Stuiver and T. F. Braziunas, Holocene **3**, 289 (1993).
7. Yu. A. Nagovitsyn and M. G. Ogurtsov, Izv. GAO **215**, 271 (2000).
8. I. G. Usoskin, K. Mursula, and G. A. Kovaltsov, Astron. Astrophys. **354**, L33 (2000).
9. I. G. Usoskin, K. Mursula, and G. A. Kovaltsov, J. Geophys. Res. **106** (A8), 16039 (2001).
10. V. A. Vasil'ev and V. A. Dergachev, Izv. Akad. Nauk SSSR, Ser. Fiz. **45**, 1180 (1980).
11. V. A. Vasil'ev and G. E. Kocharov, in *Proceedings of XIII Leningrad Seminar on Space Physics, Leningrad, Russia, 1983,* p. 75.
12. G. E. Kocharov, V. M. Ostryakov, A. N. Peristykh, and V. A. Vassil'ev, Sol. Phys. **159**, 381 (1995).
13. A. N. Peristykh and P. E. Damon, Sol. Phys. **177**, 343 (1998).
14. A. D. Wittmann and Z. Xu, Astron. Astrophys., Suppl. Ser. **70** (1), 83 (1987).
15. L. Krivský and K. Pejml, Astron. Inst. Czech. Acad. Sci. **75**, 32 (1988).
16. W. Schröder, http://verplant.org/history-geophysics/Sun/Sun.htm.
17. P. D. Jones, K. R. Briffa, T. P. Barnett, and S. F. B. Telt, Holocene **8.4**, 455 (1998).
18. D. V. Hoyt and K. Schatten, Sol. Phys. **165**, 181 (1996).
19. D. V. Hoyt and K. H. Schatten, Sol. Phys. **160**, 371 (1995).
20. Yu. A. Nagovitsyn, Geomagn. Aeron. **41** (5), 711 (2001).
21. A. Wittmann, Astron. Astrophys. **66**, 93 (1978).
22. J. A. Eddy, F. R. Stephenson, and K. K. C. Yau, Q. J. R. Astron. Soc. **30**, 65 (1989).
23. ftp//ftp.ngdc.noaa.gov/STP/SOLAR_DATA/SUNSPOT_NUMBERS/GROUP_SUNSPOT_NUMBERS
24. R. R. Stephenson, Philos. Trans. R. Soc. London **A330**, 499 (1990).
25. M. Waldmeier, *The Sunspot Activity in the Years 1610–1960* (Zurich Schulthess, Zurich, 1960).
26. B. Mendoza, Ann. Geophys. **15**, 397 (1997).
27. G. E. Kocharov, Nuovo Cimento **19** (6), 883 (1996).
28. S. S. Vassil'ev, G. E. Kocharov, and M. G. Ogurtsov, Izv. Ross. Akad. Nauk, Ser. Fiz. **61** (6), 1224 (1997).
29. A. N. Konstantinov, A. M. Krasil'shchikov, V. E. Lazarev, and I. B. Mikheeva, Izv. Ross. Akad. Nauk, Ser. Fiz. **61** (6), 1242 (1997).
30. G. E. Kocharov, *Astrophysical Phenomena and Radiocarbon Concentrations in Terrestrial Samples* [in Russian] (FTI, St. Petersburg, 1996).

31. V. A. Dergachev and V. S. Veksler, *Application of the Radiocarbon Method to Studies of the Past Environment* [in Russian] (Leningrad, 1991).
32. P. E. Damon, A. Long, and E. I. Wallick, Earth Planet. Sci. Letters **20**, 300 (1973).
33. M. Stuiver and P. D. Quay, Science **207** (4426), 11 (1980).
34. K. O'Brien, J. Geophys. Res. **84** (A2), 423 (1979).
35. Yu. A. Rivin, Geomagn. Aeron. **38**, 183 (1998).
36. M. G. Ogurtsov, Preprint No. 1754 (A. F. Ioffe Physico-Technical Institute, Russian Academy of Sciences, Moscow, 2001).
37. B. Sherman, Ann. Math. Stat. **21**, 339 (1950).
38. D. R. Cox and P. A. Lewis, *The Statistical Analysis of Series of Events* (Methuen, London, 1966).
39. W. J. Burroughs, *Weather Cycles: Real or Imaginary* (Cambridge Univ. Press, Cambridge, 1994).

Translated by V. Badin

Astronomy Reports, Vol. 47, No. 6, 2003, pp. 525–530. Translated from Astronomicheskiĭ Zhurnal, Vol. 80, No. 6, 2003, pp. 571–576.

The Empirical Melchior Laws and Parametric Excitation of the Chandler Wobble

G. S. Kurbasova[1], L. V. Rykhlova[2], and G. N. Shlikar'[1]

[1] *Crimean Astrophysical Observatory, Nauchnyi, Crimea, Ukraine*

[2] *Institute of Astronomy, Pyatnitskaya 48, Moscow, 109017 Russia*

Received June 20, 2002; in final form, November 27, 2002

Abstract—Models of the motion of the terrestrial reference frame with respect to an inertial frame can describe the motions of the Earth–Moon system, which are traditionally separated into precession, nutation, the polar motion, and rotation about the Earth's axis. Existing theoretical models do not describe variations in the Earth-orientation parameters with the required accuracy, so that the current polar coordinates and duration of the day must be determined from observations. To improve theoretical models for the time dependence of the coordinates of the Earth's pole, we examine the possible excitation of the Chandler wobble due to internal properties of the Earth–Moon system. A differential equation describing the parametric resonance in the Earth–Moon system is obtained for the first region of the parametric excitation. The solution of this equation analytically describes the finite amplitudes of the nonlinear conservative system. The theoretical results are compared with the empirical laws of Melchior deduced from observational data on the coordinates of the Earth's pole. © *2003 MAIK "Nauka/Interperiodica"*.

1. INTRODUCTION

The growing accuracy of astronomical measurements and observational techniques increases our knowledge of interactions between celestial bodies and provides a firm basis for the definition of an inertial reference frame. The trustworthiness of interpretations of observational data depends appreciably on the accuracy with which a reference frame fixed to the Earth's body can be defined with respect to an inertial frame. Modeling the motion of the terrestrial reference frame with respect to the inertial frame describes the motion of the Earth–Moon system around the Sun together with the bodies' rotational motions; these motions are traditionally separated into precession, nutation, the polar motion, and rotation about the Earth's axis.

Modeling the dynamics of the Earth–Moon system is a special case of constructing a dynamical system of interacting celestial bodies governed by the three classical laws of Newtonian mechanics and the law of gravity. This results in a one-parameter (equal to the time of the motion) group of mappings based on a simple differential operator. However, studies of this operator give rise to sophisticated mathematical problems, such as the Earth's rotational motion and the three-body problem for the Sun, Earth, and Moon.

In a classical representation, these problems correspond to those for conservative mechanical systems governed by canonical Hamilton equations. Detailed consideration of this question shows that the classical forms of the equations do not take into account a number of features associated with coupled oscillations in the Earth–Moon–Sun system, which can sometimes lead to discrepancies between the modeled and real motions.

In a system of coupled bodies, the oscillations of the individual bodies change their forms. A model describing the most important and fundamental properties of coupled oscillations in the Earth–Moon system was proposed in [1–3]. This model enabled us to apply known analysis and calculation techniques. The analysis yielded a theoretical period for the natural oscillations of the Earth in the Earth–Moon system, with this period being equal to the mean Chandler period derived from observational data on the coordinates of the Earth's pole.

The fundamental kinematic features of oscillations are their period and amplitude. Two basic models for the Chandler wobble are encountered in the literature: the "damped" model and the varying-period model. Being a free motion, the Chandler oscillation ought to be damped, but astronomical observations over the last 150 yrs have given no indications of gradually decreasing amplitudes.

Numerous studies of the Chandler wobble (undertaken by Chandler, Kimura, Berg, Nicolini, Melchior, and others) have suggested that its period varies with in time. The variable period is related to the variable

1063-7729/03/4706-0525$24.00

amplitude in accordance with the empirical laws proposed by Melchior [4].

(1) The Chandler period fluctuates, with the maximum deviation from the mean being about ±4%.

(2) The period and amplitude of the Chandler wobble are proportional to each other, with the correlation coefficient being +0.88 (according to Nicolini).

(3) Increases in the Chandler period are correlated with small amplitudes of the annual motion.

The unambiguous physical interpretation of these laws requires that we understand the origins of the variations in the amplitude and period. Recently, attention has mainly been focused on atmospheric, seismic, and tidal forces associated with changes in the period and amplitude of the free oscillation of the structurally inhomogeneous Earth.

However, the source and excitation mechanism of this oscillation remain open to question. It is generally believed that any movable component of the Earth could be responsible for this oscillation, and it is usually easier to eliminate possibilities than to confirm them [5].

Our approach [3] to explaining the behavior of the amplitude and period of the Earth's free oscillations is based on the following assertions.

(1) The main origin of variations in the period and amplitude of the Earth's free oscillations in the Earth–Moon system is interactions between coupled oscillations and the physical properties of the system.

(2) The redistribution of energy involves all movable components of the Earth, including its atmosphere.

2. PARAMETRIC ACTION IN THE EARTH–MOON SYSTEM

The frequency ω_0 of the natural oscillations and the damping coefficient δ are determined solely by the physical properties of the system. An analysis of external actions on the Earth–Moon system must distinguish between force and parametric actions. Force actions do not change ω_0 and δ. Pure force actions can act only in the case of an ideal, linear, model of the Earth–Moon system. On the contrary, parametric actions change only ω_0 and δ.

For the real Earth–Moon system, which is fundamentally nonlinear, pure force and parametric actions cannot be separated, since the growing amplitude of either an external force or of forced oscillations will give rise to a nonlinear dependence of the energy-consuming parameter ρ on the instantaneous external force (ρ is the distance between the Earth's and Moon's centers of mass). Such an action can be considered hybrid, i.e., both force and parametric [6].

This circumstance severely complicates the analysis of forced actions in the nonlinear system, even in a conservative approximation, and limits the correctness of treatments of a direct force action that do not take into account the simultaneous parametric action on the system.

It thus seems reasonable that, when considering a purely parametric action on the amplitude and frequency of the Earth's natural oscillations in the Earth–Moon system, we should not contrast this with the case of a force, or direct, action.

To analyze a parametric action, we will classify actions according to various scenarios for inputting energy into the system, which is the most important factor for resonance phenomena.

In the case of a direct action, the direct work of external forces during the system's motion provides the energy of forced oscillations. In the case of a parametric action, increases in the oscillation energy are due to the transformation of energy from one form to another.

According to general parametric-resonance theory, a process with growing amplitudes that provides partial or full compensation for energy losses in a system can be realized via the periodic variation of the energy-consuming parameter, if there are certain relations between the frequency of this variation and the natural frequency of the system. In particular, the amplitude of natural oscillations at the frequency ω_0 can be recovered by analyzing the internal properties of the system.

The internal interaction reaches its maxima and minima when the Moon is at perigee and apogee, respectively. We can treat an elliptical motion with a small eccentricity as a free oscillation near the corresponding circle. Similarly, we can treat the real motion of the Moon as a free oscillation near an orbit with radius of curvature $\rho_0 = a$, where a is the mean distance between the Earth's and Moon's centers of mass, which corresponds to the mean motion n along the unperturbed orbit.

For small deviations of the Moon from the equilibrium motion, we can express the increment of the oscillation energy in the form

$$\Delta W = \frac{k}{2}\left(\frac{1}{\rho_0 - \Delta\rho} - \frac{1}{\rho_0 + \Delta\rho}\right), \qquad (1)$$

where $k = Gm_E m_M$, G is the gravitational constant, and m_E and m_M are the masses of the Earth and Moon, respectively.

Using the inequality $\Delta\rho \ll \rho_0$, we obtain from (1) the expression

$$\Delta W = W_0 \frac{2\Delta\rho}{\rho_0}, \qquad (2)$$

where W_0 is the potential energy of the Earth–Moon system for the equilibrium rotation.

The modulation depth for the parameter ρ is

$$m = \frac{\rho_{\max} - \rho_{\min}}{\rho_{\max} + \rho_{\min}}. \quad (3)$$

In (3), $m = e$; i.e., it is the eccentricity of the Moon's orbit.

Parametric excitation (parametric resonance) requires that there be a certain relation between the frequency ω_ρ of variations of the parameter ρ and the frequency ω of the excited oscillations.

The mathematical description of the periodic variation ρ_t with respect to ρ_0 takes the form

$$\rho_t = \rho_0/[1 + e\cos(2\omega t)], \quad (4)$$

where the frequency of the periodic variations ρ_t is $2\omega = \omega_\rho$, which, in turn, is determined by the expression

$$\omega_\rho = \frac{1}{2}\sqrt{(\omega_a^2 - \omega_c^2)/2}. \quad (5)$$

In this case, ω_a and ω_c are the cyclic frequencies of the anomalistic and synodic motions, respectively.

The periodic variations in the energy-consuming parameter ρ_t with the frequency ω_ρ excite an oscillation with the frequency $\omega \cong \omega_0$.

In the general theory of oscillations for a one-dimensional system, the parametric resonance is mathematically described by the differential equation

$$\ddot{\xi} + \varphi_1(t)\dot{\xi} + \varphi_2(t)\xi = 0, \quad (6)$$

where $\varphi_1(t)$ and $\varphi_2(t)$ are periodic functions of time.

Substituting $\xi = z\exp\left\{-\frac{1}{2}\int \varphi_1(t)dt\right\}$, we transform this equation into the Hill equation

$$\ddot{z} + \psi(t)z = 0, \quad (7)$$

where $\psi(t) = \varphi_2(t) - \frac{1}{2}\dot{\varphi}_1(t) - \frac{1}{4}\varphi_1^2(t)$ is a periodic function.

The Mathieu equation is a special case of the Hill equation:

$$\ddot{y} + \omega_0^2[1 + m\cos(\omega_\rho t)]y = 0, \quad (8)$$

where the ω_0, m, and ω_ρ in (8) are the same as above.

The general solution of this equation takes the form

$$\xi = c_1\chi(t)e^{\beta t} + c_2\chi(-t)e^{-\beta t}, \quad (9)$$

where $\chi(t)$ are restricted functions whose period is equal to the period of the variations of the energy-consuming parameter or to half this period, and the complex number β is the characteristic index. A complete analysis of solutions of the Mathieu equation is rather complicated for linear problems, and even more so for nonlinear ones.

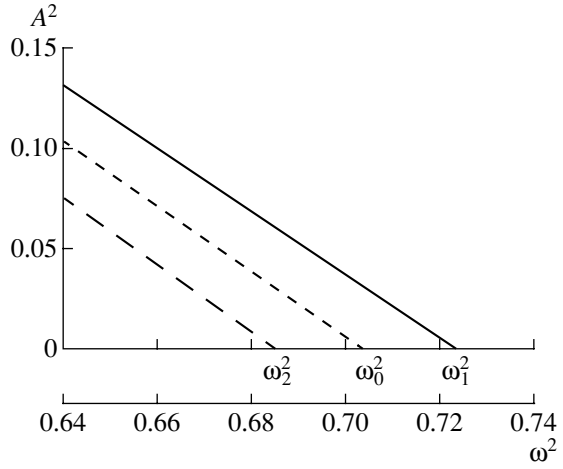

Fig. 1. The parametric resonance $A^2(\omega^2)$ for a conservative, nonlinear Earth–Moon system.

Let us consider only the most important features of the system, under assumptions that will enable us to correctly estimate the character of the parametric resonance for the important case when the natural frequency $\omega(t)$ differs only slightly from some constant value ω_0. In addition, we will take into account the nonlinear character of the oscillations of the energy-consuming parameter (4), which result in certain qualitatively new features of the motion.

Equation (8) then takes the form

$$\ddot{x} + \omega_0^2\,[1 + e\cos(2\omega t)]\,f(x) = 0, \quad (10)$$

where $f(x)$ is a function describing the nonlinear characteristics of the system. We will assume that

$$f(x) = x + \gamma x^3, \quad (11)$$

where the coefficient γ describes the degree of nonlinearity.

In accordance with the interconnected nature of the oscillations in the Earth–Moon system, we will assume

$$\gamma = \pm\sqrt{1 + (4\lambda)^2}/2, \quad (12)$$

where λ is the non-dimensional coupling coefficient for the Earth–Moon system [3].

For a given modulation depth e of the parameter ρ in (10), there are certain regions of ω near the frequencies $\omega_0/\omega = 1, 2, 3, ..., n$ in which the equilibrium motion becomes unstable, and oscillations with the frequencies ω, 2ω, 3ω, etc., should arise and grow in the system.

In our approximate analysis of (10), we will consider only the solution with the frequency ω corresponding to the first region of instability near $\omega = \omega_0$.

Boundaries of the first region of parametric excitation of the Chandler oscillation

e		0.0448	0.0549	0.0650
$P_0 = 433.4$ (days)	P_1, days	428.6	427.6	426.5
	P_2, days	438.3	439.4	440.6
$P_0 = 435.3$ (days)	P_1, days	430.5	429.4	428.4
	P_2, days	440.3	441.4	442.6

Let the approximate solution of (10) take the form

$$x = a\cos(\omega t) + b\sin(\omega t), \qquad (13)$$

that is, it is a steady-state oscillation with a frequency equal to half the frequency of the parametric action, which corresponds to the first region of the parametric excitation. In this case, the amplitude of the steady-state solution is $A = \sqrt{a^2 + b^2}$ and its phase is $\varphi = \arctan(a/b)$. Substituting (13) into (10), after some manipulations also using (11), we obtain the two coupled equations

$$\omega_0^2 a\left(1 + \frac{3\gamma}{4}A^2\right)\left(1 + \frac{1}{2}e\right) - a\omega^2 = 0, \qquad (14)$$
$$\omega_0^2 b\left(1 + \frac{3\gamma}{4}A^2\right)\left(1 - \frac{1}{2}e\right) - b\omega^2 = 0.$$

The solutions of these equations are the following.

(1) $a = b = A = 0$. There is no periodic steady-state motion. This is a possible equilibrium state. The real existence of such a state for the given parameters of the system and external actions is determined by the stability of this state.

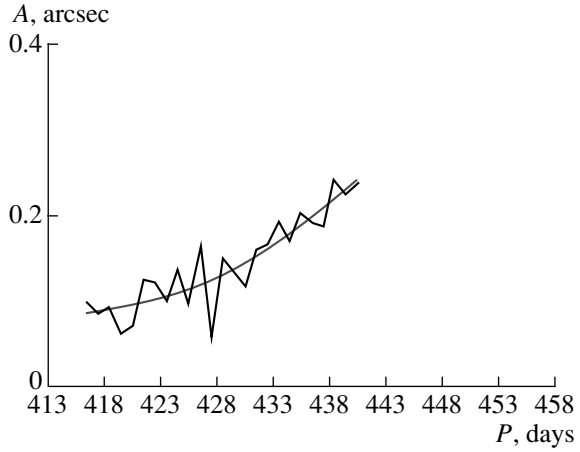

Fig. 2. Mean amplitudes of the Chandler wobble.

(2) Taking $a \neq b$ and $b = 0$, we obtain

$$\omega_0^2\left(1 + \frac{3\gamma}{4}A^2\right)\left(1 + \frac{1}{2}e\right) = \omega^2, \qquad (15)$$

whence

$$A^2 = \frac{4}{3\gamma}\left[\frac{\omega^2}{\omega_0^2\left(1 + \frac{e}{2}\right)} - 1\right]. \qquad (16)$$

The amplitude A is real ($A^2 > 0$) for $\gamma > 0$ only if $\dfrac{\omega^2}{\omega_0^2(1 + e/2)} - 1 > 0$, that is, if $\omega/\omega_0 > \sqrt{1 + e/2}$, $\omega > \omega_1 = \omega_0\sqrt{1 + e/2}$.

(3) When $a = 0$ and $b \neq 0$, the second equation of (14) yields

$$A^2 = \frac{4}{3\gamma}\left[\frac{\omega^2}{\omega_0^2\left(1 - \frac{e}{2}\right)} - 1\right], \qquad (17)$$

which means that the condition for a real solution is $\omega/\omega_0 > \sqrt{1 - e/2}$, $\omega > \omega_2 = \omega_0\sqrt{1 - e/2}$.

When $\gamma < 0$ (the mean frequency decreases with amplitude), the steady-state amplitude takes the form

$$A^2 = \frac{4}{3|\gamma|}\left[1 - \frac{\omega^2}{\omega_0^2(1 \pm e/2)}\right]. \qquad (18)$$

(4) When $a \neq 0$ and $b \neq 0$, Eqs. (14) are inconsistent.

Let us represent the amplitude (18) graphically. Figure 1 shows the amplitude A^2 (18) as a function of ω^2. The frequencies ω_1 and ω_2 correspond to the boundaries of the first region of parametric excitation of free oscillations. These frequencies were obtained from the condition that there be a real solution of (14), and have the form

$$\omega_1 = \omega_0\sqrt{1 + e/2}, \qquad (19)$$
$$\omega_2 = \omega_0\sqrt{1 - e/2}.$$

The table presents the boundaries (the periods P_1 and P_2) of the first region of parametric excitation for two mean periods of the Chandler wobble P_0 and for three eccentricities of the Moon's orbit e. The mean value $P_0 = 433.4$ days is calculated for the case when the frequency ω of the excited oscillations is equal to the natural frequency ω_0; that is, $\omega_\rho = 2\omega_0$, in accordance with (5). The mean value $P_0 = 435.3$ days is obtained from a statistical analysis of data on the coordinates of the Earth's pole obtained over the last 100 years.

The table shows that the widths of the interval of variations in the mean period as a result of the parametric excitation are 2.2, 2.7, and 3.3% for the three eccentricities.

Taking into account the dissipation and amplitude deformations resulting from the forced processes can broaden somewhat the interval of changes in the mean period.

We can describe the behavior of the system for the case of a parametric action with a given modulation depth e as follows. The presence of oscillations with their frequency ω falling in the interval $\omega_1 - \omega_2$ gives rise to an oscillatory process with a finite amplitude A that depends on the degree of nonlinearity γ.

Due to the anisochronic nature of the system, in the presence of parametric excitations, the natural frequency varies with growth in the amplitude, and the system moves to the boundary of the corresponding region of parametric excitation. This leads to a decrease in the energy contributed by the system to changes in ρ and limits the growth in the amplitude of the natural oscillations with the frequency ω_0.

Let us compare our theoretical conclusions with a numerical analysis of the coordinates of the pole derived from observational data obtained over the last century.

3. DISCUSSION OF THE RESULTS

We considered the coordinates of the pole x_i and y_i averaged over 5-day intervals from 1900 to 1998. The technique for the linear combination of exponential functions [7] was applied to the data after they were transformed into complex form.

Figure 2 presents the Chandler amplitude as a function of the oscillation period. The parameters of the models were determined in intervals of 18 yrs, with a time shift of 0.25 yrs. The plot in Fig. 2 was constructed by averaging the amplitudes for a single period. The Chandler amplitude increases with increasing period (decreasing frequency), in good agreement with the theoretical conclusions for $\gamma < 0$ and with the first and second empirical laws of Melchior.

The deviations from the mean period ($P = 435$ days) were 1.15% toward increasing and about 4% toward decreasing periods (Fig. 2). At the same time, for the case of a "pure" parametric excitation (see table), the maximum deviation from the mean does not exceed 1.7% when the asymmetry is no more than 0.1%.

In the interval 428–442 days, the deviation from the mean period is 1.7% toward increasing and 1.6% toward decreasing periods, in full agreement with the period distribution presented in the table.

Changing the duration H of the time interval used to determine the model parameters from 9 yrs to 18 yrs does not change the character of the interrelation between the Chandler amplitude and period.

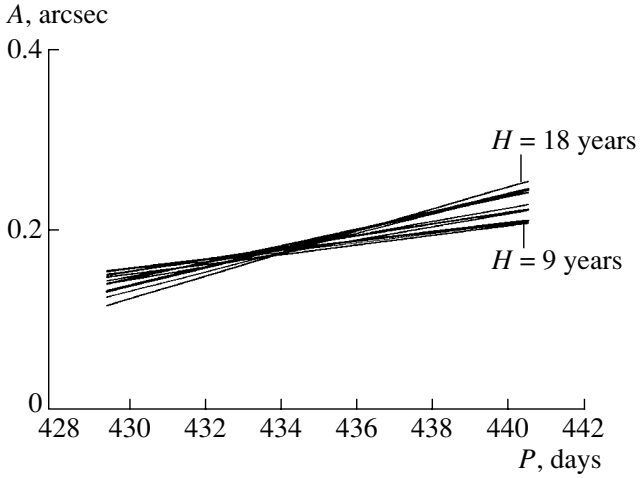

Fig. 3. Variations of the linear component of the mean amplitudes of the Chandler oscillations for various intervals H for the data.

Figure 3 shows the linear components of the amplitude variations as functions of the Chandler period for various values of H. The slope increases somewhat as H increases.

The correlation coefficient for the linear relation between A and P is 0.92 for periods from 429 to 442 days.

4. CONCLUSIONS

(1) The variations in the amplitude and period of the Chandler oscillation determined by a parametric action with a given modulation depth e and $\gamma < 0$ are in full agreement with the first and second empirical laws of Melchior, and also with the results of numerical modeling using experimental data obtained over the last century.

(2) The boundaries for the amplitude and period of the Chandler wobble are determined by the nonlinear character of the variations in the energy-consuming parameter ρ and by changes in the physical conditions of the Earth–Moon system associated with the motion of the barycenter.

5. ACKNOWLEDGMENTS

This work was supported by the Russian Foundation for Basic Research (project no. 01-02-16231).

REFERENCES

1. G. S. Kurbasova and L. V. Rykhlova, Astron. Zh. **72**, 945 (1995) [Astron. Rep. **39**, 845 (1995)].
2. G. Kurbasova and L. Rykhlova, *IAU Coll. 178: Polar Motion: Historical and Scientific Problems*, ASP Conf. Ser. **208**, Ed. by S. Dick, D. McCarthy, and B. Luzum (Astronomical Society of the Pacific, San Francisco, 2000), p. 493.
3. G. S. Kurbasova and L. V. Rykhlova, Astron. Zh. **78**, 1049 (2001) [Astron. Rep. **45**, 922 (2001)].
4. P. Melchior, *On the Motions of the Instantaneous Axis of Rotation Relative to the Earth* (Obs. Roy. Belgique, 1954), Monogr. No. 3.
5. W. Munk and G. Macdonald, *The Rotation of the Earth* (Cambrige, USA, 1960; Mir, Moscow, 1964).
6. G. S. Kurbasova, L. V. Rykhlova, and M. N. Rybalova, Astron. Zh. **79**, 579 (2002) [Astron. Rep. **46**, 515 (2002)].
7. G. S. Kurbasova, L. V. Rykhlova, and G. N. Shlikar', Astron. Zh. **71** (5), 811 (1994) [Astron. Rep. **38**, 724 (1994)].

Translated by V. Badin